Morphological quantification of the human cerebral cortex from MRI using deformable surfaces

Eskildsen, Simon Fristed

Publication date:
2008

Document Version
Publisher's PDF, also known as Version of record

Medical Informatics Group

The medical Informatics Group is part of the department of Health Science and Technology at Aalborg University.
Its main research area, initiated at Aalborg University in 1978, is information systems used for recording, analyzing, representing and interpreting clinical information. The aim of the Medical Informatics Group is to further develop methodologies and systems within three main areas:

- Metabolic Modeling
- Image Analysis
- Information Systems
- Telehealth

with a clear emphasis on clinical applicability for the benefit of patients in the health care system.

MI
Medical Informatics Group
Department of Health Science and Technology
Aalborg University
Fredrik Bajers Vej 7D
DK-9220 Aalborg
Denmark

Telephone: +45 9940 8080
Telefax: +45 9815 4008

URL: www.mi.hst.aau.dk
e-mail: contact@hst.aau.dk

ISBN: 978-87-7094-010-8

Morphological Quantification of the Human Cerebral Cortex from MRI using Deformable Surfaces

Simon Fristed Eskildsen

Medical Informatics Group

Morphological Quantification of the Human Cerebral Cortex from MRI using Deformable Surfaces

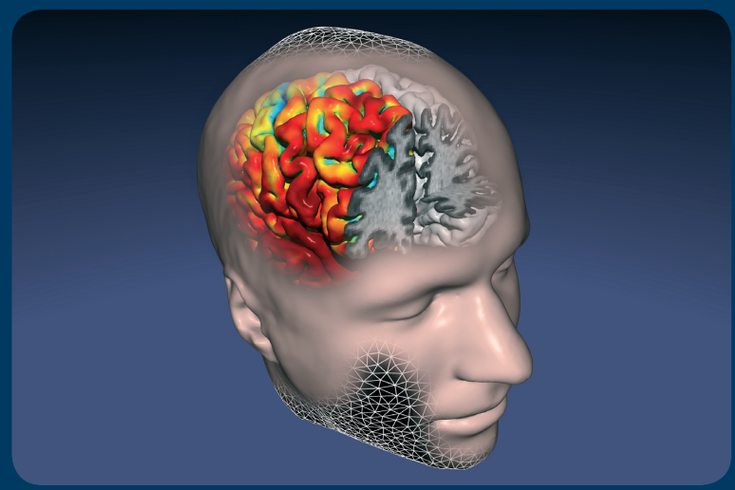

Simon Fristed Eskildsen

Medical Informatics Group
Department of Health Science and Technology
Aalborg University

2008

Author

Simon Fristed Eskildsen was born in Århus, Denmark. He received his M.Sc. in Electrical Engineering with specialization in Medical Informatics from Aalborg University in the summer of 2003. From 2003 to 2005 he was employed as a research assistant at the Department of Health Science and Technology. In 2005 he started his Ph.D. study which was defended in November 2008 at Aalborg University. Since 2008 he has been employed as an Assistant Professor at the Department of Health Science and Technology.

ISBN: 978-87-7094-010-8

Morphological Quantification of the Human Cerebral Cortex from MRI using Deformable Surfaces

PhD thesis by

Simon Fristed Eskildsen

Medical Informatics Group
Department of Health Science and Technology
Aalborg University

· 2008 ·

This thesis was finished July 2008 and was successfully defended November 26th 2008 at Aalborg University. The evaluation committee consisted of the following members:

Professor, MD, DMSc, Elna-Marie Larsson
Department of Radiology, Aalborg Sygehus
Århus University, Denmark

Associate Professor, PhD, Louis Collins
Montreal Neurological Institute
McGill University, Canada

Associate Professor, PhD, Stig Kjær Andersen (Chairman)
Department of Health Science and Technology
Aalborg University, Denmark

The cover image is a rendering of surfaces extracted from a T1 weighted magnetic resonance scan using the methods disclosed in the thesis.

ISBN: 978-87-7094-011-5

Abstract

This Ph.D. thesis investigates morphological quantification of the human cerebral cortex from magnetic resonance images (MRI). Morphological quantification of the cerebral cortex is important for understanding the manifestation and progression of neurodegenerative diseases such as Alzheimer's disease and such quantification are considered important disease markers and may aid in early diagnosis. The first part of the thesis deals with reconstruction of the cortex from T1 weighted MRI. The second part is concerned with using the cortical morphological measurements from the reconstructions to compare different cortices, and applying the quantification methods in a study of a neurodegenerative disease. The thesis is based on five papers; three papers covering the first part and two papers on the second part.

In paper I, the method for reconstructing the cortical boundaries as parametric surfaces is presented. The entire process from scanner images to cortical thickness results is described and test of the method on simulated MRI data, several young healthy individuals and a single Alzheimer's patient scanned with an interval of six months is presented. The paper presents a novel combination of a pressure force with a gradient vector flow in a deformable surface model for modeling the outer cortical boundary.

In paper II, an improved surface deformation process is presented. The energy functional described in the first paper is altered to express vector forces, and a local weighting of forces is introduced to better adapt to the highly folded cortical sheet. Test of the method on simulated MRI is reported and it is shown to be more accurate than approaches without the local weighting strategy. The main contribution of the paper is a deformation approach free of search spaces and a novel curvature influenced weighting of the terms in the energy functional.

Paper III describes the comparison of the developed method with the cortex extraction method used the most in the literature. The comparison is based on phantom MRI images constructed from cortical surfaces extracted from real MRI images. In this way, ground truth cortical boundaries are created and the geometrical error of the cortex reconstructions can be quantified. The paper reports that the developed method is reconstructing the cortical surfaces with a subvoxel accuracy and that it performs better than the competing method in most of the tests while being much faster.

In paper IV, the problem of comparing different cortices is addressed. A proposed feature driven cortical mapping algorithm is presented together with tests of it and four other mapping algorithms: a feature driven approach, two spherical mapping approaches, and a basic iterative closest point algorithm. The algorithms are evaluated with constructed criteria for a good mapping, a landmark test using manually placed landmarks and an analysis of statistical maps generated by the results of the algorithms. It is demonstrated that each method has its strengths and weaknesses and no single method performs better on all criteria and for all purposes. However, it is indicated that a combination of some of the evaluated algorithms could be a promising approach.

Paper V reports the results of applying the developed methods to identify cortical structural changes in individuals with a familial variant of frontotemporal dementia. Nine presymptomatic individuals carrying the disease mutation are compared to seven individuals from the same family without the mutation. The study is based on two serial MRI

scans of each individual and annualized atrophy rates are calculated. Both volumetric and thickness measurements show that the presymptomatic mutation carriers degenerate faster than the healthy controls. The thickness measurements have a higher sensitivity than the volumetric measurements and they are able to detect the focal differences between the two groups. Furthermore, the involved cortical areas are linked to symptoms observed in clinical frontotemporal dementia patients and support the pathogenicity of the mutation.

The work presented in the thesis demonstrate that it is possible to detect subtle morphological changes in the human cerebral cortex with MRI, and suggest that the goal of using morphological disease markers in improving diagnosis of neurodegenerative diseases is attainable.

Dansk Resumé (Danish Abstract)

Denne Ph.D. afhandling omhandler morfologisk kvantificering af den menneskelige hjernebark fra magnetisk resonans skanning (MRS). Morfologisk kvantificering af hjernebarken er vigtig for forståelsen af hvordan neurodegenerative sygdomme som Alzheimers sygdom manifesterer sig og udbredes i hjernen. Det vurderes at sådan kvantificering kan identificere sygdomsmarkører og kan bidrage til tidligere diagnose af neurodegenerative sygdomme. Første del af afhandlingen omhandler rekonstruktion af hjernebarken fra T1 vægtet MRS. Anden del fokuserer på at anvende rekonstruktionerne af hjernebarken til at kvantificere morfologien og sammenligne forskellige hjernebarker, og kvantificeringsmetoderne anvendes i et studie af en neurodegenerativ sygdom. Afhandlingen er baseret på fem artikler; tre artikler dækker første del og to omhandler anden del.

I artikel I præsenteres metoden til rekonstruktion af hjernebarkens vævsgrænser som parametriske overflader. Hele processen fra skannerbilleder til måling af hjernebarkens tykkelse er beskrevet og metoden testes på simuleret MRS data, unge raske individer og en enkelt Alzheimers patient skannet med seks måneders mellemrum. Artiklen præsenterer en tryk kraft kombineret med en gradient vektor kraft i en deformérbar overflademodel til modellering af hjernebarkens ydre vævsgrænse.

I artikel II præsenteres en forbedret deformeringsproces. Energifunktionen beskrevet i artikel I er forandret så der udtrykkes vektorkræfter, og en lokal vægtning af kræfterne introduceres for bedre tilpasning til hjernebarkens meget foldede struktur. Metoden testes på simulerede MRS og det vises at den er mere nøjagtig end metoder uden lokal vægtning af kræfterne. Hoved-bidraget i artiklen er en deformeringsmetode uden søgerum og en unik vægtning af termerne i energifunktionen baseret på overfladens krumning.

I artikel III sammenlignes den udviklede metode med den i litteraturen mest benyttede rekonstruktionsmetode. Sammenligningen er baseret på fantom MRS billeder konstrueret fra overflader af hjernebarken udtrukket fra rigtige skanninger. På denne måde genereres der data hvor den sande hjernebark er kendt og geometriske fejl i rekonstruktionerne kan måles. Artiklen viser at den udviklede metode har en nøjagtighed bedre end opløsningen af billederne, og at metoden er mere nøjagtig og hurtigere end den konkurrerende metode.

Artikel IV tager sig af problemet med at sammenligne forskellige hjernebarker. En metode til at referere mellem hjernebarker, som er baseret på sammenligning af geometriske features, præsenteres og testes sammen med fire andre referencemetoder; en anden feature baseret algoritme, to algoritmer der refererer til en kugle, og en simple iterativ nærmeste punkt algoritme. Algoritmerne evalueres med opstillede kriterier for en god reference, en test med manuelt placerede fikspunkter, samt en analyse af statistiske overfladekort genereret på baggrund af algoritmernes resultater. Det demonstreres at hver metode har sine styrker og svagheder, og at en enkelt metode ikke kan foretrækkes frem for en anden til alle formål på baggrund af de opstillede kriterier. Det antydes at en kombination af nogle af metoderne synes at være en lovende løsning på problemet.

Artikel V rapporterer resultaterne af at anvende de udviklede kvantificeringsmetoder til at identificere strukturelle forandringer i hjernebarken i individer fra en familie med en nedarvet variant af frontotemporal demens. Ni præsymptomatiske bærere af sygdomsgenet er sammenlignet med syv individer uden sygdommen fra samme familie. Studiet er baseret på to serielle skanninger af hvert individ, og atrofirater kan dermed beregnes. Både

volumetriske målinger og målinger af hjernebarkens tykkelse viser at de præsymptomatiske sygdomsbærere degenererer hurtigere end de raske kontrolpersoner. Tykkelsesmålingerne har en højere sensitivitet end de volumetriske målinger, og disse muliggør detektering af fokale forskelle de to grupper imellem. De involverede områder i hjernebarken kan henføres til symptomer observeret i kliniske patienter med frontotemporal demens og understøtter dermed patogeniciteten af sygdomsmutationen.

Forskningen præsenteret i denne afhandling demonstrerer at det er muligt at detektere små morfologiske forandringer i den menneskelige hjernebark fra strukturel MRS, og sandsynliggør at morfologiske sygdomsmarkører kan benyttes til at forbedre diagnosen af neurodegenerative sygdomme.

Acknowledgments

I wish to express my gratitude to the following institutions and foundations which have financially supported the Ph.D. study:

- Novi Innovation A/S
- Center for Functional and Integrative Neuroscience, Aarhus University
- HEALTHnTECH Research Center
- Virtual Centre for Health Informatics
- Spar Nord Fonden
- Det Obelske Familiefond
- Otto Mønsteds Fond
- The International Doctoral School of Technology and Science, Aalborg University

During my study I had the pleasure of visiting The McConnell Brain Imaging Centre (BIC), Montréal Neurological Institute, McGill University. I am grateful to Professor Alan C. Evans for the invitation, and to the inspiring and helpful people at the BIC. Also, I am grateful to the BIC for putting data from the International Consortium of Brain Mapping at my disposal during the Ph.D. study.

I wish to thank Dr. Peter Johannsen for collaboration and involving me in the FTD-3 study. Also thanks to Anders B. Rodell and Center for Functional and Integrative Neuroscience, Aarhus University for collaboration and good constructive discussions and advice. Thanks to Andrew Janke and Centre for Magnetic Resonance, The University of Queensland, Australia for providing challenging MRI data. Also thanks to the people at the radiological department at Aalborg Hospital for collaboration and co-supervision of students.

Special thanks to Mark Uldahl and Anders Prisak who co-founded the cortical reconstruction project during our master's thesis.

Finally, I wish to thank Camilla S. Grünberger and Mette Dencker for proof reading, all the nice people at the Medical Informatics group, and my supervisors Prof. Ole K. Hejlesen and Lasse R. Østergaard for their patience and support.

Preface

The content of this Ph.D. thesis is based on five papers written during the period of January 2005 to June 2008. Four papers were accepted for presentation at the following conferences:

- SPIE Medical Imaging 2005 - International Society for Optical Engineering, Medical Imaging conference in San Diego, USA, February 2005. Full papers (12 pages) were accepted on the basis of peer reviewed extended abstracts (4 pages).
- MICCAI 2006 - Medical Image Computing and Computer-Assisted Intervention conference in Copenhagen, Denmark, October 2006. 232 full papers (8 pages) were selected from 578 submissions based on peer reviews, acceptance rate: 40.1%. Proceedings are published in Lecture Notes on Computer Science.
- MICCAI 2007 - Medical Image Computing and Computer-Assisted Intervention conference in Brisbane, Australia, October-November 2007. 237 full papers (8 pages) were selected from 637 submissions based on peer reviews, acceptance rate: 37.2%. Proceedings are published in Lecture Notes on Computer Science.
- SIBGRAPI 2008 - The XXI Brazilian Symposium on Computer Graphics and Image Processing in Campo Grande, Mato Grosso do Sul, Brazil, October 2008. 38 full papers (8 pages) were selected from 107 submissions based on peer reviews, acceptance rate: 35.5%. Proceedings are published by IEEE CS Press.

The last paper has been accepted by the journal NeuroImage and is currently in press. NeuroImage communicates "important advances, using imaging and modelling techniques to study structure-function relationships in the brain." NeuroImage has an impact factor of 5.5 (2007).

Each paper is inserted into the thesis as a chapter only changing the layout and removing the abstract compared to the publication/submission. In addition to the five papers, the thesis contains a general introduction and discussion of the subject going into details not covered by the papers. Reference listings are contained within each chapter.

The algorithms developed and presented during the thesis have been implemented using the freely available software and programmer's interface MINC, which is available from http://www.bic.mni.mcgill.ca/software/

Simon Fristed Eskildsen
Aalborg, July 2008

Contents

List of Figures xiv

List of Tables xv

1 Introduction 1
1.1 Background . . . 1
1.2 Quantification of Cortical Structures . . . 3
1.2.1 Region Based Approaches . . . 3
1.2.2 Morphometry Based Approaches . . . 5
1.2.3 Surface Based Approaches . . . 7
1.3 Aim of the Ph.D. Study . . . 12
1.4 Outline and Contents of Thesis . . . 12
References . . . 14

2 Extraction of the Cerebral Cortical Boundaries from MRI for Measurement of Cortical Thickness 23
2.1 Introduction . . . 23
2.2 Methods . . . 24
2.2.1 Initial Inner Surface Generation . . . 24
2.2.2 Inner Surface Deformation . . . 25
2.2.3 Outer Surface Deformation . . . 26
2.2.4 Measurements . . . 28
2.3 Results . . . 28
2.4 Conclusion . . . 32
References . . . 33

3 Active Surface Approach for Extraction of the Human Cerebral Cortex from MRI 35
3.1 Introduction . . . 35
3.2 Methods . . . 36
3.2.1 Deformation Process . . . 36
3.2.2 Internal Forces . . . 36
3.2.3 External Forces . . . 37
3.3 Results . . . 39
3.4 Summary and Conclusion . . . 39
References . . . 41

4 Quantitative Comparison of Two Cortical Surface Extraction Methods Using MRI Phantoms 43
4.1 Introduction . . . 43
4.2 Methods . . . 43
4.2.1 FreeSurfer Method . . . 44
4.2.2 Fast Accurate Cortex Extraction Method . . . 44

4.2.3 Phantom Generation . . . 45
4.2.4 Accuracy Assessment . . . 45
4.3 Results . . . 46
4.4 Discussion . . . 47
References . . . 48

5 Evaluation of Five Algorithms for Mapping Brain Cortical Surfaces 51
5.1 Introduction . . . 51
5.2 Background . . . 51
5.3 Proposed Mapping Algorithm . . . 52
5.4 Algorithms Selected for Comparison . . . 53
5.5 Mapping Evaluation . . . 54
5.6 Results . . . 56
5.7 Discussion . . . 57
5.8 Conclusion . . . 60
References . . . 60

6 Cortical Volumes and Atrophy Rates in FTD-3 *CHMP2B* Mutation Carriers and Related Non-carriers 63
6.1 Introduction . . . 63
6.2 Materials and Methods . . . 64
6.2.1 Subjects . . . 65
6.2.2 Image Acquisition . . . 65
6.2.3 Image Processing . . . 65
6.2.4 Cortical Boundary Extraction . . . 66
6.2.5 Cortical Measurements . . . 67
6.2.6 Surface Mapping . . . 67
6.2.7 Statistical Analysis . . . 67
6.3 Results . . . 68
6.3.1 Cortical Boundary Extraction and Compartment Segmentations . . . 68
6.3.2 Cross-sectional Differences . . . 69
6.3.3 Longitudinal Effects . . . 69
6.3.4 Atrophy Rates . . . 69
6.3.5 Volume Measurements . . . 72
6.3.6 Asymmetry . . . 75
6.4 Discussion . . . 75
6.4.1 Cortical Thickness . . . 75
6.4.2 Cerebral Volumes . . . 76
6.4.3 Limitations of the Study . . . 77
6.4.4 Conclusion . . . 77
References . . . 78

7 Discussion and Conclusion 83
7.1 Cortical Reconstruction . . . 83
7.1.1 Deformable Surface Algorithm . . . 83
7.1.2 Automation and Robustness . . . 85
7.1.3 Computational Expense . . . 86
7.2 Cortical Surface Mapping . . . 87
7.3 Application on Neurodegenerative Diseases . . . 87
7.4 Future Directions . . . 89
7.5 Conclusion . . . 90
References . . . 90

List of Figures

2.1 Pipeline of the method. Rounded boxes indicate processing steps. Gray boxes indicate data. . . . 24
2.2 Process of generating the initial surface. Rounded boxes indicate processing steps. Gray boxes indicate data. . . . 25
2.3 Example of how the inflation force enables modeling of narrow sulci with no CSF evident. The gray solid line indicates the deformable surface, which approaches the GM/CSF boundary from the WM/GM boundary. As the deformable surface is pushed in the direction of the local surface normals, it will eventually meet itself inside deep narrow sulci. . . . 27
2.4 Example of a GGVF field based on an edge map calculated from the sum of the WM and GM memberships using the first order derivative. . . . 28
2.5 Visualization of the extracted inner and outer cortical surfaces of an ICBM subject. . . . 29
2.6 Intersections of inner and outer surfaces with MRI data of an ICBM subject. Top row: Inner surface. Bottom row: Outer surface. A few errors are visible in the images of second column, where the surfaces are penetrating both ventricles. These errors originate from the topology correction algorithm, that enforces a closed genus zero surface. . . . 30
2.7 Cortical thickness mapped onto the outer cortical surface as gray levels. Dark regions are thin, while bright regions are thick, ranging from 0 mm to 6 mm. . . . 30
2.8 The thickness pattern of 16 ICBM subjects seen from the top. . . . 31
2.9 Cortical thickness at two time points (The color scale ranges from 0 mm (black) to 6 mm (white)). . . . 32

3.1 Illustration of how the pressure force enables modelling of narrow sulci with no CSF evident. As the deformable surface (grey line) is pushed away from the WM/GM boundary in the direction of the local surface normals, it will eventually meet itself inside narrow sulci. . . . 38
3.2 Outer surface deformation process using different external forces at different stages in the process. Left to right: Deformation process at iterations 0,5,15 and 30. Top: Only pressure force is enabled. Middle: Only GGVF force is enabled. Bottom: Combination of both forces balanced by the curvature weighting function. . . . 40
3.3 Example of a generated cortex from ICBM data. Left: Rendering of outer surface. Right: Inner (black) and outer (white) surfaces superimposed onto MRI. . . . 40

4.1 Flow chart illustration of the comparison method. . . . 44
4.2 Fuzzy membership volumes generated from the extracted surfaces. Left to right: WM, GM, and CSF. . . . 45
4.3 Phantom produced by the MRI simulator (left), and final phantom after normalisation and added original tissue (right). . . . 46

4.4 Left: Surface extracted from original scan by FACE. Middle: Reconstruction from phantom by FreeSurfer. Right: Reconstruction from phantom by FACE. 47

5.1 From cortex surface to sphere. Left: Original cortical surface. Middle: Inflated surface with curvature values superimposed. Right: Surface mapped to a sphere with curvature values superimposed. 54
5.2 Average errors of mapping with the five tested algorithms between permutations of the 10 cortical surfaces (n=90). 56
5.3 Average distances in mm from mapped landmark to manually labeled landmark of 90 mappings. Landmarks are temporal pole (TP), supramarginal gyrus (SG), cuneus (Cun), gyrus rectus (GR), post central gyrus (PCG), and anterior cingulate gyrus (CG). 57
5.4 ICF compared vertex by vertex to the other four mapping algorithms visualized on an inflated reference surface. White areas indicate significant difference ($p<0.05$) in the cortical thicknesses mapped to a vertex. 57

6.1 Extraction of the cortical boundaries. a) Spatially aligned MRI data with initial (red contour) and final (yellow contour) brain extraction contour superimposed. b) Brain tissue classified as WM, GM, and CSF. c) Ventricles and subcortical regions labelled as WM, and WM separated into hemispheres by a sagittal cut through corpus callosum. d) Edge map calculated from the fuzzy classifications. e) WM surface superimposed on the MRI data. f) GM surface superimposed on the MRI data. 66
6.2 Statistical parametric map of differences in cortical thickness showing areas with $p < 0.01$ for one-sided t-test testing significant thinner cortex in mutation carriers compared to non-carriers. Map generated from pooled (baseline and follow-up) measurements and blurred with a diffusion smoothing approximating a Gaussian kernel smoothing with 10 mm FWHM. 69
6.3 Statistical parametric map of longitudinal differences in cortical thickness in mutation carriers showing areas with $p < 0.05$ for paired t-test testing significant thinner cortex. Map blurred with a diffusion smoothing approximating a Gaussian kernel smoothing with 10 mm FWHM. 71
6.4 Statistical parametric map of significantly ($p<0.01$) higher atrophy ratios in mutation carriers. Map blurred with a diffusion smoothing approximating a Gaussian kernel smoothing with 10 mm FWHM. Surface parts have been removed for better visualization of regions buried by the lateral fissures. Labels correspond to the clusters listed in table 6.5. Cluster sizes may appear smaller than they are due to visualization on a partially flattened surface. 72

List of Tables

2.1 Mean distance to nearest vertex on reference surface and standard deviations. 29

4.1 Errors measured by the four metrics on both WM and GM surfaces. Errors are deviation from the reference surfaces. For each metric the performance on both FreeSurfer and FACE phantoms is compared for the two methods (two-tailed paired t-test). Significant smaller errors are marked by bold font. 47

5.1 Average difference in mean cortical thickness after mapping. 56
5.2 Percent vertices of reference surface where the MWW test rejects the hypothesis that the cortical thicknesses come from the same population ($\alpha = 0.05$) for the different mapping algorithms, which means that the mappings influence the conclusion. 58

6.1 Subject demographic information. 65
6.2 Cortical thickness measurements (mm) averaged within main lobes at baseline and follow-up for mutation carriers (MC) and non-carriers (NC). Longitudinal differences evaluated by two-tailed paired t-test. Group differences evaluated by one-sided t-test with assumption of unequal variance on pooled measurements. 70
6.3 Anatomical regions with significantly ($p < 0.01$) thinner cortex in mutation carriers compared to non-carriers after smoothing. Only regions with an involved area of more than 1 cm^2 of either the left (LH) or right (RH) hemisphere are reported. The significant areas are visualized in figure 6.2. . 71
6.4 Annualized atrophy rates as percent decline of baseline thickness for mutation carriers (MC) and non-carriers (NC). Difference between groups evaluated as one-sided t-test with assumption of unequal variance. 73
6.5 Clusters of statistically significant higher atrophy ratios in mutation carriers compared with non-carriers. Clusters with significant contiguous areas >20 mm^2 are reported. Clusters are visualized in figure 6.4. 74
6.6 Compartment volumes (ml) corrected by eTIV for mutation carriers (MC) and non-carriers (NC) at baseline and follow-up. Longitudinal differences were adjusted for inter-scan interval and evaluated by two-tailed paired t-test. Group differences were evaluated by two-tailed t-test with assumption of unequal variance on pooled group measurements. 74

Chapter 1

Introduction

1.1 Background

Magnetic resonance imaging (MRI) emerged in the seventies [68, 80] and in the eighties the technology was introduced for clinical purposes [33]. Today, MRI is widely used for structural and functional imaging as well as for spectroscopy. Unlike other technologies based on x-rays or ultra-sound, MRI has the ability to distinguish soft tissues based on magnetic properties of atomic nuclei and this has revolutionized the field of structural medical imaging of the inner organs. Continuing improvement of MRI regarding image resolution and contrast has pushed the level of detail for visualization of the anatomy and images with sub-millimeter resolution are now common. Especially within the field of neurology, MRI has brought important new perspectives into understanding and diagnosing various diseases and disorders of the central nervous system as detailed visualization of the brain tissues is possible. Many neurological diseases and disorders are manifested in MRI visible pathologies of the cerebral anatomy.

Since the introduction of structural MRI in the field of neurology, increasing effort has been put into quantification of the imaged anatomical structures. In addition to physicians' qualitative and subjective assessments in clinical practice, research has pushed the need for standardized quantitative data to compare brain images across patients and imaging equipment, understand disease effects and progression and formalize diagnostic criteria based on the imaging data. One way to quantify an anatomical structure is by delineation of its boundaries. Protocols for manual delineations of anatomical structure boundaries are widely used [101, 116] and since the early nineties specific attention has been given to computerization and automation of structural quantification for consistency and precision improvement and human workload minimization.

Pathological conditions of both the cerebral gray matter (GM) and the cerebral white matter (WM) have been intensively investigated. The GM is primarily composed of neurons and holds functional areas contrary to the cerebral WM which is composed of signal transmitting myelinated axons. Many neurological disorders are linked to degeneration of the neurons, while others are due to chronic damage to the brain tissues. Important chronic neurological disorders affecting the cerebral tissues include epilepsy and mental disorders such as schizophrenia. Some neurodegenerative diseases such as multiple sclerosis primarily affect the WM while most neurodegenerative diseases primarily affect the GM. An important class of neurodegenerative diseases affecting the GM is dementias such as Alzheimer's disease (AD) which is recognized as one of the major health challenges of this century because of the growing elderly population [11]. Pathological GM regions are mainly found in the cerebral cortex, the largest part of the human brain. Regions of extensive research are the hippocampal formation and neocortical regions.

Hippocampus is part of the limbic system and primarily involves memory formations. It is affected in diseases such as schizophrenia, temporal lobe epilepsy (TLE) and various

neurodegenerative diseases. In TLE, the hippocampal size and shape play critical roles in the diagnosis and assessment of need for surgical intervention and for these reasons measurement of the hippocampus is used in clinical practice. Because of the structural compactness and limited size of the hippocampus, it is possible to quantify the structure by manual delineation of the boundaries directly on the images. Various neurodegenerative diseases such as AD, vascular dementia, and Parkinson's disease cause hippocampal atrophy [12, 65, 67]. However, hippocampal volume estimates are not used in the clinical diagnosis of these patients despite existing evidence that hippocampal volume is an important clinical marker in these diseases and may aid in earlier diagnosis compared to diagnostic criteria only based on neuropsychological tests [18]. A reason for this is that, contrary to TLE, changes in the hippocampal structure are not specific for these neurodegenerative diseases as more information is needed to differentiate between the diagnoses. Studies indicate that a combination of changes found in the hippocampus and the neocortex may provide better differentiation [18]. Despite the small and confined size of the hippocampus, no globally accepted consensus on the manual delineation yet exists [78]. Even if operators follow the same segmentation protocol, significant inter- and intra-operator variability in the resulting hippocampal volume is observed [55]. This makes hippocampal measurements difficult to compare across studies and complicates statistics based on such measurements.

The neocortex is a tightly folded sheet of tissue covering the cerebral hemispheres. Neocortex is relatively thin (2-3 mm) compared to its area (2000-2500 cm^2) and holds the majority of the brain's functional areas such as visual, sensory and auditory processing and interpretation, motor control and cognition [44]. In some diseases, e.g. frontotemporal dementia, the primary structural changes are found in the neocortex, thus rendering this anatomical structure an important clinical marker [96]. The association neocortex is also involved in early AD and this involvement of neocortex differentiates AD from normal aging according to histopathological studies [18]. However, as with the hippocampus, neocortical structural changes are rarely used in the diagnosis of neurodegenerative diseases and MRI scans are usually only acquired to rule out differential diagnoses such as tumors or other brain damage when diagnosing a suspected dementia [100].

Many of the neurodegenerative diseases affecting the cerebral cortex are difficult to diagnose because of their overlapping symptoms and insidious onset. This is the case especially for dementias and as only symptomatic and disease stalling treatment can be offered, early and correct diagnosis is critical [45]. Cortical atrophy is seen as one possible marker in early dementia [93]. Widespread cortical atrophy can be observed from MRI images, often manifested in enlarged ventricles, but it is not clearly present in the early stages of neurodegenerative diseases. The subtle focal changes related to the early stages of neurodegenerative diseases, as revealed by detailed structural MRI, have been extensively researched for the purpose of early detection, thus aiding in early diagnosis [3, 7, 12, 15, 16, 18, 37, 46, 56–58, 65, 67, 92, 96, 100, 117]. Detection of such focal cortical changes occurring in larger cortical areas seems highly impractical in the clinic using conventional manual delineations when considering the limited clinical use of hippocampal quantification. Therefore, robust, automatic delineations or segmentations of the cerebral cortex may be the only way to integrate knowledge of subtle structural changes in the early diagnosis of neurodegenerative diseases.

In addition to aiding in patient diagnosis, automatic methods for quantifying cerebral structures bring the possibility of performing large scale cohort studies when investigating the structural manifestations of various brain diseases. Furthermore, standardized quantifications may aid in validating pharmaceuticals targeted to stop or reduce cerebral atrophy and may even speed up the process of clinical trials. In recognition of these important perspectives, numerous automatic or semi-automatic methods have been developed for quantifying the structures of the human cerebral cortex.

1.2 Quantification of Cortical Structures

Traditionally, structural brain imaging has been applied to detect pathologies readily visible in the images. Pathological conditions such as tumors, hemorrhages and ischaemia are usually discovered by a single MR scan while tissue in the process of neurodegeneration may not be detectable from a single scan. Because of the large variability of the normal brain, the subtle changes occurring in the early stages of neurodegenerative diseases require serial scans to follow the progression and detect the pathological tissue. However, with the increasing knowledge of the alterations to the brain tissues caused by various neurodegenerative diseases, disease specific atrophy patterns or signatures may be revealed in the future which enables detection of early atrophy from a single scan [118]. Therefore, researchers are working toward a goal of differentiating between different neurodegenerative diseases by cortical atrophy patterns and identifying clinical markers to aid in early diagnosis. Reaching this goal involves accurately measuring subtle morphological changes, identifying similar patterns of atrophy in population groups, and finally applying the quantification methods in clinical studies.

To effectively measure subtle morphological changes and differences in the cerebral cortex, 3D T1 weighted high resolution images are needed [4] and are usually acquired by gradient echo sequences. Voxel sizes around one cubic millimeter are common and images with high tissue contrast are generated with at least 1.5 Tesla scanners. 3 Tesla scanners are increasingly becoming available in hospitals [90].

Even though MRI can capture the cerebral anatomy in high detail and with excellent contrast, the morphological quantification is complicated by factors related to noise, distortion and other artifacts found in MRI [119]. Cortical morphological quantification is further complicated by the complex structure and proximate objects with overlapping image intensities such as the dura mater and larger veins.

A proliferation of methods to quantify differences and changes in the cerebral cortex has been seen during the last twenty years. The methods apply a variety of techniques and a taxonomy of the methods can be constructed based on these techniques [107]. Here the focus is on three main categories in which most work on cortical quantification fall: 1) methods that perform segmentation of the cortex by labeling the image voxels (region based), 2) methods that quantify changes in intensity between scans (morphometry based) and 3) methods that integrate knowledge of the underlying anatomy to reconstruct the tissue boundaries (surface based).

1.2.1 Region Based Approaches

A classical way of quantifying structures in images is segmentation of the object of interest. Region based approaches operate in the image domain analyzing the intensity values and perform discrete morphological operations to identify structures. Segmentation is performed by labeling each pixel or voxel in the image as belonging to different classes (different objects of interest). Structural quantifications are usually based on voxel counts (volumetric measurements).

Conventional image segmentation techniques include thresholding, region growing and clustering algorithms. However, when analyzing biological images such simple approaches are rarely sufficient. Within the field of neuro imaging, more complex segmentation solutions have therefore been proposed. Here three categories of segmentation approaches are covered: region of interest segmentation, atlas based methods and segmentation approaches based on tissue classification.

Region of Interest

Region of interest (ROI) methods compute an overall size for each brain structure based on segmentations. Conventional segmentations involve manual delineations of tissue boundaries in consecutive slices of an MRI scan [56–58]. Such delineations of tissue

boundaries are laborious and subject to inter-operator variability [30]. However, semi-automated [92,125] and fully automated [51–53,89] methods have been proposed, but these are not widely used [3]. Other ROI methods use stereology to quantify the structure [26]. Volume estimates from ROI analysis can provide valuable insight into neurodegenerative diseases, but in the early stages of neurodegenerative diseases, changes in overall volume are minimal [4] and the subtle changes in subregions of the ROI may be overlooked. ROI analysis is mainly applied in quantification of relatively small confined structures such as the hippocampus, the caudate nucleus and the entorhinal cortex as these are of a manageable size but still recognized as important surrogate markers for several neurodegenerative diseases [92].

Apart from human interaction related problems of manual or semi-automated methods, the focus on a single structure ignores changes in other structures and may forestall new insight into the pathology of neurodegenerative diseases [3].

Atlas Based

Atlas based approaches co-register the subject image with a template containing predefined target regions of interest (atlas) so that segmentation of the target regions can be obtained by mapping atlas regions to the subject image. Such an approach is dependent on the registration technique used, the template selected and the atlas applied for the segmentation. Numerous registration methods exist [77, 128], as image registration is intensively researched and driven by a wide range of application areas.

Usually a brain template is the average of a large sample of spatially aligned images. Such an average has well-defined image edges of morphologically invariant structures while structures with greater variation, such as the cortical regions, are usually blurred in the template image. Morphological variations can be reduced by generating templates based on high dimensional non-linear registrations, thus resulting in averages with more well-defined image edges. However, removing morphological variations may lead to alignments where the images no longer are anatomically consistent. Several groups have developed and refined MRI brain templates and atlases [32, 34, 39].

Choice of template is important for the subsequent segmentation [95]. If the subjects under study are homogeneous with respect to factors such as age and disease stage, it may be preferred to use an image from the target population as template instead of an average template from a broader population [16]. In such cases, manual intervention is needed to define the regions of interest in the template. Problems with artifacts and poor signal-to-noise of a single image can be solved by repeated imaging and averaging of the same subject [54].

Atlas based approaches are well-suited for quantification of regions with little morphological variation. However, in the case of the cerebral cortex it is difficult, if not inconceivable, to create a template representative of the great variation in cortical folding patterns.

Tissue Classification

Tissue classification of the cortical GM provides means for measuring the cortical volume. Usually, a classification into WM, GM, and cerebrospinal fluid (CSF) is performed. In order to accomplish such classification, non-cerebral tissues are usually removed prior to classification. A variety of classification methods have been proposed based on Bayesian analysis [81], clustering [86], fuzzy classification [112], neural networks [114], deterministic annealing [40], Markov Random Fields [98] and combinations [8].

Other methods for cortical GM classification have been proposed. Bazin and Pham proposed a method that enforces a given topology on the target structure which prevents holes and handles from occurring in the segmentation [10]. Such topological inconsistencies are often seen in conventional classification methods due to image noise. Angelini et al. used a deformable model to segment the brain into WM, GM and CSF [2]. As described

later on, deformable models are often used to reconstruct the cortical surface; however, this approach uses a level set frame work solely for voxel classification.

Tissue classification of voxels in the image is limited by the image resolution so partial volume effects influence the segmentation. Furthermore, classification of the cortical GM only provides global measures of differences in the cortical volume. For measuring focal effects regional subdivisions are needed. This involves manual delineations or combination with an atlas technique.

Discussion of Region Based Approaches

Region based approaches for quantification of the cerebral cortex all have problems attached: ROI analysis requires human interaction which is laborious and prone to errors and variability. Model and atlas based approaches have difficulties capturing the wide morphological variety of the human cortex. Tissue classification only provides global measures of cortical volume differences.

Generally, methods resulting in voxel based segmentation suffer a number of problems regarding morphological quantification. Firstly, the segmentations are limited by the image resolution so only structural changes of voxel size proportions can be detected. Secondly, morphological characteristics such as curvature and thickness are difficult to capture from simple connected segmentations. This is even more complicated for the cortical structure because of its tightly folded appearance. Cortical thickness estimates have been proposed using a segmentation method propagating out distance values from the WM component until the GM/CSF interface is reached [73]. However, partial volume effects complicate the detection of GM/CSF image edges and often subvoxel accuracy is needed to identify subtle tissue differences.

1.2.2 Morphometry Based Approaches

Morphometry based approaches analyze the intensity difference between serial images or between an image and a template. Such approaches rely on registration techniques to spatially align images. Three types of intensity difference based methods have been developed for quantification of cerebral structures. Two approaches directly measure differences in intensity while one analyzes the deformation field involved in the spatial alignment of images.

Intensity Shift Approaches

Intensity shift approaches compute brain volume change by quantifying the difference in image intensity between spatially aligned serial MRI scans in longitudinal studies. Usually only whole brain volume change is measured automatically; regional atrophy is determined by manually defined regions. Two intensity shift methods are popular, namely the boundary shift integral (BSI) [38] and structural image evaluation using normalization of atrophy (SIENA) [103].

BSI uses a rigid transformation in the alignment and intensities are normalized to compare follow-up scans with the baseline scan. The method quantifies the shift in tissue boundaries by integrating over the difference in image intensities.

SIENA corrects for skull size in the registration procedure which results in a full affine transformation and resamples both baseline and follow-up scans to obtain images with similar interpolation-related blurring. SIENA identifies edge points in both images and estimates the motion of each point perpendicularly to the local edge. This reduces the sensitivity to intensity normalization.

Both BSI and SIENA have been shown to provide reasonably accurate measures of brain atrophy [14] and to be capable of separating AD patients from healthy controls [46]. However, whole brain measures are insufficient for determining subtle changes in the early stages of neurodegenerative diseases and regional measures using these methods are

dependent on manual intervention. Furthermore, these methods are dependent on serial scans which induce diagnosis delay [4].

Intensity shift approaches are highly dependent on the registration and normalization of intensities which is complicated by common intensity non-uniformities caused by inhomogeneities in the radio frequency field coil [127] and other artifacts [119].

Voxel Based Morphometry

Voxel based morphometry (VBM) performs voxel-wise comparisons between spatially aligned MRI scans of subject groups enabling identification of increased or decreased GM density throughout the entire brain [5, 120]. The spatial alignment involves classification of GM, WM and CSF. The GM map is non-linearly registered to a template and group averages are calculated and spatially smoothed with a filter. Group differences and correlations with clinical parameters are estimated by fitting a statistical model at each voxel [3].

The accuracy of VBM depends on the registration technique used and anatomical differences may be inferred by systematic registration errors or by systematic shifts in unaffected regions caused by changes in affected regions [13, 110]. To address these issues, information of the deformations (expansions or contractions) involved in the registration is encoded in the aligned GM map [43]. This approach is called optimized VBM.

A similar approach, called regional analysis of volumes examined in normalized space (RAVENS), has been proposed [29, 30, 42]. RAVENS use a high-dimensional elastic transformation driven by point correspondences in the spatial normalization process while optimized VBM relies on relatively smoother parametric transformations [4, 30]. The information of the deformation field is encoded in the aligned map thus preserving tissue volumes of the original image similar to optimized VBM [30].

VBM analysis has been applied in numerous studies of cerebral disorders [62, 117], normal brain development and aging [104] and other non-pathological investigations [25, 82, 88].

VBM techniques are criticized for being too reliant on a perfect registration and doubtful assumptions in the statistical model [110]. Another issue is that VBM does not account for the cortical folds which means that small effects of opposing sulcal walls may give rise to an accumulated significant effect when averaging the GM maps [3, 36].

Tensor Based Morphometry

Tensor based morphometry (TBM) analyzes the deformation field involved in high-dimensional non-linear mapping of serial intra-subject images [6, 19]. Using the determinant of the Jacobian matrix associated with the deformation field, local tissue expansion and shrinkage can be identified and the Jacobian maps can be used to quantify intra-subject longitudinal effects and differences between subject groups. Expressing the tissue expansion and shrinkage by the Jacobian maps removes directional information of atrophy which may be non-isotropic. New methods use the full dimensionality of the deformation tensors and can better detect and visualize focal areas of atrophy [3].

TBM has been used in different areas such as studying the developing human brain [21], visualizing the atrophy pattern in patients with AIDS [19] and measuring degeneration in Alzheimer's disease [37] and fronto-temporal lobar degeneration [7, 15, 105].

The accuracy of TBM depends on the applied registration method and cortical folding patterns are not accounted for.

Discussion of Morphometry Based Approaches

Morphometry based approaches address the problem of the limited resolution as sub-voxel changes of the structures can be seen as changes in voxel intensity. However, such

approaches have other problems attached regarding the morphological quantification. Intensity shift analysis measures whole brain changes which is insensitive to subtle cortical changes found in the early stages of many neurodegenerative diseases. Furthermore, these methods are very reliant on intensity normalization and registration performance which may introduce uncertainties in the measurements. Also VBM and TBM are relying on the quality of image registration and they further lack the ability to distinguish effects from opposing walls of tight sulci.

1.2.3 Surface Based Approaches

Surface based approaches model the cortical sheet with 2D manifold surfaces embedded in 3D, thus aiming at modeling the underlying anatomy. This relaxes the restrictions imposed by the limited image resolution and enables incorporation of anatomical knowledge. Furthermore, surface based approaches are potentially independent of image registration and intensity normalization. Finally, such approaches allow for distinguishing opposing walls of sulci due to the explicit reconstruction of the cortical sheet.

Apart from morphological quantification purposes, surface based reconstruction of the cerebral cortex has application within functional brain imaging for mapping activity onto the cortical surface [109] and within neuro-surgery for preoperative planning, postoperative evaluation and surgery simulation. Also, visualizations of the buried cortical regions are possible by cortical unfolding [36], as well as assignment of anatomical labels to the cortical GM [99]. In addition to visualization purposes, surface reconstructions provide the means for creating surface based atlases where anatomical and functional regions can be defined in a canonical space, thus complementing the widely accepted volumetric coordinate spaces and atlases [36].

As the human cerebral cortex is a complex, highly convolved sheet-like structure, the modeling of the structure using surfaces is challenging. In MRI, the cortical boundaries are often obscured or partly missing because of noise, inhomogeneity artifacts and partial volume effects originating from the acquisition [119]. Opposite banks of tight sulci on the outer boundary may meet inside the sulcal folds and appear as connected in MRI. Surface modeling can compensate for obscured and incomplete image edges. However, in MRI, information on the outer cortical boundary may be completely missing in several tight sulci and at the top of gyri the boundary may be obscured by meninges and dura mater close to the cortex. Furthermore, issues concerning the topology of the cortical sheet are unavoidable because of the inherent noise in MR images.

The ideal surface modeling of the cerebral cortex must align with the true underlying anatomical boundaries of the cortex and respect the true cortical topology which is spherical if closed at the brain stem [48]. To achieve these properties, a proliferation of methods for modeling the cerebral cortex with surfaces has been proposed during the last decade. One way of reconstructing the cortex is using deformable models where a contour or surface is manipulated to fit target image boundaries. Usually, approaches based on deformable models implement either a variant of the classical active contours [23, 61]; parametric deformable models or a variant based on geometric deformable models [87, 97]. Other approaches for cortical reconstruction by surfaces usually apply voxel based techniques in combination with iso-surface algorithms such as Marching Cubes [74].

A common trait of deformable models is that an initial contour or surface is evolved toward target boundaries. In parametric deformable models, the initial contour or surface keeps the same topology during deformation. This is especially useful when the target structure has a known topology. Geometric deformable models have the ability to change topology and adapt to the topology of the target structure. This is advantageous in many segmentation problems, however, when the target structure has a known topology it is a distinct disadvantage not having a fixed topology during surface evolution. This drawback is especially pronounced when geometric deformable models are applied to noisy images as found in MRI.

Usually the contour or surface is initialized completely inside or completely outside the target boundary and uses inflation or contraction to approach the target boundary in an iterative manner. The main difficulty in cortical reconstruction lies in correctly modeling the tightly folded sulci. Methods initializing a surface outside the cortex have problems penetrating the sulci and reaching their fundi. The GM/WM boundary is easier to discern in MRI because these image edges, contrary to the GM/CSF boundary, are unaffected by the tight folds and proximate dura mater. Therefore, several methods utilize information of the GM/WM boundary to detect the GM/CSF boundary as the cortex can be considered as a continuous laminar structure with smoothly varying thickness.

Methods for surface reconstruction of the cerebral cortex have been developed since the early nineties and many research groups have contributed to the field. The following describe a selection of these contributions using parametric and geometric deformable models as well as other surface based approaches for reconstructing or quantifying the cerebral cortex.

Parametric Deformable Models

Parametric deformable models are originating from the so-called snake formulation by Kass et al. [61]. The basic method describes a parametric 2D contour influenced by internal spline forces and external image and constraint forces. A functional expressing the energy of the snake was iteratively minimized to obtain the location of the contour with the lowest energy, thus resulting in a segmentation of the image. Cohen and Cohen introduced an inflation force to the active contour [22] and extended it to 3D and so named it a balloon model [23].

Davatzikos and Prince proposed to model the cortical sheet by a ribbon model where a 2D contour was fitted to the center of the cortical sheet using the homogeneity of intensity levels within the GM [31]. Davatzikos and Bryan extended the ribbon model to 3D with initialization outside the brain [28]. Vaillant and Davatzikos further refined the method and obtained parametrizations of the sulcal folds using separate active contours for each fold [113]. This approach relies on close initialization of the contour and manual interaction in order to model the sulcal folds. Furthermore, the use of separate active contours to model the sulci alters the topology of the reconstruction.

McInerney and Terzopoulos added a reparametrization step to the active contour by defining a grid of nodes as either inside or outside the contour [83, 85]. This way, the contour can dynamically change the topology and easily grow from a small initialization contour. These so-called T-snakes were extended to 3D (T-surfaces), and it was demonstrated that a T-surface can be fitted to the GM/CSF boundary by initializing it outside the cortex [84]. This strategy, however, fails to grow into the sulci.

MacDonald et al. used a sphere as the initial surface and deformed it to the GM/WM boundary in a multiscale fashion. Subsequently, a coupled surface approach was applied. In this approach, two surfaces simultaneously are deformed under proximity constraints maintaining a predefined minimum and maximum distance between the GM/WM and GM/CSF boundary [75]. This way the GM/CSF surface is dragged towards the fundi of sulci and spherical topology is enforced due to the spherical initial surface. The proximity constraints prevent the coupled surfaces model from accurately delineating cortical areas with a thickness outside the predefined distance interval. Furthermore, such an approach is more computational expensive as the model becomes more complex by the surface coupling.

An approach by Dale et al. identifies the GM/WM boundary using voxel classifications, iso-surface extraction and a deformable model. This surface is subsequently expanded towards the GM/CSF boundary [27]. This has the advantage that all sulci are present in the initial state and enables the preservation of the sulci during deformation even though evidence of the GM/CSF boundary may be missing in the MRI data. The tight sulcal folds are modeled by preventing self-intersections in the deforming surface, thus the delineation of the folds are placed equidistantly from the sulcal walls of the GM/WM boundary.

Clearly, the direction of inflation is important to the resulting outer surface. Dale et al. used the directions of the surface normals. This single surface approach is faster than the coupled surface approach by MacDonald et al. and it captures all the tight sulci. However, the expansion of the surface towards the outer boundary is sensitive to small errors or irregularities in the initial surface which may lead to modeling of non-existent folds.

Xu et al. also used a GM/WM surface as the initialization of a deformable model [121]. They used a gradient vector flow (GVF) to define directions toward the central layer of the cortex. This solution provides a fast and consistent convergence of the surface, but tight sulci with no evidence of the outer boundary are not captured by this method. Their approach does not impose self-intersection constraints which is necessary when segmenting the outer boundary and the approach requires manual interaction.

Another approach using a WM/GM boundary representation for subsequent GM/CSF delineation was proposed by Kriegeskorte and Goebel [66]. They extract the WM voxels in each hemisphere of the cerebrum using a combination of atlas masking, intensity inhomogeneity correction, anisotropic filtering and region growing. The hemispheric WM components are modified to obtain spherical topology and are tessellated to polygon meshes. Vertices of the polygon meshes are shifted along surface normals to delineate the GM/WM boundary and the GM/CSF boundary. Unfortunately, it is not clear from the documentation how the boundaries are detected during the deformation process.

Kim et al. [64] proposed a method where the WM surface is obtained by deforming a spherical polygon model to the GM/WM boundary as done by MacDonald et al. [75]. The GM/CSF boundary is found by expanding the WM surface along a Laplacian field generated between the WM surface and a skeletonized CSF image while preventing self-intersections. While achieving relatively robust and consistent convergence, this method is highly dependent on classification of CSF and the assumption that CSF is at least partly visible between all sulcal folds.

Xu et al. initialized an ellipsoidal mesh outside the cortex and used a GVF field combined with an inward pressure force to deform the mesh to the cortical boundaries [122]. They used a reproducing kernel particle method as the deformation model which provides efficient reparametrization procedures and self-intersections are avoided by using fast marching methods. Though this approach is novel in the way the deformations are implemented, the shrink-wrapping strategy still suffers from inability to reach deep into tight sulcal folds.

Geometric Deformable Models

Geometric deformable models are variants of the propagating fronts methods [17,20,87,97], where the surface is implicitly represented as the zero isovalue of a level set function. Because of the implicit representation, no self-intersections can occur in geometric deformable models. After propagation of the level set function, a parametric surface can be obtained by computing an iso-surface at the zero isovalue of the level set function. Level set methods are numerically stable and faster than algorithms deforming parametric models [50].

Zeng et al. used a coupled surfaces approach in a level set framework [126]. Goldenberg et al. adopted the coupled surfaces approach and formulated the segmentation as a minimization problem [41]. Coupled surfaces approaches enable modeling of tight sulcal folds because of an inter-surface distance constraint. However, these methods suffer the same problems as the approach by MacDonald et al. [75]. Furthermore, in both approaches the resulting surfaces have arbitrary topologies due to the level set evolution technique.

Han et al. proposed a topology preserving geometric deformable model (TGDM) where the evolving surface is kept homeomorphic to the boundary of a digital object delineated by the level set function on an underlying grid [47, 50]. The surface is only allowed to change sign at simple points of the underlying grid, thus preserving the topology of the digital object and the surface. A GM/WM surface is obtained by WM classification followed by a TGDM with a regularizing force and a signed pressure force based on fuzzy

tissue classifications. The central cortical layer are delineated by evolving the GM/WM surface using a TGDM with a GVF force similar to the parametric approach by Xu et al. [121]. Finally, the GM/CSF boundary is obtained by propagating the central cortical surface using a TGDM with combined pressure and GVF forces. This approach overcomes a number of the problems related to cortical surface reconstruction by enforcing correct topology while maintaining fast and consistent convergence. However, manual interaction is required in the preprocessing steps of the method.

Xue et al. used the framework of Han et al. [47] to reconstruct the cortical surfaces of neonates [124]. Cortical reconstruction of neonate brains is particularly difficult because of inverted GM/WM contrast in MRI images compared to adults, lower contrast-to-noise ratio, the maturation process which continuously changes the GM/WM contrast and the different folding patterns at different stages of the developing brain. Therefore, the main differences between the methods by Xue et al. and Han et al. are the tissue classification process and a relaxation of the spherical topology constraint as the topology of neonate cortices are not well-established. In contrast to the method by Han et al., the reconstruction of neonatal cortices is fully automatic, suggesting that reconstructions of adult cortices also could be done fully automatic.

Li et al. proposed a very fast method based on dual front active contours [71]. Dual front active contours iteratively find the global minimum within an active region based on minimal path techniques [24] where the active region is defined on both sides of the contour, typically by simple dilations with a structuring element. For the purpose of cortex segmentation, Li et al. used histogram analysis to define the active region instead of simple dilations. The approach requires manual adjustment of histogram parameters. Furthermore, in pathological brains tissue intensities may not have distinct peaks in the histogram which complicates the estimation of a proper threshold. Finally, the topology problem was not addressed in the proposed method.

Other Surface Reconstructions

Though most approaches to cortical reconstruction are variants of parametric or geometric deformable models, other techniques have also been suggested. In addition to low level methods such as edge detection [63] and region growing [123], a variety of algorithms have been proposed. For example Mangin et al. used a 3D skeletonization of the GM/CSF interface to generate a surface and extract sulcal patterns [79]. Van Essen et al. used a combination of Gaussian intensity transformations, gradient information and manual guidance with subsequent iso-surface extraction and topology correction to obtain a surface representation of the center of the cortex [115]. Shattuck and Leahy segmented the WM of each hemisphere, modified the WM component to obtain spherical topology, and extracted the GM/WM boundary using an iso-surface algorithm [102]. A similar approach with a Bayesian segmentation was used by Joshi et al. on digitized cryosections of macaque monkey brains [60]. However, such methods are not well suited for generating accurate and topologically correct representations of the outer cortical boundary which is why deformable models have gained popularity within the field over the recent years.

Some methods quantify the cortical morphology by combining a surface representation with analysis of the image intensity. Barta et al. used a stochastic model of the intensity distance histogram relative to the GM/WM surface to measure the cortical thickness [9]. Others calculate the cortical thickness using voxel segmentation and only use the cortical surface for projection of the thickness, thus enabling visualization and mapping of the cortical thickness [111]. It is argued that voxel based cortical thickness estimations, though less accurate, are more robust than approaches explicitly modeling the outer cortical boundary [9, 111]. Such hybrid methods may be useful. However, to quantify the morphology of the cortical sheet to its full extent, complete surface reconstructions still seem to be the best solution.

Discussion of Surface Based Approaches

Surface based approaches applying deformable models have problems attached to surface initialization, topology of target structure and robust detection of image boundaries during surface evolution. As described above several solutions to overcome these problems have been proposed.

Several researchers suggest the use of coupled surfaces [41, 75, 126]. Coupled surfaces approaches have the advantage of explicitly using information of both cortical boundaries to detect the outer boundary. This enables the GM/CSF surface to model the deep, narrow sulci. The coupling is achieved by specifying a minimum and a maximum distance between the surfaces. Such constraints, however, preclude the modeling of anatomy deviating from the norm as defined by the distance limits. When modeling abnormal anatomy found in neurodegenerative diseases and other neurological disorders or normal neonatal anatomy, restrictions on the cortical thickness render such approaches inapt to accurately quantify the true morphology [124]. Furthermore, even in normal adult cortices, a bias between the chosen predefined distance and a measured cortical thickness may be inferred by the restrictions [75].

Recent methods seem to develop in similar directions. The most promising methods, whether based on parametric or geometric deformable models, for reconstructing the GM/CSF boundary use a GM/WM boundary representation to fit the surface to the outer cortical boundary. These methods follow roughly the steps of 1) cerebrum WM classification, 2) topology correction, 3) WM tessellation and 4) expansion of WM surface towards the GM/CSF boundary [27, 47, 64, 66], where step 2 and 3 may be omitted if a spherical surface is deformed to the WM/GM boundary [64]. The methods proposed by Dale et al. [27], Xu et al. [121], Han et al. [47], and Kim et al. [64] all use similar strategies for expanding the WM surface towards the central/GM surface; all four methods use a vector field for guiding the surface towards the target boundary. Dale et al. use surface normals, Xu et al. and Han et al. use a GVF field, and Kim et al. use a Laplacian field. Such vector fields provide better and more consistent convergence than using variants of the basic image gradient.

Developers expanding the WM surface to the central cortical layer instead of the outer cortical boundary argue that this representation of the cortex provides better geometric information than both the inner and outer boundaries [72, 121]. However, explicit representations of the tissue boundaries better support measurements of cortical thickness. Furthermore, altered morphology caused by pathologies may be easier detectable at the tissue boundaries than at the center-line of the structure.

The different image forces proposed for evolving the deformable models towards the cortical boundaries can all be applied in both parametric and geometric frameworks. Choice of framework seems to be dependent on what property the individual developer finds most important. One property that is emphasized repeatedly is the ability to constrain topology of the final contour. With the classical deformable models this could only be achieved by parametric models. However, with the development of topology preserving level sets [49], the use of geometric models for cortical reconstruction have become more popular. Recently, Ségonne developed a level set method where the topology can be controlled without loosing the ability of contours to merge, split and vanish during evolution which usually advocates a strong advantage over parametric deformable models [108]. Others are also working on variants of topology preserving level sets [1, 69, 94, 106].

Hybrid methods combining surface reconstruction with voxel based analysis are potentially very robust. However, full cortical surface reconstructions provide information of the morphology which cannot be quantified by hybrid methods. So far, the most promising methods to obtain complete cortical reconstructions rely on deformable models. Even though problems related to deformable models, such as robustness, are evident in today's surface solutions, the goal is still accurate reconstructions of the cerebral cortex for the detection of subtle, focal morphological changes as found in neurodegenerative diseases.

1.3 Aim of the Ph.D. Study

A main goal within the field of structural brain imaging and brain morphometry is to differentiate between different neurodegenerative diseases by cortical atrophy patterns. This thesis addresses the initial steps toward this goal. The aim is to develop methods for quantifying structural changes in the human cerebral cortex from MRI images. To accomplish this, a method based on deformable models is developed to automatically delineate the cortical boundaries. Specifically, parametric deformable surfaces are used to delineate the GM/WM and GM/CSF boundaries of the cortex. From surfaces representing the cortical boundaries several measures describing the cortical structure can be obtained. The cortical thickness is an important measure, but quantities such as the cortical area and curvature may also be involved in describing the changing cortex as well as cortical volume for comparison purposes with volumetric methods.

Measuring the cortical thickness from surfaces of the cortical boundaries is not a simple matter due to the complex morphology. Several methods for measuring the thickness from cortical reconstructions have been proposed [35,59,70,76]. Also morphological quantification by other measures exists [91], but it is outside the scope of this Ph.D. study to develop new methods for such quantification.

The ability to quantify the cortical structure from MRI provides a mean for quantifying changes over time or differences between subjects for the entire cortical structure. However, such global quantities are not sensitive to small cortical changes and this raises a need for quantifying focal changes and differences. This can be accomplished by subdividing the cortical sheet by means of an atlas which may be based on anatomical, functional or other types of regions. However, applying fixed cortical regions wherein the measurements are averaged, also limits the sensitivity of the quantification as focal changes may be present across regions. Therefore, a point correspondence between cortical surfaces is needed to fully benefit from the measurements cortical surfaces provide and part of the study is concerned with the search for a suitable method for obtaining such a cortical mapping.

Finally, the Ph.D. study investigates the application of the methods developed during the study within the field of neurodegenerative diseases. This is done by applying the methods to quantify cortical structural changes in individuals from a large Danish family with an inherited variant of frontotemporal dementia.

1.4 Outline and Contents of Thesis

The thesis is based on five papers. Two papers describe the fundamental method for extracting the cortical boundaries from MRI using deformable surfaces. The third paper compares the developed method with a well-known and widely used method. The fourth paper deals with the mapping between different cortical surfaces to compare similar anatomical regions over groups of subjects. Finally, in the last paper, the methods developed during the Ph.D. study are applied in a study of preclinical individuals with a familial neurodegenerative disease.

Paper I: Extraction of the Cerebral Cortical Boundaries from MRI for Measurement of Cortical Thickness (Chapter 2)

In this paper the fundamental idea of extracting the cortical boundaries is presented. The entire process from scanner images to cortical thickness results is described and test of the method on simulated MRI data, several young healthy individuals and a single AD patient scanned with an interval of six months is presented. The surface deformation process described in the paper is based on a parametric deformable model and uses a discrete search space to minimize an energy functional. The method is related to the approach by McInerney and Terzopoulos [84] in the sense that reparametrizations are performed during

surface evolution. The main contribution of the paper is the combination of a pressure force with a gradient vector flow in the deformation of the outer cortical boundary.

Paper II: Active Surface Approach for Extraction of the Human Cerebral Cortex from MRI (Chapter 3)

In this paper an improved surface deformation process is presented. Instead of minimizing an energy functional in a discrete search space, the optimal deformation directions are expressed as vectors leading to a force balancing scheme. The energy functional described in the first paper is altered to express vector forces and a local weighting of forces is introduced to better adapt to the highly folded cortical sheet. Test of the method on simulated MRI is reported and the resulting cortical surfaces are shown to better model the folded structure than surfaces obtained by a pressure force or a gradient vector flow force alone. The main contribution of the paper is a deformation approach free of search spaces and a novel weighting of the terms in the energy functional influenced by surface curvature.

Paper III: Quantitative Comparison of Two Cortical Surface Extraction Methods Using MRI Phantoms (Chapter 4)

This paper describes the comparison of the developed method with the cortex extraction method used the most in the literature, namely FreeSurfer, which is developed at Harvard and based on the method by Dale et al. [27]. The comparison is based on phantom MRI images constructed from cortical surfaces extracted from real MRI images. In this way, ground truth cortical boundaries are created and the geometrical error of the cortex reconstructions can be quantified. The paper's conclusion is that the developed method is reconstructing the cortical surfaces with a subvoxel accuracy and that it performs better than FreeSurfer in most of the tests as well as being much faster.

Paper IV: Evaluation of Five Algorithms for Mapping Brain Cortical Surfaces (Chapter 5)

In this paper five different algorithms for mapping between surfaces of the cerebral cortex are evaluated. The focus is on algorithms for mapping between vertices of discrete surfaces which is complicated by the possibly arbitrary vertex count of the cortical surfaces. A proposed feature driven mapping algorithm is presented together with tests of it and four other mapping algorithms consisting of a feature driven approach, two spherical mapping approaches and a basic iterative closest point algorithm. The algorithms are evaluated with constructed criteria for a good mapping, a landmark test using manually placed landmarks and an analysis of constructed statistical maps. The paper concludes that no algorithm can be singled out as the best choice of mapping between cortical surfaces; each method has its strengths and weaknesses. However, it is indicated that a combination of a spherical warp approach with an iterative feature based algorithm could be a promising choice.

Paper V: Cortical Volumes and Atrophy Rates in FTD-3 *CHMP2B* Mutation Carriers and Related Non-carriers (Chapter 6)

This paper reports the results of applying the developed methods to identify cortical structural changes in individuals with a familial variant of frontotemporal dementia. Nine presymptomatic individuals carrying the disease mutation are compared to seven individuals from the same family without the mutation. The study is based on two serial MRI scans of each individual and annualized atrophy rates are calculated. Both volumetric and thickness measurements show that the presymptomatic mutation carriers degenerate

faster than the healthy controls. The thickness measurements have a higher sensitivity than the volumetric measurements and are able to detect the focal cortical differences between the two groups. Furthermore, the involved cortical areas are linked to symptoms observed in clinical frontotemporal dementia patients and support the pathogenicity of the mutation.

Discussion and Conclusions (Chapter 7)

The final chapter provides a discussion of the methods developed and results obtained during the Ph.D. study and the thesis is concluded with summarizing the technological and scientific contributions of the study and provides directions for future research within the field.

References

[1] O. Alexandrov and F. Santosa. A topology-preserving level set method for shape optimization. *Journal of Computational Physics*, 204(1):121–130, 2005.

[2] E. D. Angelini, T. Song, B. D. Mensh, and A. F. Laine. Brain MRI segmentation with multiphase minimal partitioning: A comparative study. *International Journal of Biomedical Imaging*, 2007, 2007.

[3] L. G. Apostolova and P. M. Thompson. Brain mapping as a tool to study neurodegeneration. *Neurotherapeutics*, 4(3):387–400, 2007.

[4] J. Ashburner, J. G. Csernansky, C. Davatzikos, N. C. Fox, G. B. Frisoni, and P. M. Thompson. Computer-assisted imaging to assess brain structure in healthy and diseased brains. *Lancet Neurology*, 2(2):79–88, 2003.

[5] J. Ashburner and K. J. Friston. Voxel-based morphometry - the methods. *NeuroImage*, 11(6 I):805–821, 2000.

[6] J. Ashburner, C. Hutton, R. Frackowiak, I. Johnsrude, C. Price, and K. Friston. Identifying global anatomical differences: Deformation-based morphometry. *Human Brain Mapping*, 6(5-6):348–357, 1998.

[7] B. Avants, M. Grossman, and J. C. Gee. The correlation of cognitive decline with frontotemporal dementia induced annualized gray matter loss using diffeomorphic morphometry. *Alzheimer Disease and Associated Disorders*, 19(SUPPL. 1), 2005.

[8] V. Barra and J. Y. Boire. Tissue segmentation on MR images of the brain by possibilistic clustering on a 3D wavelet representation. *Journal of Magnetic Resonance Imaging*, 11(3):267–278, 2000.

[9] P. Barta, M. I. Miller, and A. Qiu. A stochastic model for studying the laminar structure of cortex from MRI. *IEEE Transactions on Medical Imaging*, 24(6):728–742, 2005.

[10] P.-L. Bazin and D. L. Pham. Topology-preserving tissue classification of magnetic resonance brain images. *IEEE Transactions on Medical Imaging*, 26(4):487–496, 2007.

[11] C. Berr, J. Wancata, and K. Ritchie. Prevalence of dementia in the elderly in europe. *European Neuropsychopharmacology*, 15(4):463–471, 2005.

[12] M. Bobinski, J. Wegiel, H. M. Wisniewski, M. Tarnawski, M. Bobinski, B. Reisberg, M. J. De Leon, and D. C. Miller. Neurofibrillary pathology - correlation with hippocampal formation atrophy in Alzheimer disease. *Neurobiology of Aging*, 17(6):909–919, 1996.

[13] F. L. Bookstein. "voxel-based morphometry" should not be used with imperfectly registered images. *NeuroImage*, 14(6):1454–1462, 2001.

[14] O. Camara, R. I. Scahill, J. A. Schnabel, W. R. Crum, G. R. Ridgway, D. L. G. Hill, and N. C. Fox. Accuracy assessment of global and local atrophy measurement techniques with realistic simulated longitudinal data. 4792 LNCS(PART 2):785–792, 2007.

[15] V. A. Cardenas, A. L. Boxer, L. L. Chao, M. L. Gorno-Tempini, B. L. Miller, M. W. Weiner, and C. Studholme. Deformation-based morphometry reveals brain atrophy in frontotemporal dementia. *Archives of Neurology*, 64(6):873–877, 2007.

[16] O. T. Carmichael, H. A. Aizenstein, S. W. Davis, J. T. Becker, P. M. Thompson, C. C. Meltzer, and Y. Liu. Atlas-based hippocampus segmentation in Alzheimer's disease and mild cognitive impairment. *NeuroImage*, 27(4):979–990, 2005.

[17] V. Caselles, F. Catté, T. Coll, and F. Dibos. A geometric model for active contours in image processing. *Numerische Mathematik*, 66(1):1–31, 1994.

[18] G. Chetelat and J.-C. Baron. Early diagnosis of Alzheimer's disease: Contribution of structural neuroimaging. *NeuroImage*, 18(2):525–541, 2003.

[19] M.-C. Chiang, R. A. Dutton, K. M. Hayashi, O. L. Lopez, H. J. Aizenstein, A. W. Toga, J. T. Becker, and P. M. Thompson. 3D pattern of brain atrophy in HIV/AIDS visualized using tensor-based morphometry. *NeuroImage*, 34(1):44–60, 2007.

[20] D. L. Chopp. Computing minimal surfaces via level set curvature flow. *Journal of Computational Physics*, 106(1):77–91, 1993.

[21] M. K. Chung, K. J. Worsley, T. Paus, C. Cherif, D. L. Collins, J. N. Giedd, J. L. Rapoport, and A. C. Evans. A unified statistical approach to deformation-based morphometry. *NeuroImage*, 14(3):595–606, 2001.

[22] L. D. Cohen. On active contour models and balloons. *CVGIP: Image Understanding*, 53(2):211–218, 1991.

[23] L. D. Cohen and I. Cohen. Finite-element methods for active contour models and balloons for 2-D and 3-D images. *IEEE Transactions on Pattern Analysis and Machine Intelligence*, 15(11):1131–1147, 1993.

[24] L. D. Cohen and R. Kimmel. Global minimum for active contour models: A minimal path approach. *International Journal of Computer Vision*, 24(1):57–78, 1997.

[25] K. P. Cosgrove, C. M. Mazure, and J. K. Staley. Evolving knowledge of sex differences in brain structure, function, and chemistry. *Biological Psychiatry*, 62(8):847–855, 2007.

[26] L. M. Cruz-Orive. Stereology of single objects. *Journal of Microscopy*, 186(2):93–107, 1997.

[27] A. M. Dale, B. Fischl, and M. I. Sereno. Cortical surface-based analysis: I. Segmentation and surface reconstruction. *NeuroImage*, 9(2):179–194, 1999.

[28] C. Davatzikos. Using a deformable surface model to obtain a shape representation of the cortex. *IEEE Transactions on Medical Imaging*, 15(6):785–795, 1996.

[29] C. Davatzikos. Mapping image data to stereotaxic spaces: Applications to brain mapping. *Human Brain Mapping*, 6(5-6):334–338, 1998.

[30] C. Davatzikos, A. Genc, D. Xu, and S. M. Resnick. Voxel-based morphometry using the RAVENS maps: Methods and validation using simulated longitudinal atrophy. *NeuroImage*, 14(6):1361–1369, 2001.

[31] C. A. Davatzikos and J. L. Prince. Active contour model for mapping the cortex. *IEEE Transactions on Medical Imaging*, 14(1):65–80, 1995.

[32] H. A. Drury and D. C. Van Essen. Functional specializations in human cerebral cortex analyzed using the visible man surface-based atlas. *Human Brain Mapping*, 5(4):233–237, 1997.

[33] W. A. Edelstein, J. M. S. Hutchison, G. Johnson, and T. Redpath. Spin warp NMR imaging and applications to human whole-body imaging. *Physics in Medicine and Biology*, 25(4):751–756, 1980.

[34] A. C. Evans, D. L. Collins, and B. Milner. An MRI-based stereotactic brain atlas from 300 young normal subjects. *Proceedings of the 22nd Symposium of the Society for Neuroscience*, page 408, 1992.

[35] B. Fischl and A. M. Dale. Measuring the thickness of the human cerebral cortex from magnetic resonance images. *Proceedings of the National Academy of Sciences of the United States of America*, 97(20):11050–11055, 2000.

[36] B. Fischl, M. I. Sereno, and A. M. Dale. Cortical surface-based analysis: II. Inflation, flattening, and a surface-based coordinate system. *NeuroImage*, 9(2):195–207, 1999.

[37] N. C. Fox, W. R. Crum, R. I. Scahill, J. M. Stevens, J. C. Janssen, and M. N. Rossor. Imaging of onset and progression of Alzheimer's disease with voxel-compression mapping of serial magnetic resonance images. *Lancet*, 358(9277):201–205, 2001.

[38] P. A. Freeborough and N. C. Fox. The boundary shift integral: An accurate and robust measure of cerebral volume changes from registered repeat MRI. *IEEE Transactions on Medical Imaging*, 16(5):623–629, 1997.

[39] K. J. Friston, A. P. Holmes, K. J. Worsley, J. . Poline, C. D. Frith, and R. S. J. Frackowiak. Statistical parametric maps in functional imaging: A general linear approach. *Human Brain Mapping*, 2(4):189–210, 1994.

[40] Z. Ge, V. Venkatesan, and S. Mitra. A statistical 3-D segmentation algorithm for classifying brain tissues in multiple sclerosis. *Proceedings of the IEEE Symposium on Computer-Based Medical Systems*, pages 455–460, 2001.

[41] R. Goldenberg, R. Kimmel, E. Rivlin, and M. Rudzky. Cortex segmentation: A fast variational geometric approach. *IEEE Transactions on Medical Imaging*, 21(12):1544–1551, 2002.

[42] A. F. Goldszal, C. Davatzikos, D. L. Pham, M. X. H. Yan, R. N. Bryan, and S. M. Resnick. An image-processing system for qualitative and quantitative volumetric analysis of brain images. *Journal of Computer Assisted Tomography*, 22(5):827–837, 1998.

[43] C. D. Good, J. Ashburner, and R. S. J. Frackowiak. Computational neuroanatomy: New perspectives for neuroradiology. *Revue Neurologique*, 157(8-9 I):797–805, 2001.

[44] L. D. Griffin. The intrinsic geometry of the cerebral cortex. *Journal of Theoretical Biology*, 166(3):261–273, 1994.

[45] H. Grossman, C. Bergmann, and S. Parker. Dementia: A brief review. *Mount Sinai Journal of Medicine*, 73(7):985–992, 2006.

[46] J. L. Gunter, M. M. Shiung, A. Manduca, and C. R. Jack Jr. Methodological considerations for measuring rates of brain atrophy. *Journal of Magnetic Resonance Imaging*, 18(1):16–24, 2003.

[47] X. Han, D. L. Pham, D. Tosun, M. E. Rettmann, C. Xu, and J. L. Prince. CRUISE: Cortical reconstruction using implicit surface evolution. *NeuroImage*, 23(3):997–1012, 2004.

[48] X. Han, C. Xu, U. Braga-Neto, and J. L. Prince. Topology correction in brain cortex segmentation using a multiscale, graph-based algorithm. *IEEE Transactions on Medical Imaging*, 21(2):109–121, 2002.

[49] X. Han, C. Xu, and J. L. Prince. A topology preserving level set method for geometric deformable models. *IEEE Transactions on Pattern Analysis and Machine Intelligence*, 25(6):755–768, 2003.

[50] X. Han, C. Xu, D. Tosun, and J. L. Prince. Cortical surface reconstruction using a topology preserving geometric deformable model. *Proceedings of the Workshop on Mathematical Methods in Biomedical Image Analysis*, pages 213–220, 2001.

[51] R. E. Hogan, R. D. Bucholz, and S. Joshi. Hippocampal deformation-based shape analysis in epilepsy and unilateral mesial temporal sclerosis. *Epilepsia*, 44(6):800–806, 2003.

[52] R. E. Hogan, K. E. Mark, L. Wang, S. Joshi, M. I. Miller, and R. D. Bucholz. Mesial temporal sclerosis and temporal lobe epilepsy: MR imaging deformation-based segmentation of the hippocampus in five patients. *Radiology*, 216(1):291–297, 2000.

[53] R. E. Hogan, L. Wang, M. E. Bertrand, L. J. Willmore, R. D. Bucholz, A. S. Nassif, and J. G. Csernansky. MRI-based high-dimensional hippocampal mapping in mesial temporal lobe epilepsy. *Brain*, 127(8):1731–1740, 2004.

[54] C. J. Holmes, R. Hoge, L. Collins, R. Woods, A. W. Toga, and A. C. Evans. Enhancement of MR images using registration for signal averaging. *Journal of Computer Assisted Tomography*, 22(2):324–333, 1998.

[55] C. R. Jack Jr., M. D. Bentley, C. K. Twomey, and A. R. Zinsmeister. MR imaging-based volume measurements of the hippocampal formation and anterior temporal lobe: Validation studies. *Radiology*, 176(1):205–209, 1990.

[56] C. R. Jack Jr., R. C. Petersen, Y. Xu, P. C. O'Brien, G. E. Smith, R. J. Ivnik, B. F. Boeve, E. G. Tangalos, and E. Kokmen. Rates of hippocampal atrophy correlate with change in clinical status in aging and AD. *Neurology*, 55(4):484–489, 2000.

[57] C. R. Jack Jr., R. C. Petersen, Y. Xu, P. C. O'Brien, G. E. Smith, R. J. Ivnik, E. G. Tangalos, and E. Kokmen. Rate of medial temporal lobe atrophy in typical aging and Alzheimer's disease. *Neurology*, 51(4):993–999, 1998.

[58] C. R. Jack Jr., M. M. Shiung, J. L. Gunter, P. C. O'Brien, S. D. Weigand, D. S. Knopman, B. F. Boeve, R. J. Ivnik, G. E. Smith, R. H. Cha, E. G. Tangalos, and R. C. Petersen. Comparison of different MRI brain athrophy rate measures with clinical disease progression in AD. *Neurology*, 62(4):591–600, 2004.

[59] S. E. Jones, B. R. Buchbinder, and I. Aharon. Three-dimensional mapping of cortical thickness using Laplace's equation. *Human Brain Mapping*, 11(1):12–32, 2000.

[60] M. Joshi, J. Cui, K. Doolittle, S. Joshi, D. Van Essen, L. Wang, and M. I. Miller. Brain segmentation and the generation of cortical surfaces. *NeuroImage*, 9(5):461–476, 1999.

[61] M. Kass, A. Witkin, and D. Terzopoulos. Snakes: Active contour models. *International Journal of Computer Vision*, 1(4):321–331, 1988.

[62] S. S. Keller and N. Roberts. Voxel-based morphometry of temporal lobe epilepsy: An introduction and review of the literature. *Epilepsia*, 49(5):741–757, 2008.

[63] D. N. Kennedy, P. A. Filipek, and V. S. Caviness Jr. Anatomic segmentation and volumetric calculations in nuclear magnetic resonance imaging. *IEEE Transactions on Medical Imaging*, 8(1):1–7, 1989.

[64] J. S. Kim, V. Singh, J. K. Lee, J. Lerch, Y. Ad-Dab'bagh, D. MacDonald, J. M. Lee, S. I. Kim, and A. C. Evans. Automated 3-D extraction and evaluation of the inner and outer cortical surfaces using a laplacian map and partial volume effect classification. *NeuroImage*, 27(1):210–221, 2005.

[65] J. H. Kordower, Y. Chu, G. T. Stebbins, S. T. Dekosky, E. J. Cochran, D. Bennett, and E. J. Mufson. Loss and atrophy of layer II entorhinal cortex neurons in elderly people with mild cognitive impairment. *Annals of Neurology*, 49(2):202–213, 2001.

[66] N. Kriegeskorte and R. Goebel. An efficient algorithm for topologically correct segmentation of the cortical sheet in anatomical MR volumes. *NeuroImage*, 14(2):329–346, 2001.

[67] M. P. Laakso, K. Partanen, P. Riekkinen Jr., M. Lehtovirta, E. . Helkala, M. Hallikainen, T. Hänninen, P. Vainio, and H. Soininen. Hippocampal volumes in Alzheimer's disease, parkinson's disease with and without dementia, and in vascular dementia: An MRI study. *Neurology*, 46(3):678–681, 1996.

[68] P. C. Lauterbur. Image formation by induced local interactions: Examples employing nuclear magnetic resonance. *Nature*, 242(5394):190–191, 1973.

[69] C. Le Guyader and L. A. Vese. Self-repelling snakes for topology-preserving segmentation models. *IEEE Transactions on Image Processing*, 17(5):767–779, 2008.

[70] J. P. Lerch and A. C. Evans. Cortical thickness analysis examined through power analysis and a population simulation. *NeuroImage*, 24(1):163–173, 2005.

[71] H. Li, A. Yezzi, and L. D. Cohen. 3D brain segmentation using dual-front active contours with optional user interaction. *International Journal of Biomedical Imaging*, 2006, 2006.

[72] T. Liu, J. Nie, A. Tarokh, L. Guo, and S. T. C. Wong. Reconstruction of central cortical surface from brain MRI images: Method and application. *NeuroImage*, 40(3):991–1002, 2008.

[73] G. Lohmann, C. Preul, and M. Hund-Georgiadis. Morphology-based cortical thickness estimation. *Information processing in medical imaging : proceedings of the conference*, 18:89–100, 2003.

[74] W. E. Lorensen and H. E. Cline. Marching cubes: A high resolution 3D surface construction algorithm. *Computer Graphics (ACM)*, 21(4):163–169, 1987.

[75] D. MacDonald, N. Kabani, D. Avis, and A. C. Evans. Automated 3-D extraction of inner and outer surfaces of cerebral cortex from MRI. *NeuroImage*, 12(3):340–356, 2000.

[76] D. MacDonald, N. Kabani, D. Avis, and A. C. Evans. Automated 3-D extraction of inner and outer surfaces of cerebral cortex from MRI. *NeuroImage*, 12(3):340–356, 2000.

[77] J. B. A. Maintz and M. A. Viergever. A survey of medical image registration. *Medical Image Analysis*, 2(1):1–36, 1998.

[78] N. V. Malykhin, T. P. Bouchard, C. J. Ogilvie, N. J. Coupland, P. Seres, and R. Camicioli. Three-dimensional volumetric analysis and reconstruction of amygdala and hippocampal head, body and tail. *Psychiatry Research - Neuroimaging*, 155(2):155–165, 2007.

[79] J. Mangin, V. Frouin, I. Bloch, J. Régis, and J. López-Krahe. From 3D magnetic resonance images to structural representations of the cortex topography using topology preserving deformations. *Journal of Mathematical Imaging and Vision*, 5(4):297–318, 1995.

[80] P. Mansfield. Multi-planar image formation using NMR spin echoes. *Journal of Physics C: Solid State Physics*, 10(3), 1977.

[81] J. L. Marroquin, B. C. Vemuri, S. Botello, F. Calderon, and A. Fernandez-Bouzas. An accurate and efficient Bayesian method for automatic segmentation of brain MRI. *IEEE Transactions on Medical Imaging*, 21(8):934–945, 2002.

[82] A. May and C. Gaser. Magnetic resonance-based morphometry: A window into structural plasticity of the brain. *Current Opinion in Neurology*, 19(4):407–411, 2006.

[83] T. McInerney and D. Terzopoulos. Topologically adaptable snakes. *Proc. Fifth International Conf. on Computer Vision*, pages 840–845, 1995.

[84] T. McInerney and D. Terzopoulos. Topology adaptive deformable surfaces for medical image volume segmentation. *IEEE Transactions on Medical Imaging*, 18(10):840–850, 1999.

[85] T. McInerney and D. Terzopoulos. T-snakes: Topology adaptive snakes. *Medical Image Analysis*, 4(2):73–91, 2000.

[86] A. Noe and J. C. Gee. Partial volume segmentation of cerebral MRI scans with mixture model clustering. *IPMI2001*, pages 423–430, 2001.

[87] S. Osher and J. A. Sethian. Fronts propagating with curvature-dependent speed: Algorithms based on Hamilton-Jacobi formulations. *J. Comput. Phys.*, 79(1):12–49, 1988.

[88] J. S. Peper, R. M. Brouwer, D. I. Boomsma, R. S. Kahn, and H. E. Hulshoff Pol. Genetic influences on human brain structure: A review of brain imaging studies in twins. *Human Brain Mapping*, 28(6):464–473, 2007.

[89] A. Pitiot, H. Delingette, P. M. Thompson, and N. Ayache. Expert knowledge-guided segmentation system for brain MRI. *NeuroImage*, 23(SUPPL. 1):S85–S96, 2004.

[90] J. A.-L. Prado. 3-Tesla MRI and temporal lobe epilepsy. *Seminars in Ultrasound, CT and MRI*, 28(6):451–461, 2007.

[91] M. E. Rettmann, X. Han, C. Xu, and J. L. Prince. Automated sulcal segmentation using watersheds on the cortical surface. *NeuroImage*, 15(2):329–344, 2002.

[92] B. H. Ridha, J. Barnes, J. W. Bartlett, A. Godbolt, T. Pepple, M. N. Rossor, and N. C. Fox. Tracking atrophy progression in familial Alzheimer's disease: a serial MRI study. *Lancet Neurology*, 5(10):828–834, 2006.

[93] K. Ritchie and S. Lovestone. The dementias. *Lancet*, 360(9347):1759–1766, 2002.

[94] M. Rochery, I. H. Jermyn, and J. Zerubia. Higher order active contours. *International Journal of Computer Vision*, 69(1):27–42, 2006.

[95] T. Rohlfing, R. Brandt, R. Menzel, and C. R. Maurer Jr. Evaluation of atlas selection strategies for atlas-based image segmentation with application to confocal microscopy images of bee brains. *NeuroImage*, 21(4):1428–1442, 2004.

[96] H. J. Rosen, M. L. Gorno-Tempini, W. P. Goldman, R. J. Perry, N. Schuff, M. Weiner, R. Feiwell, J. H. Kramer, and B. L. Miller. Patterns of brain atrophy in frontotemporal dementia and semantic dementia. *Neurology*, 58(2):198–208, 2002.

[97] E. Rouy and A. Tourin. Viscosity solutions approach to shape-from-shading. *SIAM Journal on Numerical Analysis*, 29(3):867–884, 1992.

[98] S. Ruan, C. Jaggi, J. Xue, J. Fadili, and D. Bloyet. Brain tissue classification of magnetic resonance images using partial volume modeling. *IEEE Transactions on Medical Imaging*, 19(12):1179–1187, 2000.

[99] S. Sandor and R. Leahy. Surface-based labeling of cortical anatomy using a deformable atlas. *IEEE Transactions on Medical Imaging*, 16(1):41–54, 1997.

[100] P. Scheltens. Early diagnosis of dementia: Neuroimaging. *Journal of Neurology*, 246(1):16–20, 1999.

[101] L. J. Seidman, S. V. Faraone, J. M. Goldstein, J. M. Goodman, W. S. Kremen, R. Toomey, J. Tourville, D. Kennedy, N. Makris, V. S. Caviness, and M. T. Tsuang. Thalamic and amygdala-hippocampal volume reductions in first-degree relatives of patients with schizophrenia: An MRI-based morphometric analysis. *Biological Psychiatry*, 46(7):941–954, 1999.

[102] D. W. Shattuck and R. M. Leahy. Brainsuite: An automated cortical surface identification tool. *Medical Image Analysis*, 6(2):129–142, 2002.

[103] S. M. Smith, N. De Stefano, M. Jenkinson, and P. M. Matthews. Normalized accurate measurement of longitudinal brain change. *Journal of Computer Assisted Tomography*, 25(3):466–475, 2001.

[104] E. R. Sowell, P. M. Thompson, and A. W. Toga. Mapping changes in the human cortex throughout the span of life. *Neuroscientist*, 10(4):372–392, 2004.

[105] C. Studholme, V. Cardenas, R. Blumenfeld, N. Schuff, H. J. Rosen, B. Miller, and M. Weiner. Deformation tensor morphometry of semantic dementia with quantitative validation. *NeuroImage*, 21(4):1387–1398, 2004.

[106] G. Sundaramoorthi and A. Yezzi. Global regularizing flows with topology preservation for active contours and polygons. *IEEE Transactions on Image Processing*, 16(3):803–812, 2007.

[107] J. S. Suri, S. Singh, and L. Reden. Computer vision and pattern recognition techniques for 2-d and 3-d mr cerebral cortical segmentation (part i): A state-of-the-art review. *Pattern Analysis and Applications*, 5(1):46–76, 2002.

[108] F. Ségonne. Active contours under topology control-genus preserving level sets. *International Journal of Computer Vision*, 79(2):107–117, 2008.

[109] P. C. Teo, G. Sapiro, and B. A. Wandell. Creating connected representations of cortical gray matter for functional MRI visualization. *IEEE Transactions on Medical Imaging*, 16(6):852–863, 1997.

[110] N. Thacker. Tutorial: A critical analysis of voxel based morphometry (VBM). Technical report, Division of Imaging Science and Biomedical Engineering, University of Manchester, 2005.

[111] P. M. Thompson, A. D. Lee, R. A. Dutton, J. A. Geaga, K. M. Hayashi, M. A. Eckert, U. Bellugi, A. M. Galaburda, J. R. Korenberg, D. L. Mills, A. W. Toga, and A. L. Reiss. Abnormal cortical complexity and thickness profiles mapped in williams syndrome. *Journal of Neuroscience*, 25(16):4146–4158, 2005.

[112] J. K. Udupa and S. Samarasekera. Fuzzy connectedness and object definition: Theory, algorithms and applications in image segmentation. *Graphical Models and Image Processing*, 16(3):246–261, 1995.

[113] M. Vaillant and C. Davatzikos. Finding parametric representations of the cortical sulci using an active contour model. *Medical Image Analysis*, 1(4):295–315, 1997.

[114] R. Valdés-Cristerna, V. Medina-Bañuelos, and O. Yáñez-Suárez. Coupling of radial-basis network and active contour model for multispectral brain MRI segmentation. *IEEE Transactions on Biomedical Engineering*, 51(3):459–470, 2004.

[115] D. C. Van Essen, H. A. Drury, J. Dickson, J. Harwell, D. Hanlon, and C. H. Anderson. An integrated software suite for surface-based analyses of cerebral cortex. *Journal of the American Medical Informatics Association*, 8(5):443–459, 2001.

[116] C. Watson, F. Andermann, P. Gloor, M. Jones-Gotman, T. Peters, A. Evans, A. Olivier, D. Melanson, and G. Leroux. Anatomic basis of amygdaloid and hippocampal volume measurement by magnetic resonance imaging. *Neurology*, 42(9):1743–1750, 1992.

[117] J. L. Whitwell and C. R. Jack Jr. Comparisons between Alzheimer disease, frontotemporal lobar degeneration, and normal aging with brain mapping. *Topics in Magnetic Resonance Imaging*, 16(6):409–425, 2005.

[118] J. L. Whitwell, E. L. Sampson, C. T. Loy, J. E. Warren, M. N. Rossor, N. C. Fox, and J. D. Warren. VBM signatures of abnormal eating behaviours in frontotemporal lobar degeneration. *NeuroImage*, 35(1):207–213, 2007.

[119] A. J. Worth, N. Makris, V. S. Caviness Jr., and D. N. Kennedy. Neuroanatomical segmentation in MRI technological objectives. *International Journal of Pattern Recognition and Artificial Intelligence*, 11(8):1161–1187, 1997.

[120] I. C. Wright, P. K. Mcguire, J. . Poline, J. M. Travere, R. M. Murray, C. D. Frith, R. S. J. Frackowiak, and K. J. Friston. A voxel-based method for the statistical analysis of gray and white matter density applied to schizophrenia. *NeuroImage*, 2(4):244–252, 1995.

[121] C. Xu, D. L. Pham, M. E. Rettmann, D. N. Yu, and J. L. Prince. Reconstruction of the human cerebral cortex from magnetic resonance images. *IEEE Transactions on Medical Imaging*, 18(6):467–480, 1999.

[122] M. Xu, P. M. Thompson, and A. W. Toga. Adaptive reproducing kernel particle method for extraction of the cortical surface. *IEEE Transactions on Medical Imaging*, 25(6):755–767, 2006.

[123] J. Xuan, T. Adali, and Y. Wang. Segmentation of magnetic resonance brain image: integrating region growing and edge detection. *IEEE International Conference on Image Processing*, 3:544–547, 1995.

[124] H. Xue, L. Srinivasan, S. Jiang, M. Rutherford, A. D. Edwards, D. Rueckert, and J. V. Hajnal. Automatic segmentation and reconstruction of the cortex from neonatal MRI. *NeuroImage*, 38(3):461–477, 2007.

[125] P. A. Yushkevich, J. Piven, H. C. Hazlett, R. G. Smith, S. Ho, J. C. Gee, and G. Gerig. User-guided 3D active contour segmentation of anatomical structures: Significantly improved efficiency and reliability. *NeuroImage*, 31(3):1116–1128, 2006.

[126] X. Zeng, L. H. Staib, R. T. Schultz, and J. S. Duncan. Segmentation and measurement of the cortex from 3-D MR images using coupled-surfaces propagation. *IEEE Transactions on Medical Imaging*, 18(10):927–937, 1999.

[127] A. P. Zijdenbos and B. M. Dawant. Brain segmentation and white matter lesion detection in MR images. *Critical Reviews in Biomedical Engineering*, 22(5-6):401–465, 1994.

[128] B. Zitová and J. Flusser. Image registration methods: A survey. *Image and Vision Computing*, 21(11):977–1000, 2003.

Chapter 2

Extraction of the Cerebral Cortical Boundaries from MRI for Measurement of Cortical Thickness

Adapted from: S. F. Eskildsen, M. Uldahl and L. R. Østergaard: Extraction of the Cerebral Cortical Boundaries from MRI for Measurement of Cortical Thickness, Progress in Biomedical Optics and Imaging, vol. 5747, issue II, 2005, p. 1400-10.

2.1 Introduction

Several diseases degenerate the human cerebral cortex. One of the most common and fast developing neurodegenerative diseases is Alzheimer's disease (AD). Subtle, spatially localized atrophy may occur before the first clinical signs [2]. Knowledge on the earliest signs of atrophy and its initiating site in AD patients may accompany earlier and more accurate diagnosis of AD. Atrophy of the cerebral cortex may be quantified in vivo by measuring the volume or thickness of the cortex from a magnetic resonance imaging (MRI) scan, containing a series of cross-sectional images. Knowledge of cortical volume may indicate atrophy, but cannot reveal the exact site of atrophy as local thickness measurements can. Measurements of cortical thickness from a series of MRI images is complicated as it requires the images to be orthogonal onto the measured structure in order to avoid under- or over-estimates. In addition to this, the relatively low resolution and partial volume effects (PVE) may complicate an accurate definition of the cortical boundaries. Manual measurement of the cortical thickness is a tedious and time consuming process, and the manual measurements are likely to be biased to the operator due to the difficulty of defining the cortical boundaries. Hence, there is a need for fully automatic and objective methods.

Automatic measurements of the cortex requires an automatic delineation of the cortical boundaries. The cerebral cortex is a thin sheet of gray matter (GM), surrounding the cerebrum white matter (WM), and surrounded by cerebrospinal fluid (CSF). In this paper the WM/GM and GM/CSF crossings are referred to as the inner and outer boundary of the cortex respectively. The cortex is isomorph to a sphere, if closed at the brain stem [1]. Thus, advantageously, the boundaries may be represented as simple surfaces, isomorph to a sphere.

Segmentation algorithms based on deformable surfaces rely on a combination of high- and low-level information, which enables delineation of the boundary in areas where image edges are obscured or missing. Opposite banks of tight sulci may meet inside the sulcal

folds and appear as connected in MRI due to undersampling and artifacts. The main difficulty in cortical segmentation lies in correctly penetrating such sulci and reaching their fundi, as the true cortical thickness otherwise will be overestimated. MacDonald et al. [9] addressed this problem by deforming the inner and outer surface simultaneously under influence of intersection constraints and an inter-surface distance constraint, which drags the outer surface towards the fundi of sulci. However, a bias between the chosen predefined distance and the measured cortical thickness may exist [9].

A different approach to modeling the cortex without a distance constraint is taken by Dale et al. [5] In this approach, Dale et al. fit a surface to the inner boundary of the cortex, and inflates it towards the outer boundary of the cortex. The approach causes the surface to settle at approximately the midpoints of tight sulci when no CSF is evident between the sulcal banks, and constraints prevent the surface from self-intersecting. Clearly, the direction of inflation is important to the resulting outer surface. Dale et al. use the directions of the surface normals. However, such an approach requires the use of excessive smoothing to avoid the formation of non-existent folds, in the presence of small concavities, or noise in the inflating surface. Xu et al. [16] introduced an alternative to the direction of the surface normals with a generalized gradient vector flow (GGVF) force, which provides vectors pointing towards the nearest image boundary. Xu et al. used this force for extending the inner surface towards the *central* layer of the cortex. Xu et al. noted that their approach could be tailored to segmenting the GM/CSF boundary instead of the central layer. However, their approach does not impose self-intersection constraints, which is necessary when segmenting the outer boundary, nor is it fully automatic.

This paper presents a new method inspired by the work of Dale et al. [5] and Xu et al. [16] The method is capable of fully automatically extracting measurements of cortical thickness, volume and area from a T1-weighted MRI scan. The details of the method is described in the following section, and preliminary test results are presented in section 2.3.

2.2 Methods

The data used as input to the method are T1-weighted MRI scans encompassing the entire cerebrum. Tissue inhomogeneity artifacts in the MRI volumes are reduced using a method by Sled et al. [12], and the volumes are registered into a common reference space using a method by Collins et al. [4] The steps in the cortex extraction method is illustrated in figure 2.1. An initial surface is extracted from the T1-weighted MRI scan, and deformed to fit the inner cortical boundary. The resulting surface is then deformed to fit the outer cortical boundary. From these surface representations of the inner and outer cortical boundary, anatomical properties of the cortex, such as the thickness, can be obtained.

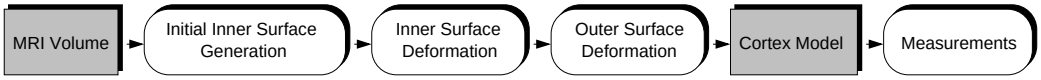

Figure 2.1: Pipeline of the method. Rounded boxes indicate processing steps. Gray boxes indicate data.

2.2.1 Initial Inner Surface Generation

A surface of the inner boundary of the cerebral cortex is generated by extracting the WM component of the cerebrum, and then performing a tessellation of this component. The steps are illustrated in figure 2.2.

The brain is extracted from the MRI volume using a brain extraction tool [13]. The result after applying the brain extraction tool is a volume consisting of the cerebrum,

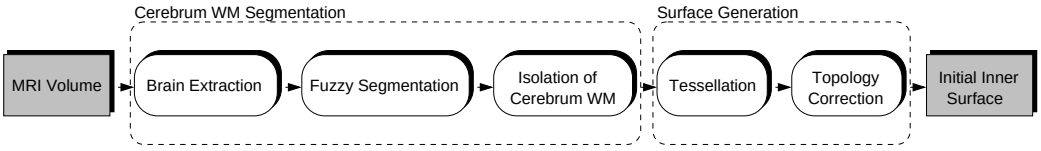

Figure 2.2: Process of generating the initial surface. Rounded boxes indicate processing steps. Gray boxes indicate data.

the cerebellum and the brain stem. To identify the WM voxels in the volume, the fuzzy c-means algorithm is applied [14]. The volume is divided into WM, GM, CSF and background, and the output of the algorithm is a membership volume for each class. The WM membership volume is used in the further procedure of generating the initial surface. To find the WM inside the cerebrum, the cerebrum is automatically separated from the cerebellum and brain stem, using morphological operations on the WM membership volume.

A tessellation of the cerebrum WM is performed using a simple iso-surfacing algorithm. The tessellation of the cerebrum WM may include handles or holes. To ensure that the tessellated surface is isomorph to a sphere, a topology correction algorithm by Han et al. [6] is applied to the tessellated surface of the cerebrum WM.

2.2.2 Inner Surface Deformation

The initial estimate of the inner boundary of the cerebral cortex is a surface close to the true WM/GM boundary. The purpose of the surface deformation is to smoothen the surface and adjust it to the correct tissue boundary. An active contour framework originally described by Kass et al. [8] is used to deform the surface. The deformation is made by iteratively moving the vertices to the positions, in a spherical search space, which result in the lowest energy level expressed by an energy function. The energy function must ensure that the energy minimum is situated where the surface fits the correct WM/GM boundary.

Internal and external energies are used to control the behavior of the deformable surface. The internal energies are applied to achieve a smooth characteristic of the surface and help keeping the vertices uniformly distributed on the surface. For this purpose a tension term and a flexural term are used. The tension term is an approximation of the Laplacian [10]:

$$E_{Laplacian} = \|\vec{L}(\vec{v})\|, \quad \text{where} \quad \vec{L}(\vec{v}) = \frac{1}{n}\sum_{i=0}^{n}\vec{v}_i - \vec{v}\ , \tag{2.1}$$

where $\vec{v}$ is a vertex in the surface, $\vec{v}_i$ is the ith neighbor to $\vec{v}$, and n is the number of neighboring vertices to $\vec{v}$. The flexural term is an approximation to the squared Laplacian [10]:

$$E_{squared\ Laplacian} = \left\| \frac{1}{n}\sum_{i=0}^{n}\vec{L}(\vec{v}) - \vec{L}(\vec{v}_i) \right\| \tag{2.2}$$

External energies are used to guide the surface towards the WM/GM boundary. Three different external energies are used, namely gradient, inflation and initial energy.

The gradient energy attracts the deforming surface to the WM/GM boundary when close to image edges of this boundary:

$$E_{gradient} = -\|\vec{\nabla} I(\vec{v})\|\ , \tag{2.3}$$

where $\vec{\nabla} I$ is the first derivative of the intensities in the MRI volume. The magnitude of

the gradient is used, as the energy function must return an energy level at a given position, not a vector.

The fuzzy membership values and the directions of the surface normals are used to displace the surface towards the correct tissue boundary. If a vertex in the surface is placed in WM, the vertex is displaced in the direction of the surface normal. Contrary, if the vertex is placed outside WM, the vertex is displaced in the opposite direction of the surface normal. The WM membership is assumed to equal or to be close to the GM membership when exactly on the GM/WM boundary, but to differ significantly from the GM membership when far from the boundary. The inflation energy has no influence whenever the difference between the WM and GM memberships is between the thresholds $-T$ and T:

$$E_{inflation} = \begin{cases} -(\vec{n}(\vec{v}) \cdot \vec{D}), & \text{if } \mu_{WM}(\vec{v}) - \mu_{GM}(\vec{v}) > T & \textit{(In WM)} \\ -(-\vec{n}(\vec{v}) \cdot \vec{D}), & \text{if } \mu_{WM}(\vec{v}) - \mu_{GM}(\vec{v}) < -T & \textit{(In GM)} \\ 0, & \text{otherwise} & \textit{(Border region)}, \end{cases}$$

where $\vec{n}(\vec{v})$ is the unit surface normal at vertex $\vec{v}$, $\vec{D}$ describes the direction of the movement of $\vec{v}$, and μ is the membership values from the fuzzy segmentation. The expression is negated to yield a low energy whenever the inner product between $\pm\vec{n}$ and $\vec{D}$ is high.

The initial surface is generally a good estimate of the WM/GM boundary. Therefore, an energy penalizing large deviations from the initial surface is introduced:

$$E_{initial} = g(|\vec{v}_{initial} - \vec{v}_{deforming}|), \tag{2.4}$$

where $\vec{v}_{initial}$ is a vertex in the initial surface and $\vec{v}_{deforming}$ is the corresponding vertex in the deforming surface. g is a weighting function controlling the extent of a range R where the energy has no influence. This range is necessary as the initial surface is only an approximation. g is defined as:

$$g(x) = \begin{cases} |x - R|^2 & \text{, if x} > \text{R} \\ 0 & \text{, otherwise} \end{cases} \tag{2.5}$$

The complete energy function used for the deformation of the inner surface is:

$$\begin{aligned} E_{inner} \quad = \quad & c_1 E_{Laplacian} + c_2 E_{squared\ Laplacian} \\ & + c_3 E_{gradient} + c_4 E_{inflation} + c_5 E_{initial}, \end{aligned} \tag{2.6}$$

where $c_1 ... c_5$ are weights. This function is an expression of the energy level of a single position in the search space of a vertex. The greedy algorithm by Williams et al. [15] is used to find the minimum energy position in the search space of each vertex. The vertices are moved in this way until the number of vertices moved during an iteration is below a given threshold, where equilibrium is assumed. The used search space is spherical containing 26 different positions.

Two hard constraints are applied to the surface during deformation; one that ensures a certain minimum distance between neighboring vertices, and one that prevents the surface from self-intersecting.

2.2.3 Outer Surface Deformation

The inner surface is used as the initial estimate of the outer cortical boundary. As mentioned in the introduction, the image edges of the outer boundary in tight sulcal folds cannot always be observed in MRI scans. As the cortex has approximately the same convexity and concavity as the WM, tight sulcal folds can be modeled by displacing the inner surface in the direction of the surface normals. This is done using an inflation energy similar to the one used in the inner surface deformation. If a vertex is located in WM or GM, the vertex is displaced in the direction of the surface normal, otherwise it is displaced

in the opposite direction:

$$E_{inflation} = \begin{cases} -(\vec{n}(\vec{v}) \cdot \vec{D}), & \text{if } \mu_{GM}(\vec{v}) + \mu_{WM}(\vec{v}) \geq \mu_{CSF} \quad \textit{(In WM or GM)} \\ -(-\vec{n}(\vec{v}) \cdot \vec{D}), & \text{otherwise} \quad \textit{(In CSF)} \end{cases}$$

A hard constraint prevents the surface from self-intersecting in sulci where no CSF is evident in-between the sulcal banks. This causes the inflation energy to collapse walls of tight sulcal folds at a position approximately equidistant to the inner surface, when no CSF is evident (see figure 2.3). However, the inflation energy may erroneously collapse

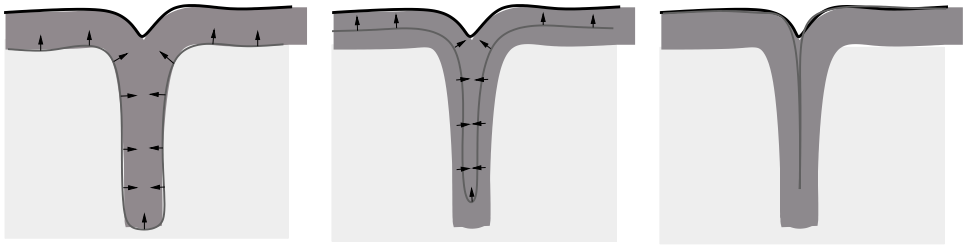

(a) Initial (b) Deforming (c) Final

Figure 2.3: Example of how the inflation force enables modeling of narrow sulci with no CSF evident. The gray solid line indicates the deformable surface, which approaches the GM/CSF boundary from the WM/GM boundary. As the deformable surface is pushed in the direction of the local surface normals, it will eventually meet itself inside deep narrow sulci.

the surface in small concavities, and for example model non-existent folds on top of gyri. Increasing the influence of the internal energies resolves these problems, but also impairs the ability of the surface to conform to curved regions on the outer boundary. To overcome this tradeoff, an energy displacing the surface directly towards the GM/CSF image edge is included in the energy function. This energy has the effect of unfolding concavities on the deforming surface when no outer surface concavities is evident in the image data, and thus avoids forming non-existent folds in the surface. A proper weighting between this energy and the inflation energy causes tight sulcal folds to collapse and small concavities to be unfolded, while capturing the GM/CSF image edge. The energy uses a GGVF field by Xu et al. [16] The components of the GGVF field point towards edges in a given edge map. In order to ensure that the GGVF field points towards the outer boundary, the edge map is calculated by taking the first derivative of the sum of the WM and GM fuzzy memberships (see figure 2.4). The GGVF energy is the inner product between the normalized GGVF field vector $\vec{G}$ and the normalized direction vector $\vec{D}$:

$$E_{GGVF} = -\vec{G}(\vec{v}) \cdot \vec{D} \tag{2.7}$$

When close to the edge defined by the edge map, the GGVF energy is switched to a gradient energy calculated from the MRI data. This switch is made when the difference between the CSF and GM membership value goes below a given threshold ρ:

$$E_{GGVF} = \begin{cases} -\vec{G}(\vec{v}) \cdot \vec{D} & \text{, if } |\mu_{CSF} - \mu_{GM}| \geq \rho \\ -\|\vec{\nabla} I(\vec{v})\| & \text{, otherwise} \end{cases} \tag{2.8}$$

The same internal energies is used for the deformation of the outer surface as those used for the inner surface. The complete energy function used for the deformation of the outer surface is:

$$E_{outer} = c_6 E_{Laplacian} + c_7 E_{squared\ Laplacian} + c_8 E_{inflation} + c_9 E_{GGVF}, \tag{2.9}$$

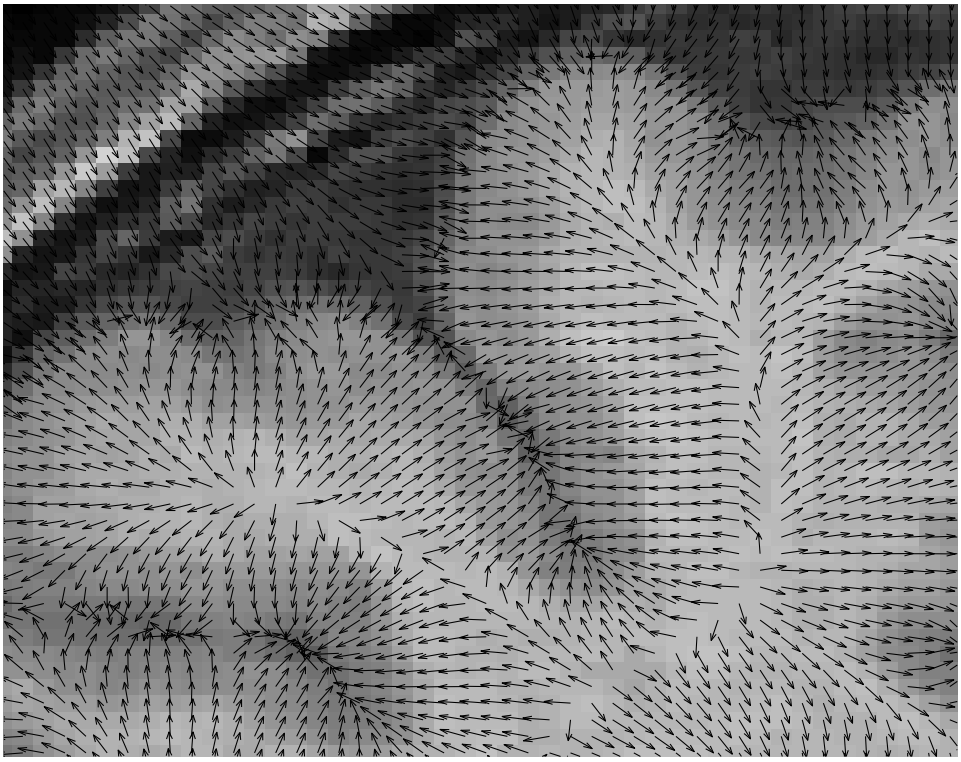

Figure 2.4: Example of a GGVF field based on an edge map calculated from the sum of the WM and GM memberships using the first order derivative.

where $c_6 ... c_9$ are weights.

2.2.4 Measurements

Having the inner and outer boundary of the cortex represented as closed surfaces, it is possible to obtain a variety of measurements, such as volume, area and thickness. However, in this paper the focus is on the cortical thickness. The thickness is measured as the shortest distance from a given vertex on the outer surface to the face of the inner surface (not necessarily being a vertex). A thickness measurement is obtained at each vertex of the outer surface.

2.3 Results

The generated surfaces contain approximately 200.000 vertices each. The entire extraction of the cortical boundaries requires less than one hour on a 2.8GHz Pentium 4 processor, although the deformation process alone is done in less than 10 minutes.

The method was tested on six simulated MRI scans of a brain phantom [3] with respectively 0%, 1%, 3%, 5%, 7% and 9% of noise added, and an isotropic voxel size of 1.00mm. Surfaces representing the GM/CSF tissue boundary were extracted for all datasets, and the surface of the dataset without noise was used as a reference in order to facilitate a comparison. The comparison was made by calculating the distance to the nearest vertex on the reference surface for all vertices on each of the remaining surfaces. The mean distances and standard deviations are reported in table 2.1. Only a small increase in error, measured as mean distance, is the result when the noise level is increased from 1% to 9%.

1%	3%	5%	7%	9%
0.27mm (0.22)	0.31mm (0.26)	0.34mm (0.27)	0.37mm (0.30)	0.41mm (0.33)

Table 2.1: Mean distance to nearest vertex on reference surface and standard deviations.

To assess the robustness of the method, thickness measurements of the same subject, scanned at two different sessions on the same scanner were compared. First session voxel size was 0.89x0.89x2.00mm, and the second session voxel size was 0.86x0.86x2.00mm. The difference in mean cortical thickness between the first and second scan was 0.01mm. To investigate these subtle deviations, a vertex to vertex comparison of the cortical thickness for the two scans was done by calculating the deviation in cortical thickness for corresponding vertices (using nearest point correspondence) on the GM/CSF surfaces of the two scans. The mean deviation was found to 0.33mm with a standard deviation of 0.27mm.

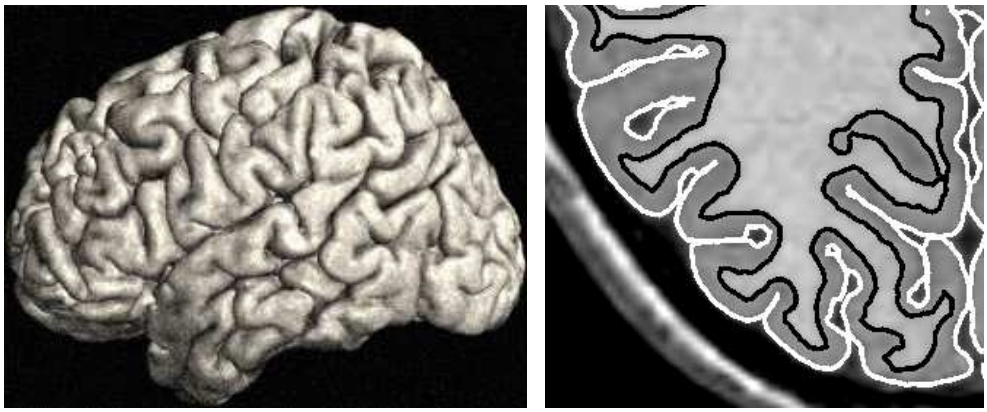

(a) Rendering of the outer cortical surface.

(b) Intersections of inner and outer cortical surfaces with MRI data.

Figure 2.5: Visualization of the extracted inner and outer cortical surfaces of an ICBM subject.

The method was applied to 38 T1-weighted MRI scans of healthy subjects acquired from the ICBM database [7]. These data have an isotropic voxel size of 1.00mm. A visual inspection of surface/data intersections for all 38 datasets revealed few visible errors (see figures 2.5 and 2.6). The mean cortical thickness for the 38 subjects was measured to 2.59mm (0.15mm). This is within the range of what was measured in a post-mortem study by Pakkenberg et al. [11], where the mean thickness in the four main lobes were measured to be in the range 2.16mm to 2.88mm. The cortical thickness of the 38 subjects was color mapped onto the outer cortical surface. An example of this, converted to grayscale, is shown in figure 2.7. As it can be observed from the figure, the cortex is measured to be thickest in the frontal and temporal regions, and thinnest in the occipital and parietal regions. This was the case of all 38 subjects, and is consistent with normal anatomical findings. Even though the pattern of thick frontal and temporal lobes, and thin parietal and occipital lobes can be recognized in all subjects, inter-subject variations exist in the cortical thickness. Figure 2.8 illustrates this by the thickness map of 16 healthy subjects seen from the top.

To evaluate the method on a brain with an abnormal morphology, cortical thickness measurements were obtained from two MRI scans of an Alzheimer's patient with severe atrophy acquired six months apart. These data have an isotropic voxels size of 0.9 mm, however, the contrast is lower than the ICBM data. The method succeeded in capturing the inner and outer cortical surfaces of the brain with abnormal morphology, and the thickness measurements indicated a small decrease in mean cortical thickness from 2.02

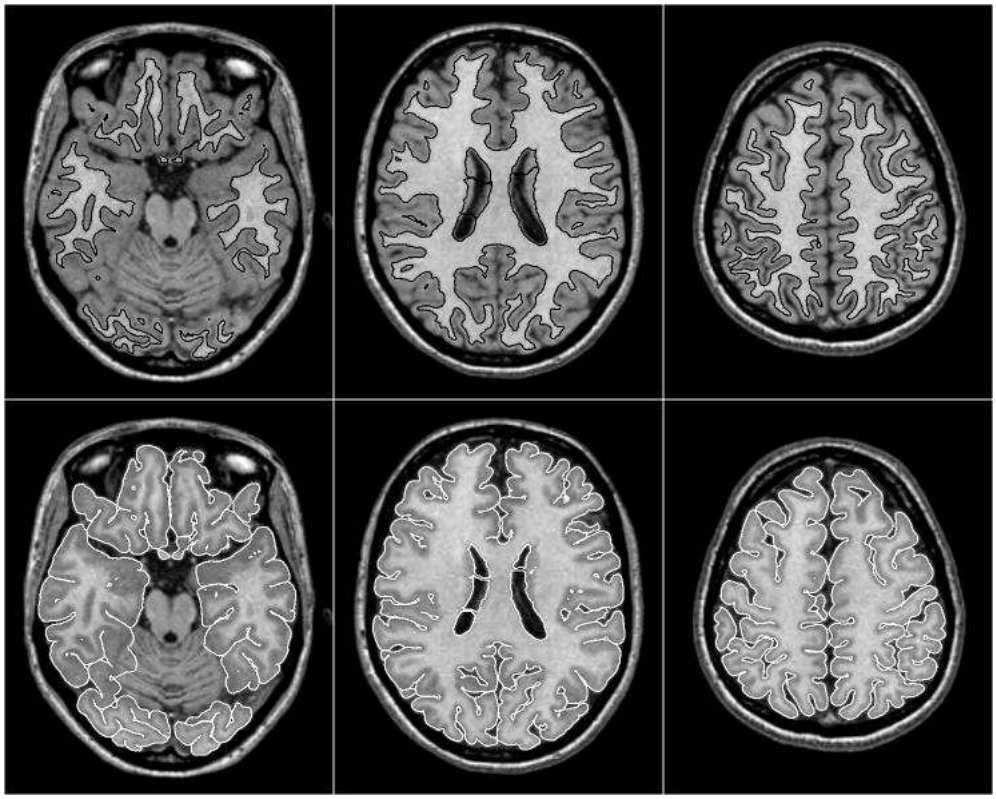

Figure 2.6: Intersections of inner and outer surfaces with MRI data of an ICBM subject. Top row: Inner surface. Bottom row: Outer surface. A few errors are visible in the images of second column, where the surfaces are penetrating both ventricles. These errors originate from the topology correction algorithm, that enforces a closed genus zero surface.

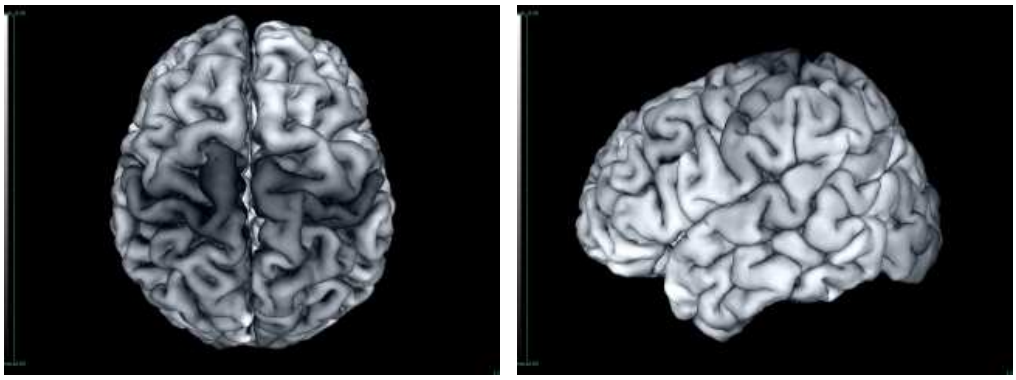

(a) Top view (b) Left view

Figure 2.7: Cortical thickness mapped onto the outer cortical surface as gray levels. Dark regions are thin, while bright regions are thick, ranging from 0 mm to 6 mm.

mm to 1.89 mm. Figure 2.9 shows the cortical thickness measurements extracted from the two scans, mapped onto the outer cortical surfaces as gray levels. The small decrease in cortical thickness can be observed from the surfaces by a faintly darker texture on the second surface.

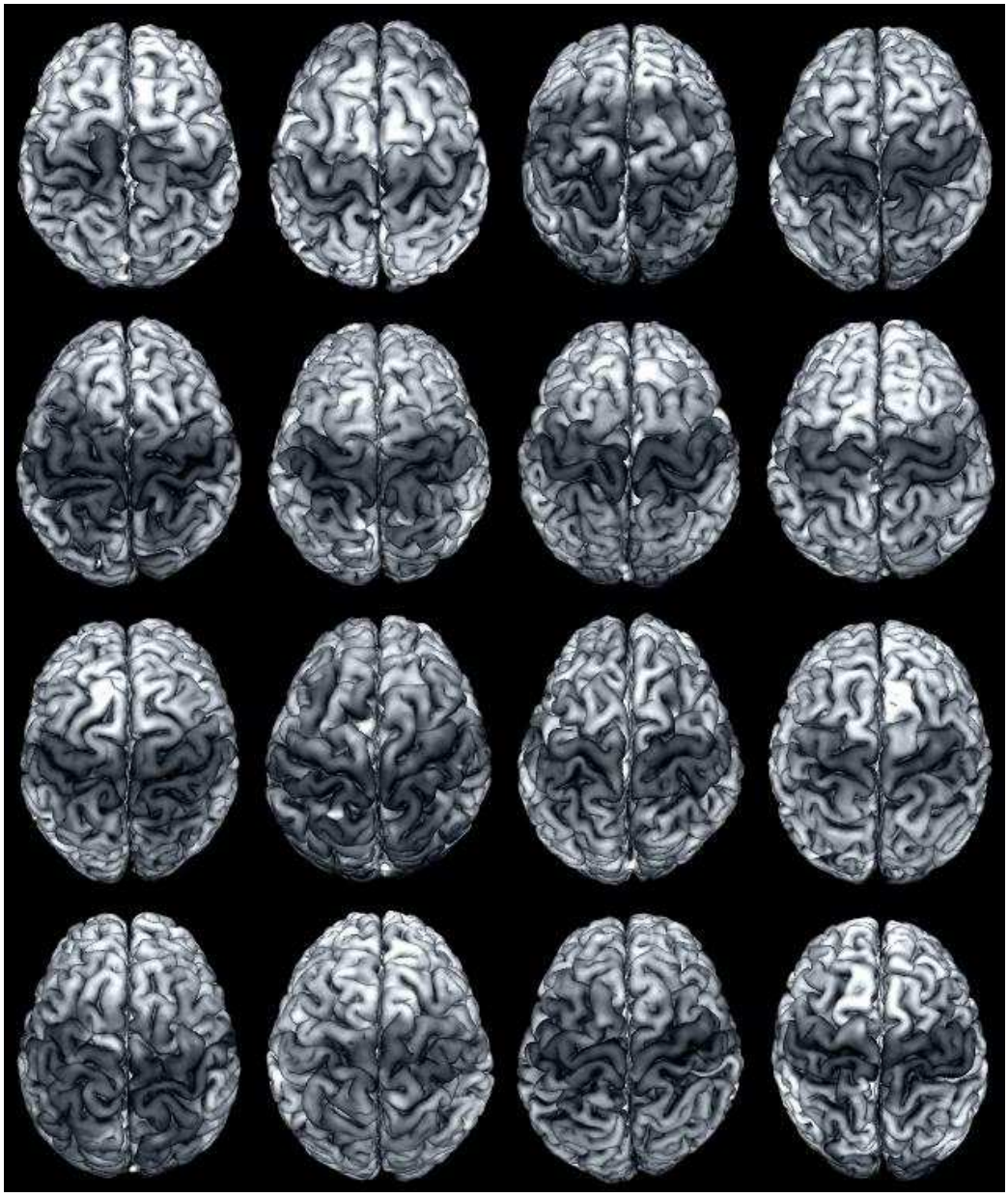

Figure 2.8: The thickness pattern of 16 ICBM subjects seen from the top.

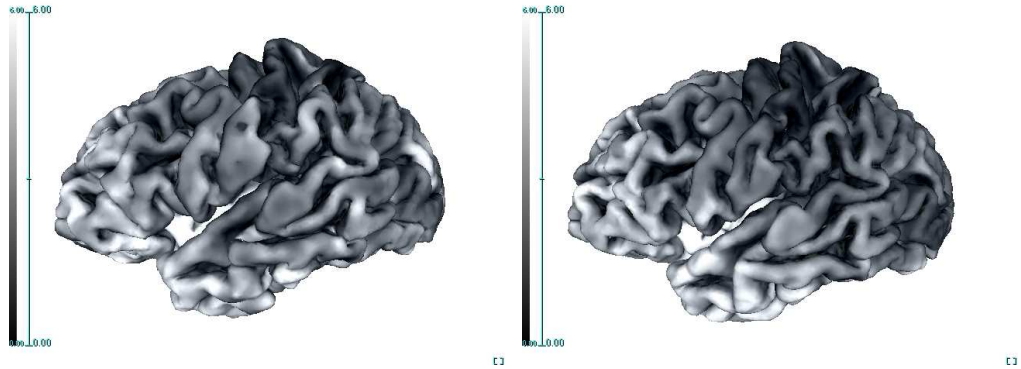

(a) Time point 1 (b) Time point 2

Figure 2.9: Cortical thickness at two time points (The color scale ranges from 0 mm (black) to 6 mm (white)).

2.4 Conclusion

This paper presented a new fully automatic method for segmenting the inner and outer boundaries of the human cerebral cortex from MRI data. The method is based on a deformable surface framework, and incorporates a new combination of energies in the energy function. The accurate initial surface speeds up the overall extraction process, as fewer iterations are necessary in the deformation process, and increases the probability of locating the correct minimum of the energy function.

The tests conducted on a simulated brain phantom with various degrees of noise added, showed that increased image noise only influences the sub-voxel accuracy of the method. This, along with the test/retest experiment, suggests that the method is robust to changes in image noise and other image artifacts.

Preliminary tests have been conducted on neuroanatomical data of normal brains and brains with severe atrophy at different time points. Results of these tests show that the method is fast, robust and accurate for segmenting the cortical boundaries. The thickness measurements conducted on normal subjects are close to post-mortem measurements, and the relative thickness between the major lobes are in accordance with the known anatomy of the brain. The inter-subject variability in the cortical thickness patterns, found among the normal subjects (illustrated in figure 2.8), indicates that knowledge of this variability must be obtained in order to discern normal and abnormal anatomy. The results obtained from the Alzheimer's subject indicate that the method is capable of tracking progression of atrophy in Alzheimer's patients.

In the near future, we intend to apply the method on a large collection of MRI scans of Alzheimer's patients, and a collection of longitudinal data from Alzheimer's patients. This data material give us the opportunity to investigate the possibility of tracking the progression of cortical atrophy. Furthermore, we intend to create statistical models of both Alzheimer's and normal brains based on the data material. With this, we hope to get indications of which anatomical markers could be relevant in the identification of Alzheimer's patients.

Acknowledgements

The data material of normal healthy subjects was provided with courtesy of the International Consortium of Brain Mapping. The data material of the Alzheimer's subject was provided with courtesy of Centre for Magnetic Resonance, University of Queensland,

Australia. The brain phantom used in the robustness test was provided with courtesy of McConnell Brain Imaging Centre, Montréal Neurological Institute, McGill University. The authors thank these institutions for their contribution. The authors also thank Center for Functionally Integrative Neuroscience, Aarhus University, Denmark, for their cooperation and funding.

References

[1] L. Abrams, D. E. Fishkind, and C. E. Priebe. A proof of the spherical homeomorphism conjecture for surfaces. *IEEE Transactions on Medical Imaging*, 21(12):1564–1566, 2002.

[2] G. Chetelat and J.-C. Baron. Early diagnosis of alzheimer's disease: contribution of structural neuroimaging. *NeuroImage*, 18:525–541, 2003.

[3] D. Collins, A. Zijdenbos, V. Kollokian, J. Sled, N. Kabani, C. Holmes, and A. Evans. Design and construction of a realistic digital brain phantom. *IEEE Transactions on Medical Imaging*, 17(3):463–468, June 1998.

[4] D. L. Collins, A. P. Zijdenbos, T. Paus, and A. C. Evans. Use of registration for cohort studies. Technical report, Montreal Neurological Institute, McGill University, 2000.

[5] A. M. Dale, B. Fischl, and M. I. Sereno. Cortical surface-based analysis i: Segmentation and surface reconstruction. *NeuroImage*, 9:179–194, 1999.

[6] X. Han, C. Xu, U. Braga-Neto, and J. L. Prince. Topology correction in brain cortex segmentation using a multiscale, graph-based algorithm. *IEEE Transactions on Medical Imaging*, 21(2):109–121, 2002.

[7] ICBM. *International Consortium for Brain Mapping.* http://www.loni.ucla.edu/ICBM/, 2002.

[8] M. Kass, A. Witkin, and D. Terzopoulos. Snakes: Active contour models. *International Journal of Computer Vision*, 1988.

[9] D. MacDonald, N. Kabani, D. Avis, and A. C. Evans. Automated 3-D extraction of inner and outer suraces of cerebral cortex from mri. *NeuroImage*, 12:340–356, 2000.

[10] T. McInerney and D. Terzopoulos. Topology adaptive deformable surfaces for medical image volume segmentation. *IEEE Transactions on Medical Imaging*, 18(10):840–850, 1999.

[11] B. Pakkenberg and H. J. G. Gundersen. Neocortical neuron number in humans: Effect of sex and age. *Journal of Comparative Neurology*, (384):312–320, 1997.

[12] J. G. Sled, A. P. Zijdenbos, and A. C. Evans. A non-parametric method for automatic correction of intensity non-uniformity in mri data. *IEEE Transactions on Medical Imaging*, 17(1):87–97, 1998.

[13] S. M. Smith. Fast robust automated brain extraction. *Human Brain Mapping*, 17(3):143–155, 2002.

[14] J. S. Suri, S. Singh, and L. Reden. Computer vision and pattern recognition techniques for 2-D and 3-D MR cerebral cortical segmentation(part I): A state-of-the-art review. *Pattern Analysis and Apllications*, 5:46–76, 2002.

[15] D. J. Williams and M. Shah. A fast algorithm for active contours. In *Third International Conference on Computer Vision*, 1990.

[16] C. Xu, D. L. Pham, M. E. Rettmann, D. N. Yu, and J. L. Price. Reconstruction of the human cerebral cortex from magnetic resonance images. *IEEE Transactions on Medical Imaging*, 18(6):467–480, 1999.

Chapter 3

Active Surface Approach for Extraction of the Human Cerebral Cortex from MRI

Adapted from: Simon F. Eskildsen and Lasse R. Østergaard: Active Surface Approach for Extraction of the Human Cerebral Cortex from MRI, MICCAI 2006, Lecture Notes in Computer Science, 4191, pp. 823-830, October, 2006.

3.1 Introduction

During the last decade, several methods for extracting the boundaries of the human cerebral cortex from magnetic resonance imaging (MRI) have been proposed [1,3,5–8,10,11]. The segmentation of the cerebral cortex may facilitate extraction of important anatomical features, such as the cortical thickness, which may be utilised in studying the progress of a long list of neurodegenerative diseases, and in turn may aid in diagnosing these diseases. Furthermore, anatomical models of the cortex may be useful in connection with surgery simulation, preoperative planning, and postoperative evaluation.

The human cerebral cortex is a complex, highly convolved sheet-like structure. In MRI the cortical boundaries are often obscured or partly missing because of poor contrast, noise, inhomogeneity artifacts and partial volume averaging originating from the acquisition. Opposite banks of tight sulci on the outer boundary may meet inside the sulcal folds and appear as connected in MRI. Active surfaces have the ability to compensate for obscured and incomplete image edges. However, in brain MRI, information of the outer cortical boundary may be completely missing in several tight sulci. The most promising methods for delineating the outer boundary use information of the white matter/grey matter (WM/GM) boundary to fit the surface to the outer cortical boundary. MacDonald et al. used a coupled surface approach, where the inner and outer surface simultaneously were deformed under proximity constraints maintaining a predefined minimum and maximum distance between the inner and outer boundary [7]. Zeng et al. also used the coupled surfaces approach in a level set framework [11]. The coupled surfaces approach has the advantage of explicitly using information of both cortical boundaries to detect the outer boundary. This solves the problem of penetrating the deep narrow sulci. The drawbacks are the computational expense, and the constraints of a predefined distance, which may prevent the detection of abnormal thin or thick areas of the cortex. Kim et al. proposed a modification to the method by MacDonald et al. which does not contain a coupled surface constraint [6]. This method has shown promising results.

Another approach by Dale et al. identified the inner cortical boundary, and expanded this surface towards the outer boundary [3]. This has the advantage that all sulci are

present in the initial state, and enables the preservation of the sulci during deformation, even though the evidence of the outer boundary may be missing in the MRI data. The tight sulcal folds are modelled by preventing self-intersections in the deforming surface, thus the delineation of the folds is placed equidistant from the sulcal walls of the inner boundary. This single surface approach is fast and captures all the tight sulci. However, the expansion of the surface towards the outer boundary is sensitive to small errors or irregularities in the initial surface, which may lead to modelling of non-existent sulci. Xu et al. used a Generalised Gradient Vector Flow (GGVF) to define a direction toward the central layer of the cortex [10]. This solution provided a fast and consistently convergence of the surface, but tight sulci with no evidence of the outer boundary were not captured by this method. Recent work by Han et al. expands the surface from the central layer toward the outer boundary using a topology-preserving geometric deformable model [5]. In this approach the GGVF is only included in the model when reconstructing the central cortical layer.

This paper presents an active surface approach for cortex extraction characterised by the inclusion of a GGVF in the extraction of the outer cortical boundary and the use of a local weighting strategy based on the intrinsic properties of the deforming surface.

3.2 Methods

The strategy for reconstructing the cerebral cortex is to first extract the inner boundary, and then displace this surface towards the outer boundary under the influence of internal and external forces. The inner boundary is extracted using the method disclosed in our earlier work [4] ensuring a surface topology of a sphere. The following explains the deformation that fits a surface to the outer cortical boundary using a surface estimating the inner boundary.

3.2.1 Deformation Process

The active surface is a non-parametric triangular mesh. The surface is deformed by iteratively updating each vertex with a vector defined as the sum of deformation forces. This deformation scheme has the advantage of being fast ($O(n)$) and eliminates problems regarding granularity, which is found in discrete methods. Even though convergence may be fast, absolute equilibrium is never reached, due to the iterative nature of the algorithm. Therefore, a threshold for the update vector is given that defines whether or not a vertex has moved during an iteration. The stop criterion is met when a sufficiently small number vertices are displaced during an iteration.

During surface deformation the surface is remeshed at prespecified intervals using a simple mesh adaption algorithm. The remeshing is based on the vertex density of the surface. This is done to avoid clustering of vertices and allowing the surface to expand where necessary, i.e. the distribution of vertices are kept uniform throughout the surface. The surface remeshing algorithm does not change the topology of the surface, but is allowed to alter the surface geometry. Finally, the surface is prevented from self-intersecting during deformation using the same principle as described in [3].

3.2.2 Internal Forces

Internal forces are applied to keep the vertices well-distributed and achieve a smooth characteristic of the surface. The internal forces used in this paper are similar to conventional smoothing forces [1,8] in form of a tensile and a flexural force. The tensile force is calculated by an approximation of the Laplacian [8]:

$$\vec{L}(i) = \frac{1}{m} \sum_{j \in N(i)} \vec{x}(j) - \vec{x}(i) \ , \tag{3.1}$$

where $\vec{x}(i)$ is the position of vertex i, $N(i)$ are the neighbour vertices to i, $\vec{x}(j)$ is the position of i's neighbour j, and m is the number of vertices in $N(i)$. The flexural force is calculated by an approximation of the squared Laplacian [8]:

$$\vec{L^2}(i) = \frac{1}{m} \sum_{j \in N(i)} \vec{L}(\vec{x}(j)) - \vec{L}(\vec{x}(i)) \tag{3.2}$$

Both $\vec{L}$ and $\vec{L^2}$ are decomposed into a tangential and a normal component of the force vector as in the method of Dale et al. [3]. This enables adjustment of the contractive effect of the internal forces by weighting each component.

The internal forces have the effect of smoothing and flattening the surface, however, as the target boundary is highly convolved with both peaked and flat areas, the internal forces should be relaxed in certain areas of the surface and increased in others. The deforming surface is used as a reference for the curvature of the target boundary to obtain local curvature weighting of the internal forces. To enable the surface to compensate for errors in the initial surface, and facilitate some degree of surface curvature alteration, the curvature values are recalculated at prespecified intervals during the deformation process. The curvature is estimated at each vertex of the deforming surface using the expression:

$$\rho(i) = \begin{cases} \sigma(i) & , if \quad \vec{w}(i) \cdot \vec{n}(i) \leq 0 \\ -\sigma(i) & , otherwise \end{cases} \tag{3.3}$$

$$\sigma(i) = \frac{1}{m} \sum_{j \in N_g(i)} \pi - 2cos^{-1} \left(\frac{\vec{x}(j) - \vec{x}(i)}{|\vec{x}(j) - \vec{x}(i)|} \cdot \vec{w}(i) \right), \tag{3.4}$$

where $N_g(i)$ is a geodesic neighbourhood around vertex i, $\vec{w}(i)$ is a unit vector pointing from i towards the centre of gravity of $N_g(i)$, $\vec{n}(i)$ is the unit vector normal at i, and m is the number of vertices in $N_g(i)$. Curvature values of zero are found in flat areas, positive values in convex areas and negative values in concave areas. Note that the size of N_g has great influence on the curvature values and should be chosen carefully. The curvature values are Gaussian filtered ($\sigma = 1$), normalised, and in this form used to weight the internal forces:

$$\vec{\hat{u}}_{int}(i) = f(\rho(i))\vec{u}_{int}(i), \tag{3.5}$$

where f is a weighting function defined as

$$f(x) = 1 - \frac{1}{2} tan(|x|), x \in [-1; 1] \tag{3.6}$$

3.2.3 External Forces

The outer boundary of the cerebral cortex follows approximately the same convexities and concavities as the inner cortical boundary. Hence, a surface delineating the inner cortical boundary is used as an initial estimate of the outer cortical boundary. This inner surface is displaced in the direction of the local surface normals until the surface meets itself (see figure 3.1), and thereby model sulci, even though only little or no image information is available. For this purpose a pressure force [1] is used. The force is similar to the external force used in [3, 8], but based on fuzzy memberships of the tissue classes as described in [10]. The fuzzy memberships are calculated using the fuzzy c-means algorithm [9]. The pressure force is expressed as:

$$\begin{aligned} \vec{p}(i) &= \Delta\mu(i)\vec{n}(i) \\ \Delta\mu(i) &= \mu_{WM}(i) + \mu_{GM}(i) - \mu_{CSF}(i), \end{aligned} \tag{3.7}$$

where μ is the membership values (trilinearly interpolated) and $\vec{n}(i)$ is the unit vector normal at vertex i. A weighting function is applied to the membership difference to

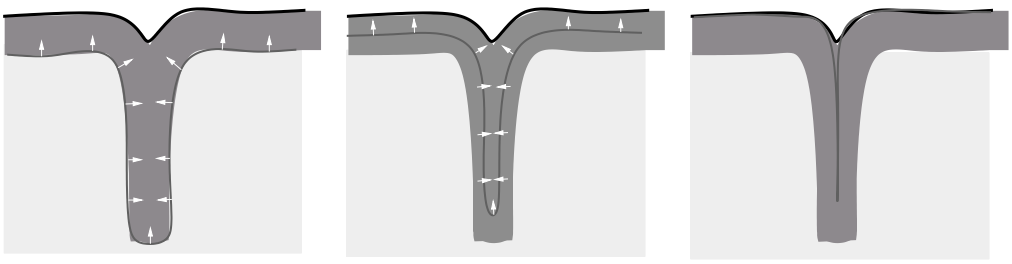

(a) Initial (b) Deforming (c) Final

Figure 3.1: Illustration of how the pressure force enables modelling of narrow sulci with no CSF evident. As the deformable surface (grey line) is pushed away from the WM/GM boundary in the direction of the local surface normals, it will eventually meet itself inside narrow sulci.

ensure a degree of freedom at membership differences close to zero:

$$\vec{p}(i) = c_1 g(\Delta\mu(i))\vec{n}(i), \tag{3.8}$$

where c_1 is a weighting constant and

$$g(x) = x(2 - 2cos(x)), x \in [-1 : 1] \tag{3.9}$$

Surface normals, approximated from a discrete mesh, may be misleading, as they can be perturbed by noise in the surface. This may erroneously cause modelling of non-existing features, when the surface is displaced over larger distances. Increasing the influence of the internal forces resolves this problem, but also prevents the surface from reaching small concavities, which are truly evident in the MRI. To solve the problem, the pressure force is combined with a GGVF force similar to the one used by Xu et al. [10], but with an edge map of the outer cortical boundary instead of the central cortical layer. This edge map is the first order derivative of the sum of the WM and GM fuzzy memberships. The GGVF force performs best at the gyri where information of the GM/CSF boundary is evident in the MRI, thus the normal vector is combined with the GGVF vector so the GGVF vector dominates the normal vector at the crown and ridges of gyri, and the normal vector dominates the GGVF vector along the fundi, and walls of sulci. The local surface curvature, calculated in a geodesic neighbourhood, is used for balancing the influence of the GGVF vector and the normal vector:

$$\vec{u}_{ext}(i) = c_2 \left(\vec{p}(i)\frac{1-\rho(i)}{2} + \vec{g}(i)\frac{1+\rho(i)}{2} \right), \tag{3.10}$$

where $\vec{p}(i)$ is the pressure force vector at vertex i, $\vec{g}(i)$ is the GGVF vector at vertex i, $\rho(i)$ is the curvature value at i given in (3.3), and c_2 is a constant.

Gradient information is used to scale the update vector $\vec{u}$, so the magnitude of the update vector is reduced when the magnitude of the gradient increases. This is done by mapping the normalised gradient magnitudes with the function:

$$h(x) = cos(\frac{\pi}{2}x), x \in [0 : 1] \tag{3.11}$$

and scaling the update vector $\vec{u}$ by the result. The update vector is unchanged when there is no gradient and greatly shortened when a strong gradient is present at the given vertex position. Information of the gradient is used only when close to the GM/CSF boundary and suppressed when far from the boundary. The weighted membership difference $g(\Delta\mu(i))$ in (3.8), that provides an estimate for the spatial position of the GM/CSF

boundary, is therefore utilised to weight the influence of the gradient. The resulting update vector is given as a weighted sum of a gradient weighted term and a non-gradient weighted term:

$$\begin{aligned} &\vec{u}(i) = ((1-\tau)cos\left(\tfrac{\pi}{2}|\vec{\nabla}(i)|\right) + \tau)(\vec{\hat{u}}_{int}(i) + \vec{u}_{ext}(i)), \\ &\tau = |g(\Delta\mu(i))|, \end{aligned} \tag{3.12}$$

where $\vec{\nabla}(i)$ is the image gradient trilinearly interpolated at vertex i, $\vec{\hat{u}}_{int}(i)$ is the weighted sum of the internal forces given in (3.5), and $\Delta\mu(i)$ is given in (3.7).

3.3 Results

Simulated MRI scans of a brain phantom[1] [2] and 36 T1 weighted MRI datasets of young normal subjects from the International Consortium for Brain Mapping (ICBM) database were used for testing the general behaviour of the deformation. The same weighting constants were used in all test cases. Initial surfaces isomorph to a sphere were generated and fitted to the inner cortical boundary. The initial surfaces consisted of approximately $1.5 \cdot 10^5$ vertices. During deformation this number was increased to approximately $2.0 \cdot 10^5$. The deformation process converged after 30-40 iterations with the stop criterion of (#moved vertices) $<$ (1% of total vertices). The deformation of the outer surface required approximately 20 minutes on a 3 GHz Pentium 4 processor. The self-intersection tests performed throughout the deformation of the inner and outer surface were responsible for the majority of the processing time.

Figure 3.2 shows three different modes of the deformation process in a selected part of the simulated MRI. The three modes differ in their external forces, the internal forces are the same for all three modes. In the first mode, only the pressure force is enabled, simulating the method by Dale et al. [3]. This clearly shows that the use of the pressure force alone result in irregularities in the surface. This is especially evident at top of gyri. In the second mode, only the GGVF force is enabled, simulating the method by Xu et al. [10]. In this case the surface does not reach the fundus of sulci without evidence of CSF. There is also an undesirable behaviour in some of the sulci, because the surface is attracted to the nearest visible GM/CSF image edge. The last mode shows deformation with both the pressure force and the GGVF force enabled, balanced using the curvature weighting function. Now the tight sulci are being modelled correctly while avoiding surface irregularities on top of gyri.

All 36 cortices from the ICBM database were automatically reconstructed and qualitatively assessed by visual inspection. An example of an extracted outer surface is shown in figure 3.3. As it can be seen from the figure, the extracted surface appears smooth, realistic and major gyri and sulci are easily recognised. The qualitative assessment of the accuracy of the extracted surfaces was made by superimposing the surfaces onto the MRI and visually inspecting the contours (figure 3.3, right). As it can be observed from the figure the outer cortical boundary is accurately delineated. Tight sulci are modelled even when the crowns of adjacent gyri are not separated in the image data, and the surface tend to be placed at a position equidistant to the WM walls when no CSF is evident in sulci. This indicates that the method follows the intended behaviour.

3.4 Summary and Conclusion

This paper presented a new method for extracting the outer boundary of the human cerebral cortex from MRI. The active surface approach combines a conventional pressure force with fuzzy tissue classifications, and a generalised gradient vector flow force, while locally

[1] The brain phantom was provided by the McConnel Brain Imaging Centre at the Montreal Neurological Institute, http://www.bic.mni.mcgill.ca

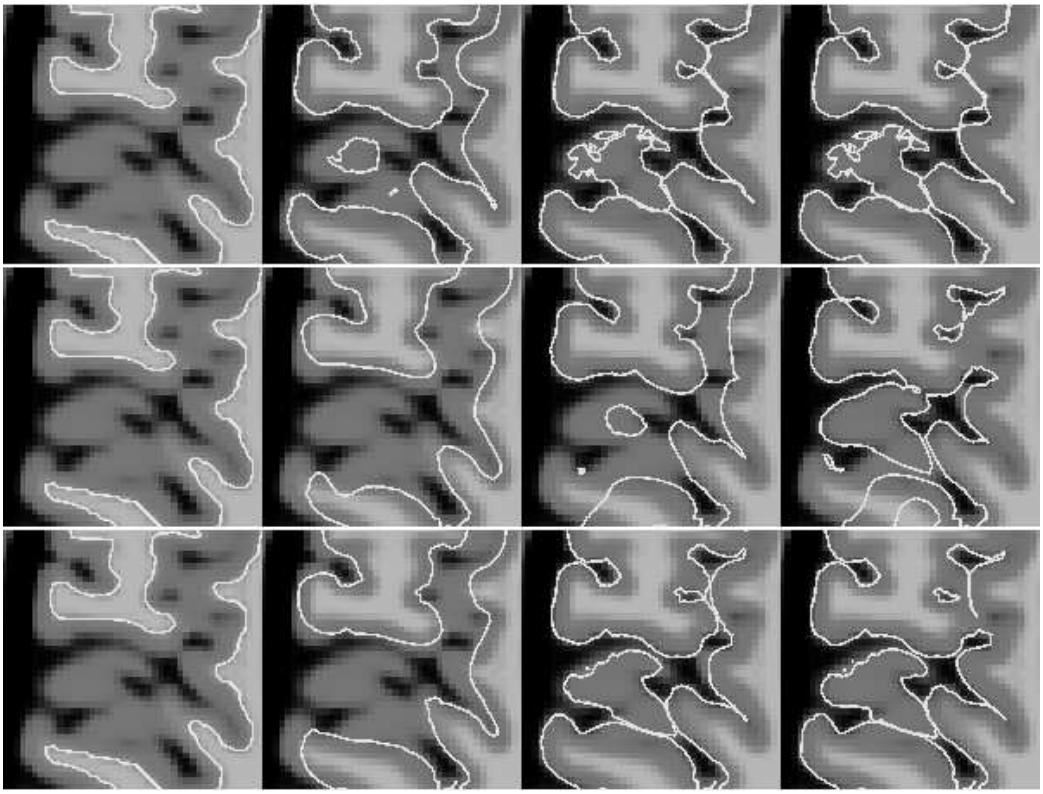

Figure 3.2: Outer surface deformation process using different external forces at different stages in the process. Left to right: Deformation process at iterations 0,5,15 and 30. Top: Only pressure force is enabled. Middle: Only GGVF force is enabled. Bottom: Combination of both forces balanced by the curvature weighting function.

Figure 3.3: Example of a generated cortex from ICBM data. Left: Rendering of outer surface. Right: Inner (black) and outer (white) surfaces superimposed onto MRI.

weighting the forces based on the surface curvature. Preliminary tests were conducted on both simulated data and real data of young normal subjects. The primary results of

these tests indicate that the method is fast, robust and accurate for segmenting the cortical boundary in both simulated and real neuroanatomical data. Still, the method needs further validation, as it must be able to perform on data with varying quality and from a varying population, if it is going to be applicable in everyday clinical use. Future work include a large scale validation on both healthy subjects and subjects with altered cortical morphology.

Acknowledgements

Test data were provided courtesy of the International Consortium of Brain Mapping and McConnell Brain Imaging Centre, Montreal Neurological Institute, McGill University.

References

[1] L. D. Cohen and I. Cohen. Finite-element methods for active contour models and balloons for 2D and 3D images. *IEEE Trans. Pattern Analysis and Machine Intelligence*, 1993.

[2] D. L. Collins, A. P. Zijdenbos, V. Kollokian, J. Sled, N. Kabani, C. Holmes, and A. Evans. Design and construction of a realistic digital brain phantom. *IEEE Transactions on Medical Imaging*, 17(3):463–468, June 1998.

[3] A. M. Dale, B. Fischl, and M. I. Sereno. Cortical surface-based analysis i: Segmentation and surface reconstruction. *NeuroImage*, 9:179–194, 1999.

[4] S. F. Eskildsen, M. Uldahl, and L. R. Østergaard. Extraction of the cerebral cortical boundaries from mri for measurement of cortical thickness. *Progress in Biomedical Optics and Imaging - Proceedings of SPIE*, 5747(2):1400–1410, 2005.

[5] X. Han, D. Pham, D. Tosun, M. Rettmann, C. Xu, and J. Prince. Cruise: Cortical reconstruction using implicit surface evolution. *NeuroImage*, 23(3):997–1012, 2004.

[6] J. S. Kim, V. Singh, J. K. Lee, J. Lerch, Y. Ad-Dab'bagh, D. MacDonald, J. M. Lee, S. I. Kim, and A. C. Evans. Automated 3-d extraction and evaluation of the inner and outer cortical surfaces using a laplacian map and partial volume effect classification. *NeuroImage*, 27(1):210–221, 2005.

[7] D. MacDonald, N. Kabani, D. Avis, and A. C. Evans. Automated 3-D extraction of inner and outer suraces of cerebral cortex from mri. *NeuroImage*, 12:340–356, 2000.

[8] T. McInerney and D. Terzopoulos. Topology adaptive deformable surfaces for medical image volume segmentation. *IEEE Trans. Medical Imaging*, 18(10):840–850, 1999.

[9] D. Pham and J. Prince. Adaptive fuzzy segmentation of magnetic resonance images. *IEEE Transactions on Medical Imaging*, 18(9):737–752, September 1999.

[10] C. Xu, D. L. Pham, M. E. Rettmann, D. N. Yu, and J. L. Prince. Reconstruction of the human cerebral cortex from magnetic resonance images. *IEEE Trans. Medical Imaging*, 18(6):467–480, 1999.

[11] X. Zeng, L. H. Staib, R. T. Schultz, and J. S. Duncan. Segmentation and measurement of the cortex from 3-d mr images using coupled-surfaces propagation. *IEEE Trans. Medical Imaging*, 18(10):100–111, October 1999.

Chapter 4

Quantitative Comparison of Two Cortical Surface Extraction Methods Using MRI Phantoms

Adapted from: Simon F. Eskildsen and Lasse R. Østergaard: Quantitative Comparison of Two Cortical Surface Extraction Methods Using MRI Phantoms, MICCAI 2007, Lecture Notes in Computer Science, 4791, pp. 409-416, October, 2007.

4.1 Introduction

Reconstruction of the human cerebral cortex from magnetic resonance (MR) images facilitates morphometric studies and brain mapping, and provides intuitive visualisation of the human brain for the use in e.g. surgical planning. Since the nineties a number of algorithms has been developed for extracting the boundaries of the cortex from MR images [2, 4, 8, 9, 12, 13, 15]. FreeSurfer has been around for more than seven years, and has, due to the fact that it is freely available, become widespread in the scientific community. We have recently published a method (henceforth designated Fast Accurate Cortex Extraction (FACE)), which resembles FreeSurfer in many aspects, but is significantly improved in terms of computational speed [5, 6].

When performing morphometric studies the accuracy of the cortex reconstructions is very important. Therefore, it is of interest to investigate how well FACE performs in terms of accuracy compared to FreeSurfer. Quantification of the accuracy is difficult as the ground truth is rarely available. A means to measure the accuracy is using phantoms resembling real neuroanatomical data. Lee et al. [11] compared FreeSurfer [4], CLASP [9] and BrainVISA [12] using generated phantoms. They found that CLASP was more accurate than BrainVISA and FreeSurfer. However, CLASP is not publicly available, while the two other methods are. FreeSurfer performed second best in the study. In this study we compare our method, FACE, to FreeSurfer using realistic phantoms generated from real MR scans.

4.2 Methods

To evaluate the two cortex extraction methods, eight healthy young subjects (age: 32 ± 7.4) and eight healthy middle-aged subjects (age: 54.3 ± 6.0) were selected , and a comparison method similar to the method described by Lee et al. was used [11]. For each subject both methods were used to extract the cortical boundaries. The surfaces extracted by each method were used as reference for the generation of simulated MR scans as described

below. The cortex of these customised phantoms were extracted by each method and the resulting surfaces were compared to the reference surfaces (see figure 4.1).

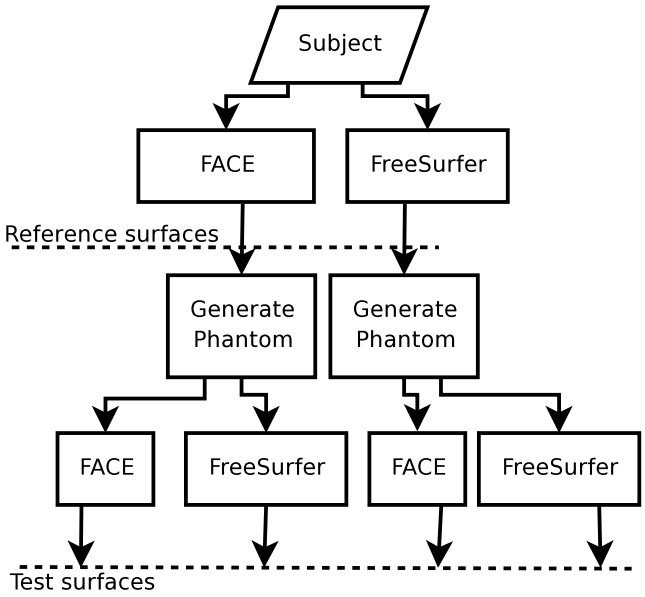

Figure 4.1: Flow chart illustration of the comparison method.

The following briefly describes the two cortex extraction methods, the generation of the test phantoms, and how the error between the reference surfaces and the test surfaces was quantified.

4.2.1 FreeSurfer Method

FreeSurfer [4, 7] first registers the input MR volume to Talairach space [3]. Non-uniformities originating from inhomogeneities in the magnetic field are corrected, and the intensities are normalised. The resulting volume is skull stripped using an approach similar to BET [14]. The WM voxels inside the skull stripped volume is labelled using a two-step segmentation algorithm based on intensities and prior knowledge of the GM/WM interface. The ventricles and subcortical matter inside the WM component is filled, and the WM is separated into the two hemispheres by a sagittal cut through the corpus callosum and an axial cut through the pons. A connected component algorithm is used to isolate the main body of WM voxels, i.e. the cerebrum WM voxels.

From the WM voxels a surface mesh is constructed by generating connected triangles on the faces of the voxels. The resulting surface for each hemisphere is topology corrected to be isomorph to a sphere, and a deformation process smoothes the surface while maintaining it at the WM/GM interface. The pial, or GM surface is found by displacing the WM surface toward the GM/CSF interface using the local surface normals and intensity gradients.

4.2.2 Fast Accurate Cortex Extraction Method

FACE performs similar preprocessing steps as FreeSurfer. The registered, intensity corrected, and skull stripped volume is segmented into WM, GM, and CSF using a fuzzy clustering algorithm solely based on the intensities, and a WM labelling is performed by maximum membership classification. Cerebellum and the brain stem is removed using atlas information, and the hemispheres are separated by a sagittal cut through the corpus callosum. After a connected component analysis spherical topology of each hemisphere

is obtained using a topology correction algorithm [1], and the WM hemispheres can be tessellated by an iso-surface algorithm yielding surfaces with Euler characteristics of a sphere (genus=0).

The iso-surface generated from the WM cerebrum voxels are deformed to fit the WM/GM interface under the influence of smoothing forces and forces derived from the surface normals, the fuzzy voxel classification, and gradient information of the original image.

The GM surface is found using the method described in [6]. The WM surface is displaced towards the GM/CSF interface using a combination of the local surface normals and a gradient vector field calculated from an edge map of the voxel segmentation. The influence of the two vector force fields on each vertex in the surface is weighted by the curvature of the surface, which enables different deformation behaviour according the position on the surface (sulcus or gyrus). The deformation is not minimising an objective function, which means that the complexity is low compared to the deformation process in FreeSurfer.

4.2.3 Phantom Generation

Membership volumes of WM, GM, and CSF were generated directly from the extracted surfaces. This was accomplished by labelling each voxel completely inside the WM surface as WM, and calculating the inside fraction of each voxel intersected by the surface. This was also done for the GM surface, and the memberships for the three tissue classes were calculated from the fuzzy labelled volumes (see figure 4.2). The three membership volumes

Figure 4.2: Fuzzy membership volumes generated from the extracted surfaces. Left to right: WM, GM, and CSF.

were used as input to an MRI simulator [10] with the same acquisition parameters as the original MR scans (TR=18ms, TE=10ms, 1mm slices). The intensities of the resulting volume were normalised to the range of the original scan. Finally, subcortex, ventricles, cerebellum, brain stem, and extra-cerebral tissue were added from the original scan by superimposing the simulated brain scan onto the original (figure 4.3).

4.2.4 Accuracy Assessment

To test the accuracy of each method, reconstructions of the cortical boundaries were generated from the 32 phantoms. The reconstructions were then compared to the reconstructions of the original MR scans. Both methods ensures correct topology by volume- or surface-correction. Thus the comparison was based solely on geometrical factors. Four factors were considered, namely volume difference, surface area difference, over/under seg-

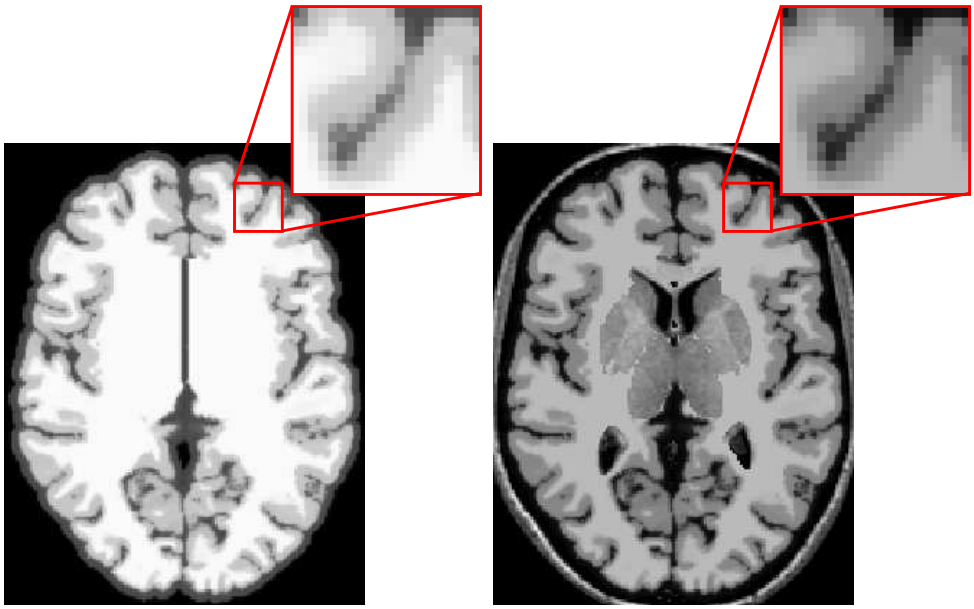

Figure 4.3: Phantom produced by the MRI simulator (left), and final phantom after normalisation and added original tissue (right).

mentation ratio, and the explicit geometrical error. Also the vertex density was taking into consideration in the comparison.

- **Volume Difference:** The enclosing volume of the surfaces was calculated and the difference (in percent) from the reference surfaces was measured.
- **Surface Area Difference:** Surface areas were calculated and the difference (in percent) from the reference surfaces was measured.
- **Over/under segmentation ratio:** Tissue membership volumes of WM, GM and CSF were created from the test surfaces similar to the procedure used in the phantom generation. The resulting fuzzy maps were compared to the maps generated from the reference surfaces, and the percentages of voxels respectively missing inside (false negatives) and added outside (false positives) the reference map were calculated.
- **Explicit Geometrical Error:** The Euclidean distance from each vertex in the reference surface to the closest face on the test surface was measured. The root mean square error of these distances was calculated for both the WM surface and the GM surface. Similarly, the distance was measured from the test surface to the reference surface. The latter was done to avoid that simply adding vertices to the surface did not necessarily reduce the error.

4.3 Results

The cortical extractions were performed on an AMD Opteron 2.6 GHz processor with 12 GB memory. The average extraction time from native scan to final surfaces for FreeSurfer was 20.1 hours, while it was 0.8 hours for FACE. The following presents the results on how well the methods reconstructed the original surfaces from the generated phantoms.

When comparing the reconstructed surfaces visually, only small differences can be discerned. Figure 4.4 shows the original GM surface along with the reconstructions by the two methods. The number of vertices in the surfaces generated by the two methods

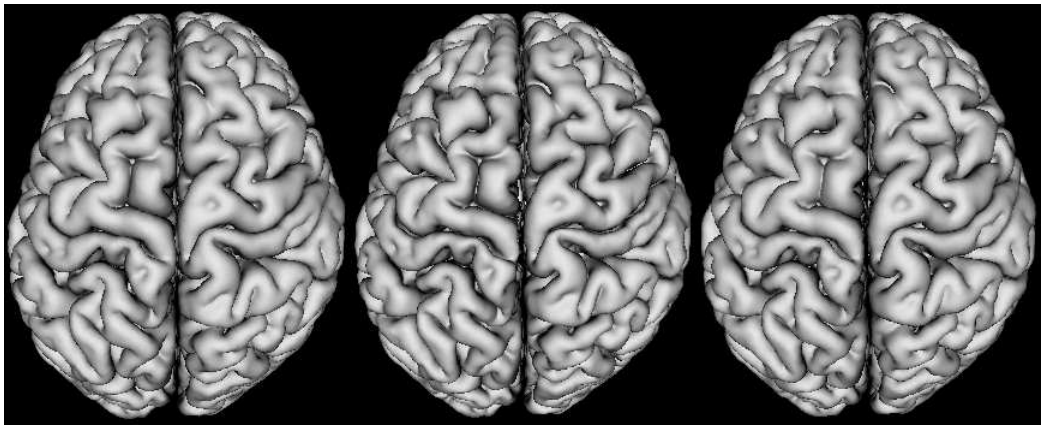

Figure 4.4: Left: Surface extracted from original scan by FACE. Middle: Reconstruction from phantom by FreeSurfer. Right: Reconstruction from phantom by FACE.

	FreeSurfer Phantom			FACE Phantom		
Metric	FreeSurfer	FACE	P-value	FreeSurfer	FACE	P-value
WM Δvol (%)	**1.2±1.1**	5.4±2.6	0.00	**1.7±1.9**	4.9±2.3	0.00
WM Δarea (%)	7.6±1.9	**3.1±1.5**	0.00	15.4±3.4	**9.4±1.9**	0.00
Brain Δvol (%)	4.4±1.2	4.0±1.0	0.36	5.5±2.0	**3.7±0.8**	0.01
GM Δarea (%)	5.4±1.4	5.0±3.1	0.54	2.5±2.4	1.6±1.5	0.22
WM FN (%)	8.5±1.3	**4.2±0.6**	0.00	10.0±2.1	**3.2±0.6**	0.00
WM FP (%)	**7.8±0.8**	9.1±2.3	0.01	8.7±0.8	**7.4±1.8**	0.00
GM FN (%)	23.4±1.3	**21.9±2.0**	0.01	26.4±3.7	**19.9±1.9**	0.00
GM FP (%)	15.7±1.4	**7.3±1.4**	0.00	17.6±3.1	**6.9±1.3**	0.00
WM ref2test (mm)	0.95±0.64	1.14±0.11	0.20	1.47±0.90	**0.63±0.07**	0.00
WM test2ref (mm)	0.75±0.14	0.84±0.17	0.13	1.28±0.17	**0.46±0.05**	0.00
GM ref2test (mm)	0.86±0.50	1.07±0.11	0.08	1.26±0.92	**0.64±0.08**	0.02
GM test2ref (mm)	0.83±0.14	**0.63±0.13**	0.00	1.39±0.19	**0.59±0.06**	0.00

Table 4.1: Errors measured by the four metrics on both WM and GM surfaces. Errors are deviation from the reference surfaces. For each metric the performance on both FreeSurfer and FACE phantoms is compared for the two methods (two-tailed paired t-test). Significant smaller errors are marked by bold font.

vary. FreeSurfer generates surfaces with almost twice the number of vertices compared to FACE (310,415±18,628 vs. 169,218±9,755).

Table 4.1 lists the results for each error metric averaged for the 16 subjects. The errors of the two methods for each metric was compared and tested by two-tailed paired t-test (the p-values are listed in the right hand column of each phantom). Significant smaller errors are marked by bold font. The volume and area errors are absolute percent change compared the to reference surfaces. The under/over segmentation error is measured by percent outside reference surface volume (false positives (FP)) and percent missing inside reference surface (false negatives (FN)). The explicit geometrical difference is measured by the RMS error in mm.

4.4 Discussion

From table 4.1 it can be observed that FACE has significantly fewer WM false negatives and GM false positives when testing on both groups of phantoms. The two metrics are

related in that missing WM voxels most likely are classified as GM voxels. Generally, both methods seem to over-expand the surfaces when compared to the phantoms. This especially increases the GM false negatives percentage, as the GM tissue class is smaller than the WM tissue class.

The geometrical error rates show that the average distance between the test and reference surfaces is at subvoxel level when testing the accuracy of FACE. Reproducibility errors of FACE are consistently around half a voxel size, while FreeSurfer reproducibility errors are between 0.75 - 0.95 voxel size. For purposes of comparison the difference for the reference surfaces of the two methods was measured to 1.48 ± 0.31 mm (average for both WM and GM surfaces).

When looking at the volume and area errors for the GM surfaces, i.e. cerebrum volume and area, there is little difference between the two methods, and the error is fairly small (1.6% - 5.5%). Also, the WM volume errors are low. However, higher error rates are found in the WM area. Looking at the area change per subject, it was found that all reconstructed WM surfaces had a smaller area than the reference, while the volume remained more or less the same. This could point to the fact that the WM voxels in the phantoms do not exactly resemble the original MR WM voxels leading to less deep sulci. Improvements of the phantoms could solve this bias. Also, visual inspection of the surfaces revealed significant differences in the surfaces at the base of the brain due to the different brain stem cutting strategies in the two methods. The inspection also revealed that FreeSurfer in a few surfaces missed part of the occipital lobe. This could be caused by registration errors which again could be caused by tissue voxels not resembling real MR data.

Generally, the tests show that the accuracy of FACE is comparable to Free-Surfer. In most cases FACE has a significantly better accuracy. FACE is on average more than 25 times faster than FreeSurfer. The longer extraction time in FreeSurfer can partly be explained by the high number of vertices in the surfaces. FreeSurfer generates surfaces with almost twice the number of vertices compared to FACE. Another reason for the speed difference is a very fast convergence of the deformation in FACE due to refraining from minimising an objective function.

Even though FACE in the comparison proved to be more accurate, results from some of the error metrics and visual inspections suggested that the phantoms could be improved to resemble real anatomical MR data. However, the results indicate that FACE is comparable to FreeSurfer in terms of accuracy.

The subjects used in this study were healthy without altered cortical morphology. Further studies must examine the accuracy of the two methods when analysing subjects with altered morphology (e.g. Alzheimer's patients), which is often the case in clinical trials.

Acknowledgements

Test data were provided courtesy of Dr. Peter Johannsen, Rigshospitalet, under grant number 22-04-0458 Danish Medical Research Counsil, and the International Consortium of Brain Mapping, McConnell Brain Imaging Centre, Montreal Neurological Institute, McGill University.

References

[1] L. Chen and G. Wagenknecht. Automated topology correction for human brain segmentation. *Lecture Notes in Computer Science*, 4191(LNCS):316–323, 2006.

[2] L. D. Cohen and I. Cohen. Finite-element methods for active contour models and balloons for 2D and 3D images. *IEEE Trans. Pattern Analysis and Machine Intelligence*, 1993.

[3] D. L. Collins, P. Neelin, T. M. Peters, and A. Evans. Automatic 3d intersubject registration of mr volumetric data in standardized talairach space. *Journal of Computer Assisted Tomography*, 18(2):192–205, March-April 1994.

[4] A. M. Dale, B. Fischl, and M. I. Sereno. Cortical surface-based analysis I: Segmentation and surface reconstruction. *NeuroImage*, 9(2):179–194, 1999.

[5] S. F. Eskildsen, M. Uldahl, and L. R. Østergaard. Extraction of the cerebral cortical boundaries from mri for measurement of cortical thickness. *Progress in Biomedical Optics and Imaging - Proceedings of SPIE*, 5747(2):1400–1410, 2005.

[6] S. F. Eskildsen and L. R. Østergaard. Active surface approach for extraction of the human cerebral cortex from mri. *Lecture Notes in Computer Science*, 4191(LNCS):823–830, 2006.

[7] B. Fischl, M. I. Sereno, and A. M. Dale. Cortical surface-based analysis ii: Inflation, flattening, and surface-based coordinate system. *NeuroImage*, 9(2):195–207, 1999.

[8] X. Han, D. Pham, D. Tosun, M. Rettmann, C. Xu, and J. Prince. CRUISE: Cortical reconstruction using implicit surface evolution. *NeuroImage*, 23(3):997–1012, 2004.

[9] J. S. Kim, V. Singh, J. K. Lee, J. Lerch, Y. Ad-Dab'bagh, D. MacDonald, J. M. Lee, S. I. Kim, and A. C. Evans. Automated 3-d extraction and evaluation of the inner and outer cortical surfaces using a laplacian map and partial volume effect classification. *NeuroImage*, 27(1):210–221, 2005.

[10] R.-S. Kwan, A. Evans, and G. Pike. MRI simulation-based evaluation of image-processing and classification methods. *IEEE Transactions on Medical Imaging*, 18(11):1085–97, 1999.

[11] J. Lee, J.-M. Lee, J. S. Kim, I. Y. Kim, A. C. Evans, and S. I. Kim. A novel quantitative cross-validation of different cortical surface reconstruction algorithms using mri phantom. *NeuroImage*, 31:572–584, 2006.

[12] J.-F. Mangin, V. Frouin, I. Bloch, J. Régis, and J. López-Krahe. From 3d magnetic resonance images to structural representations of the cortex topography using topology preserving deformations. *Journal of Mathematical Imaging and Vision*, 5(4):297–318, December 1995.

[13] T. McInerney and D. Terzopoulos. Topology adaptive deformable surfaces for medical image volume segmentation. *IEEE Trans. Medical Imaging*, 18(10):840–850, 1999.

[14] S. M. Smith. Fast robust automated brain extraction. *Human Brain Mapping*, 17(3):143–155, 2002.

[15] X. Zeng, L. H. Staib, R. T. Schultz, and J. S. Duncan. Segmentation and measurement of the cortex from 3-d mr images using coupled-surfaces propagation. *IEEE Trans. Medical Imaging*, 18(10):100–111, October 1999.

Chapter 5

Evaluation of Five Algorithms for Mapping Brain Cortical Surfaces

Adapted from: S. F. Eskildsen and L. R. Østergaard: Evaluation of Five Algorithms for Mapping Brain Cortical Surfaces, SIBGRAPI, pp. 137-144, 2008 XXI Brazilian Symposium on Computer Graphics and Image Processing, 2008

5.1 Introduction

Morphological analysis of the human cerebral cortex from in-vivo medical images plays an important role in the investigation of various neurological disorders, such as schizophrenia and dementia [6, 18]. Increasing effort is being put into measuring cortical morphological changes over time and differences between populations. Magnetic resonance imaging (MRI) provides excellent structural information of the cerebral tissues, and surface reconstructions of the cortex from MRI have grown popular for studying morphological features, such as cortical thickness, area, and patterns of the cortical folds. During the last decade several surface reconstruction algorithms have been proposed [7,9,14,17,21,34], and several ways to obtain cortical thickness measurements and other features from cortical surfaces have been developed [24, 28]. Usually the cortical surfaces are approximated by discrete polygonal meshes, and cortical features are calculated at each vertex provided a reasonably uniform distribution of vertices across the surface. To measure morphological differences between subjects one can average the measurements over the entire cortex or within specified regions, but to exploit the detailed map of measurements provided by high resolution surfaces and be able to detect focal differences a point correspondence between cortical surfaces is required. Such a mapping must preserve anatomical landmarks across subjects in order to reliably compare measurements, i.e. it does not make sense to compare the top of a fold (gyrus) on one surface with the bottom of a fold (sulcus) on another surface. Because of the high diversity of folding patterns across individual cortices, such a mapping is far from trivial.

5.2 Background

Several methods to solve the cortical mapping problem have been proposed. A popular approach is to parameterize the cortical surface by mapping the surface into a canonical space and solve the correspondence problem in this space. Often the unit sphere is used, as it is topologically equivalent to the cortical surface and provides an attractive coordinate system for easy parameterization [13]. Utilizing the Riemann mapping theorem on manifold surfaces [1] several approaches have been proposed to conformally map the cortical surface to a sphere [16, 19, 23, 25, 26, 31]. Also other canonical spaces have been

used for parameterization, such as an ellipsoid and the 2D plane [33]. The latter, so-called flat maps, require cuts in the closed surface to be able to map the surface to the plane. Consistent cuts are hard to automate, thus requiring manual intervention.

After parameterization of cortical surfaces the correspondence between vertices can be obtained by registration of the surfaces in the canonical space using the preserved geometrical features as similarity measure. This registration is usually a non-linear warp because of the highly irregular folding patterns [12, 35].

The mapping onto a canonical space introduces geometrical distortion in the surface, and even though work has been focused on minimizing the distortion in the conformal mapping [23] it remains a problem for the subsequent parameterization and registration. Creating flat maps introduces more geometrical distortion than the spherical approach and alters the topology thus partly destroying geodesic relations between vertices [12]. Several methods constrain the mapping using landmark curves [16, 25, 29, 33]. These are often manually defined, but methods have been proposed to automate identification of landmark curves [15, 22, 28], though it is hard to do consistently [4].

Another group of methods try to solve the correspondence problem without the intermediate step of mapping to a canonical space. One family of such methods is derived from the iterative closest point method (ICP) [2,5]. Apart from variations over the simple closest point method, several methods combine ICP with point feature registration [10,27]. Others approach the problem by finding a direct mapping using partial differential equations (PDE) [29] or diffeomorphisms [32].

Common for the mapping approaches described above is the preservation of intrinsic vertex configuration, except from the cuts introduced when creating flat maps. This may seem important, as these geometric properties reflect the underlying cytoarchitecture of the cortex. However, when mapping between cortices with very different cortical folding patterns, this constraint can be relaxed to better match morphological features. A feature based method disregarding the intrinsic vertex configurations was proposed by Spjuth et al. [30]. They used a similarity functional based on mean curvature, surface normals, and Euclidean distance to find corresponding vertices between surfaces after an initial, global, affine registration. The method allows several vertices to map to the same target vertex while other vertices are left without mapping. Thereby information is lost. To retain information, the optimal solution is a bijection between the surfaces only mapping between similar anatomical points. When a vertex to vertex correspondence is needed the mapping cannot be a bijection if the two cortex surfaces have different number of vertices. However, one can try to approximate a bijection by having unique projections for as many vertices as possible.

As described above a variety of algorithms for solving the cortical mapping problem have been proposed. However, to the best of our knowledge, comparisons of the different approaches have not been carried out. In this paper we propose a new algorithm for the problem of finding vertex correspondence between surfaces with different vertex counts and evaluate the performance of the proposed algorithm along with a selection of other mapping algorithms.

5.3 Proposed Mapping Algorithm

The proposed algorithm for mapping a source surface to a target surface is inspired by Spjuth et al. [30], and it uses the same similarity features, but seeks to optimize the number of unique mappings, thereby approximating a bijection as close as possible. The algorithm initially aligns the two surfaces with a rigid transformation found by center of mass normalization followed by ICP optimization [5]. The method for finding a vertex to vertex correspondence from source to target surface uses a cost functional J. The cost of mapping between source vertex i and target vertex j is given by

$$J(i,j) = \alpha e^{c(i,j)} + \beta e^{n(i,j)} + \gamma e^{d(i,j)} \tag{5.1}$$

where c is the absolute difference in normalized mean curvature at the vertices, n is the normalized angle between the vertex normals, d is the normalized Euclidean distance between the vertices, and α, β and γ are weights. This cost functional is sought minimized per source vertex by the following algorithm:

Definitions:
V_s is the set of source vertices.
V_t is the set of target vertices.
t_c is the cost threshold any mapping must be below.
t_m is the maximum number of mappings allowed to the same target vertex.
N_s is the set of source vertices without a mapping.
N_t is the set of target vertices with number of mappings $< t_m$.
Initial conditions: $N_s = V_s$, $N_t = V_t$, and $t_m = 1$.

1. For each vertex in N_s find the vertex in N_t with the lowest mapping cost defined by J.
2. For each vertex in V_t where number of mappings $> t_m$ remove highest cost mappings until number of mappings $= t_m$. Update N_s and N_t.
3. Repeat from 1 until no mappings are found with a cost $< t_c$, or either N_s or N_t is empty.
4. If N_s is non-empty, set $N_t = V_t$, $t_m = t_m + 1$ and repeat from 1.

We designate the algorithm iterative closest feature (ICF), because of its use of point features and iterative behavior. The weights in the cost functional were found by repeated trials of mapping between two simple phantom surfaces where the true mapping was known. The found weights were $\alpha = 3.7$, $\beta = 1.1$, and $\gamma = 2.7$.

5.4 Algorithms Selected for Comparison

Apart from the proposed mapping algorithm we wanted to evaluate a handful of typical algorithms to find their strengths and weaknesses. The following algorithms were included in the evaluation:

- Iterative closest point (**ICP**). The basic ICP algorithm [5] to compare with a simple and "naive" approach.
- **Feature**. The method by Spjuth et al. [30] was included as this method is similar to the proposed algorithm but without the iterative behavior.
- Iterative closest feature (**ICF**). The proposed method as described in section 5.3.
- Spherical **Warp**. This is the method used in FreeSurfer to register a cortical surface to a "canonical" surface [12, 13]. Source and target surfaces are mapped to the unit sphere (figure 5.1) and the folding patterns are aligned using a warp minimizing the mean squared difference between the average convexity [13]. This method is included as the algorithm is freely available and the spherical mapping introduces less metric distortion than other mapping methods [20]. To obtain a vertex correspondence map, the geodesic closest points are used between two surfaces registered to the canonical surface provided by FreeSurfer.
- **Spherical**. A method where source and target surfaces are mapped to a sphere and corresponding points are found by rotations of the source surface optimizing curvature correlation. The method is similar to the approach described by Fischl et al. [12], but instead of the final non-linear warp a rigid optimization is performed iteratively in a multi-scale manner. The spherical mapping was done using FreeSurfer

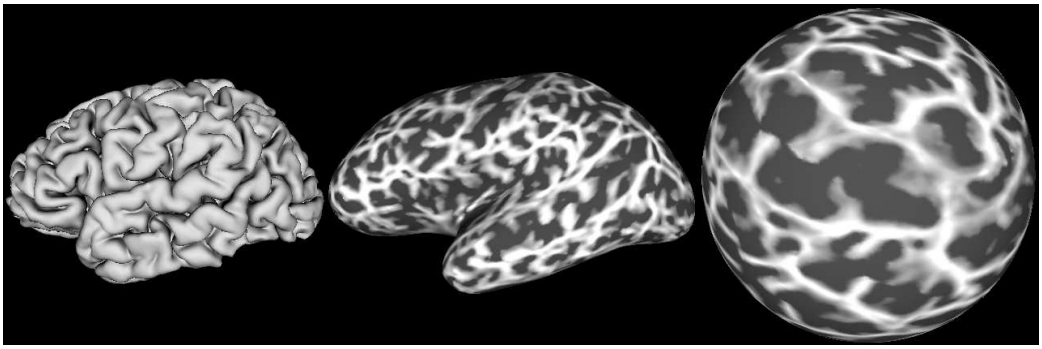

Figure 5.1: From cortex surface to sphere. Left: Original cortical surface. Middle: Inflated surface with curvature values superimposed. Right: Surface mapped to a sphere with curvature values superimposed.

[7], while the subsequent optimization was implemented locally. As in the warp approach described above, a vertex correspondence map is obtained by the geodesic closest points between the two surfaces after optimization.

The following section describes how the five mapping algorithms were evaluated.

5.5 Mapping Evaluation

Performance of the algorithms was tested using 10 cortical surfaces extracted by the FreeSurfer software [7] from T1 weighted MRI scans (1.5 Tesla, 30°flip angle, TR/TE=18/10 ms, isotropic 1 mm voxels) from young healthy subjects. FreeSurfer produces surfaces of the inner and outer boundary of the cortex for each hemisphere separately. Surfaces of the outer cortical boundary of left hemispheres only were used in the evaluation, as brain symmetri properties suggest that either hemisphere is representative for the cortical variation, and the mapping algorithms are expected to perform equally well on both hemispheric surfaces. Surfaces generated by FreeSurfer are triangular meshes with spherical topology and have arbitrary number of vertices, thus they are well-suited for testing the algorithms described here. The 10 extracted left cortical surfaces had on average 148k±8k vertices. The distribution of vertices were assumed similar for the generated surfaces. All 10 cortical surfaces were in turn used as target for mapping the other nine surfaces, thus resulting in 90 mappings in total used in the evaluation.

The optimal corresponding target vertex for any given source vertex can be sought even though this means that two distinct vertices may map to the same vertex on the target surface. It is desirable to map to as many vertices on the target surface as possible to retain information, i.e. the image of the mapping must cover as much of the target surface as possible. The higher coverage of the target surface the better approximation of a bijection between the surfaces. Therefore, one criterion for a good mapping is the percentage of vertices on the target surface that are used as correspondence points for vertices on the source surface, i.e. the coverage of the target surface. If the source surface has less vertices than the target surface full coverage is not possible. Therefore the coverage error, C, is defined as:

$$C = 1 - \frac{|M_t|}{min(|V_s|, |V_t|)}, \tag{5.2}$$

where M_t is the set of target vertices with a mapping, and V_s and V_t are the same as in section 5.3. Thus a full coverage results in $C = 0$ while mappings with less coverage have higher values with a theoretical upper limit of $C = 1$.

Increasing the vertex count of the source surface provides better conditions for a good coverage. However, a source surface with twice as many vertices as the target surface may

provide full coverage of the target surface without being considered a good mapping if for instance a large portion of source vertices map to the same target vertex. Therefore, another criterion for a good mapping is the mean square number of mappings per target vertex normalized by the squared source/target vertex count ratio. The multiple mapping error, M, is defined as:

$$M = \frac{\frac{1}{|V_t|}\sum_{j \in V_t} m_j^2}{(\frac{|V_s|}{|V_t|})^2} - 1 = \frac{|V_t|\sum_{j \in V_t} m_j^2}{|V_s|^2} - 1 \tag{5.3}$$

where m_j is the number of mappings to vertex j of the target surface. If $M = 0$ the mapping is optimal with regard to the criterion, while higher values of M signal worse mappings with a theoretical upper limit of $M = |V_t| - 1$.

When mapping between surfaces we expect that patches of the source surface are mapped to patches of similar size on the target surface. We introduce a third criterion aiming at evaluating this property. For each vertex i on the source surface we determine the geodesic distances to the neighbors along the target surface after applying the map, where the geodesic distance is calculated as the minimum edge length between vertices (Dijkstra's algorithm [8]). Optimally, this distance should be the same as on the source surface when surfaces have equally distributed vertices. We calculate the geodesic error at vertex i as:

$$\phi(i) = \frac{1}{|N(i)|}\sum_{j \in N(i)} |g(m(i), m(j)) - g(i, j)| \tag{5.4}$$

where $N(i)$ is the set of neighboring vertices to vertex i on the source surface, $g(i, j)$ is the geodesic distance between i and neighbor j, while $g(m(i), m(j))$ the geodesic distance between these vertices after the mapping. The density evaluation criteria, D, is defined as the average of the geodesic errors:

$$D = \frac{1}{|V_s|}\sum_{i \in V_s} \phi(i) \tag{5.5}$$

A mapping with good preservation of source surface patches has a small D with a theoretical minimum of $D = 0$ for the perfect preservation. This metric is affected if the vertex distributions of the two surfaces are highly irregular. For this reason, similar distributions of the surfaces are assumed.

Finally, we wanted to evaluate if vertices are mapped between similar topographical areas. To quantify this we define a topography criterion, T, as the average difference in mean curvature before and after mapping to the target surface:

$$T = \frac{1}{|V_s|}\sum_{i \in V_s} |\rho(i) - \rho(m(i))| \tag{5.6}$$

where $\rho(i)$ is the mean curvature at vertex i and $m(i)$ is the mapping of vertex i (the target vertex). Curvature values are normalized to the interval $[-1 : 1]$, thus the topography criterion has values in $[0 : 2]$ with theoretical extrema.

The four criteria described above are all quantitative approaches to evaluating the mapping between cortical surfaces. To add a more qualitative approach we performed a landmark test to evaluate the algorithms' performance in mapping to the same anatomical landmarks between different cortical surfaces. Six landmarks were identified manually on all 10 cortical surfaces of the left hemisphere. Landmarks were placed by labeling vertices spanning areas of 1-5 mm^2. The selected anatomical landmarks were the temporal pole (TP) at the anterior end of the superior temporal gyrus, the supramarginal gyrus (SG) at the posterior end of the lateral sulcus, the cuneus (Cun) where the parieto-occipital sulcus meets the calcarine sulcus, the posterior part of gyrus rectus (GR), the most superior

	Avg. difference (mm)	Paired t-test (p-val)
ICP	-0.10±0.05	<0.01
Feature	0.02±0.03	0.11
ICF	-0.01±0.02	0.06
Spherical	0.00±0.03	0.64
Warp	0.01±0.01	0.13

Table 5.1: Average difference in mean cortical thickness after mapping.

part of the post central gyrus (PCG), and the cingulate gyrus (CG) at the anterior end of the cingulate sulcus. These anatomical locations were used as they are relatively easy to recognize on the cortical surface, but are still subject of morphological variation. For each mapping the geodesic distances between the mapped landmarks and the manually labeled landmarks were measured and averages over all 90 mappings were calculated.

Finally, we wanted to evaluate the effect of different mapping algorithms on statistical maps, which are often used when measuring cortical thickness. We wanted to test if choice of mapping algorithm would change the conclusions drawn from cortical thickness statistics. The cortical thicknesses of the 10 subjects were therefore mapped to a random target surface and the non-parametric Kruskal-Wallis test [3] was performed at each vertex to test for equality among the mapped values. Furthermore, at each vertex the algorithms were tested against each other using the non-parametric Mann-Whitney-Wilcoxon (MWW) test [3] to evaluate differences between them.

5.6 Results

The four quantitative evaluation criteria as defined in section 5.5 were calculated for all 90 mappings. Figure 5.2 shows the average errors calculated for each algorithm by the evaluation criteria. The results from the landmark test are shown in figure 5.3. Table 5.1

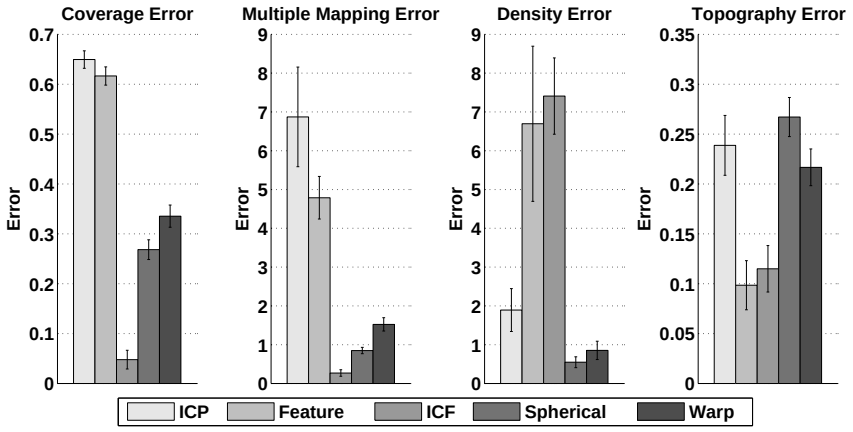

Figure 5.2: Average errors of mapping with the five tested algorithms between permutations of the 10 cortical surfaces (n=90).

shows the average difference in mean cortical thickness before and after mapping the nine cortices to the randomly selected reference surface. The Kruskal-Wallis test showed that 31% of the vertices were dependent on the mapping algorithm, and the subsequent MWW test revealed that the feature and ICF algorithms were providing similar statistical results, while specifically the spherical rigid approach had areas with conclusions different from the other algorithms (table 5.2). Figure 5.4 shows the statistical maps when comparing the ICF algorithm with each of the other four mapping algorithms using the MWW test.

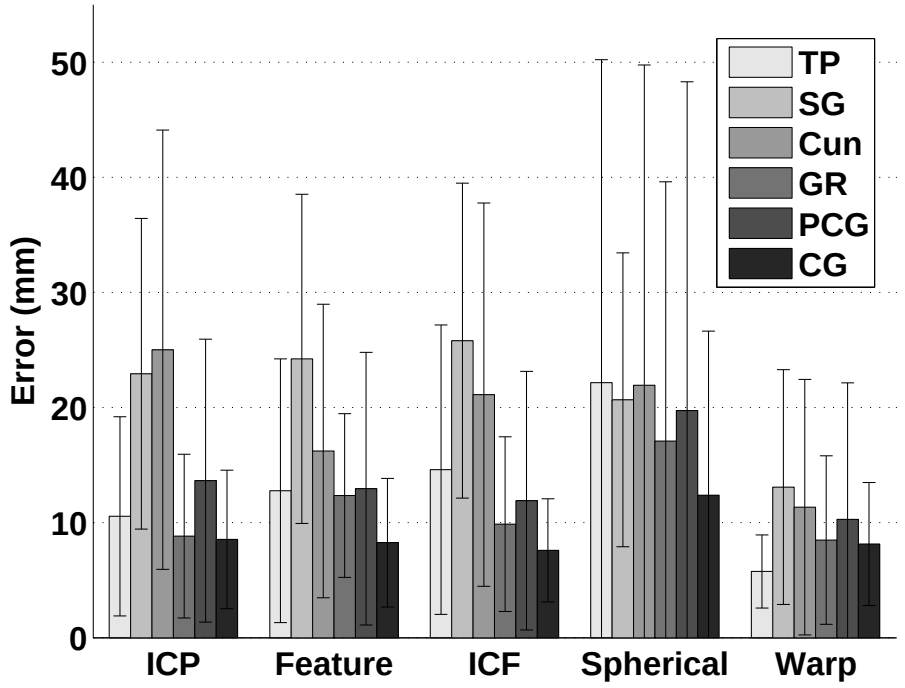

Figure 5.3: Average distances in mm from mapped landmark to manually labeled landmark of 90 mappings. Landmarks are temporal pole (TP), supramarginal gyrus (SG), cuneus (Cun), gyrus rectus (GR), post central gyrus (PCG), and anterior cingulate gyrus (CG).

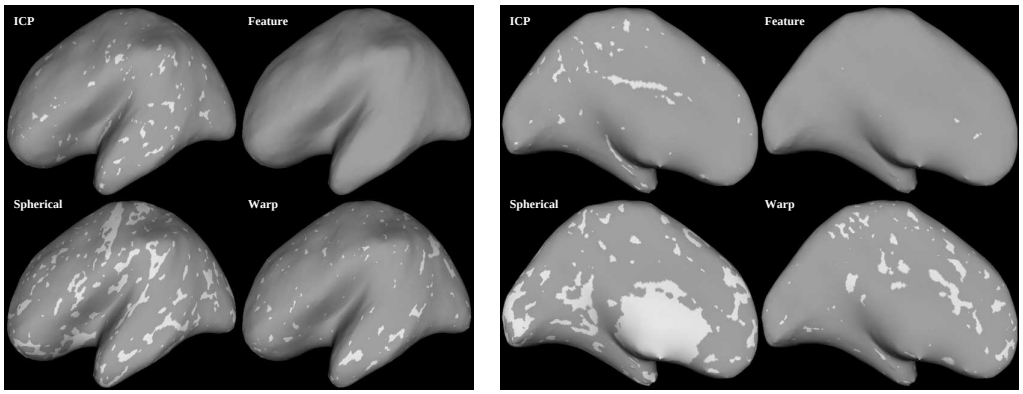

(a) Lateral views (b) Medial views

Figure 5.4: ICF compared vertex by vertex to the other four mapping algorithms visualized on an inflated reference surface. White areas indicate significant difference ($p<0.05$) in the cortical thicknesses mapped to a vertex.

5.7 Discussion

Evaluation Metrics

The four evaluation criteria in section 5.5 were designed to evaluate the behavior of the examined mapping algorithms. Even though the criteria should optimally result in as low

	Feature	ICF	Spherical	Warp
ICP	6%	3%	24%	14%
Feature	-	0%	22%	6%
ICF	-	-	22%	6%
Spherical	-	-	-	22%

Table 5.2: Percent vertices of reference surface where the MWW test rejects the hypothesis that the cortical thicknesses come from the same population ($\alpha = 0.05$) for the different mapping algorithms, which means that the mappings influence the conclusion.

values as possible, all criteria cannot be expected to be low because of the highly diverse folding patterns in the surfaces. For example, a low density error, i.e. a good preservation of the intrinsic vertex configurations, will inevitably result in a high topography error, as some vertices are mapped from convexities to concavities and vice versa. Nevertheless, the four criteria are useful for evaluating the algorithms' strengths and weaknesses.

From figure 5.2 it can be seen that the algorithms behave more or less as expected. The ICP algorithm not surprisingly has relatively high coverage, multiple mapping, and topography errors, while the density error is kept low. This is to be expected as no constraints on multiple mappings or topography preservation are applied, and vertices are kept very compact as only the Euclidean distance is optimized. The feature algorithm as proposed by Spjuth et al. [30] has almost as bad a coverage as the ICP algorithm, but performs better in both the multiple mapping and topography criteria. As expected the density error for the feature algorithm is high, as neighboring vertices are allowed to jump between gyri resulting in long geodesic distances between the mapped vertices. The proposed ICF algorithm behaves approximately similar to the feature algorithm with regard to the density and topography criteria. However, when evaluating the coverage and multiple mapping, it can be seen that this algorithm has the lowest errors among the five evaluated algorithms. This was expected as constraints are enforced to prevent multiple mappings and optimize the coverage.

The two mapping approaches that use an intermediate step in form of mapping to a sphere have a similar behavior. As expected these algorithms have the lowest density errors among the algorithms, and the multiple mapping errors are also relatively low. This is because the intrinsic vertex configurations are retained during the spherical fitting process. However, the coverage errors are relatively high, and the topography errors are highest among the evaluated algorithms for the rigid spherical approach, while a little lower for the warp approach. This is interesting as the fitting process should minimize the topographical differences between the surfaces. This is a tangible sign of the high diversity of the folding patterns, and that maintaining the intrinsic vertex configurations result in mapping between different topographies. The spherical warp approach which non-linearly should compensate for the highly diverse folding patterns still has high topography errors. This may be explained by the fact that the non-linear fitting is done to an average model instead of the actual target surface. It seems that a combination of the ICF and the spherical approach may provide a nice trade-off between the four mapping criteria.

Landmark Test

Figure 5.3 reveals that the mapping algorithms are far from perfect when evaluating how well they map between manually labeled landmarks. The error is measured as the geodesic distance to the manually labeled landmark, which means that mapping to a gyrus or sulcus adjacent to the correct results in a large error. From the figure it can be seen that some landmarks are generally more accurately mapped than others no matter the choice of algorithm. The cingulate gyrus are in most cases mapped with a precision of less than 1 cm, and gyrus rectus is also in most cases mapped more accurately than the remaining four landmarks. These two landmarks are both located medially close to the midbrain

where cortical variations are less pronounced. The supramarginal gyrus, which is located in an area of deep sulci and great cortical variability, generally has high errors in all five algorithms. This emphasize the fact that highly convoluted and variable areas are harder to map than less folded areas. The ICP, feature, and ICF algorithms all have similar patterns of landmark errors not significantly ($0.21<p<0.40$) different from each other, which may be due to the similar nature of these algorithms. The spherical approach with the rigid optimization seems to have a more uniform distribution of errors, except for the cingulate gyrus. This can be explained by the rigid optimization. The spherical approach with the non-linear optimization is able to compensate for the high cortical variability, and it results in errors similar to landmarks in areas without great cortical variability, such as the cingulate gyrus and gyrus rectus. Because of the high standard deviations in the landmark errors, it is hard to confidently determine the best mapping algorithm, however, when averaging all landmark errors within each algorithm the spherical warp approach performs significantly ($p<0.001$) better than the other algorithms with an average error of 9.5 ± 9.0 mm, while the spherical rigid approach performs significantly ($p<0.001$) worse with an average error of 19.0 ± 23.4 mm. Further tests should include more subjects and landmarks in concave regions in addition to the convexly located landmarks used here to get a more representative quantification of mapping accuracy.

Statistical Maps

The averaged cortical thickness after mapping to the random reference surface did not change significantly except when using the ICP algorithm (see table 5.1). However, the generated statistical maps revealed that almost one third of the vertices on the reference surface are dependent on which mapping algorithm is used to map the cortical thickness to the reference. Testing each algorithm against the others revealed that the spherical rigid approach is the algorithm with the largest areas (22% - 24%) of deviating conclusions based on the MWW test (see figure 5.4 and table 5.2). Almost no difference is seen between the ICF and feature algorithms while smaller differences is seen between ICF and ICP (3%) and ICF and the spherical warp (6%). As it can be seen from figure 5.4, 3% is a noticeable portion of a cortex, and may lead to wrong conclusions. This suggests that the impact of the mapping algorithm on the statistical maps is high, and it must be taken into consideration when drawing conclusions from the statistical maps.

Proposed Algorithm

The ICF algorithm extends the simple feature based approach by iteratively approximating a bijection. This is reflected in the quantitative measures of coverage and multiple mapping, where ICF has the lowest errors. However, the algorithm is not more accurate when measuring the distance to the manually placed landmarks, and the statistical maps show no difference between the simple feature based method and the ICF. Though preserving more information, the ICF algorithm does not seem to improve accuracy or change the produced statistical maps.

Both approaches use mean curvature, normal direction, and Eucledian distance for matching vertices. These features do not distinguish between large convex areas, such as the sylvian fissure, and the smaller convexities, such as most of the sulci. Additional features could be included in the cost functional to better map areas of similar sized convexity, e.g. the average convexity as used by FreeSurfer could be used [11, 12]. Also, a term punishing large geodesic distances between vertex neighbors after mapping could be included to compensate for the high density errors. Furthermore, the weights in the cost functional were optimized by a simple phantom surface, and better accuracy may be achieved by optimizing using realistic cortical surfaces.

5.8 Conclusion

This paper presented a new algorithm for solving the cortical mapping problem and tested it along with four other algorithms. The tests of the five mapping algorithms leave a mixed result, where no algorithm can be singled out as the best. The four evaluation criteria showed that the algorithms generally behave expectedly, while the landmark test indicated that the spherical warp approach is more accurate than the rest of the tested algorithms. Choice of algorithm should depend on the study. Dependent on whether the preservation of intrinsic vertex configuration or the comparison of similar topographic areas is important, either the spherical warp or the ICF algorithm should be chosen, as these are respectively more accurate and preserve the most information. A combination of these algorithms could be a promising mapping method and should be investigated in the future. We showed that choice of mapping algorithm impacts the results drawn from statistical maps. However, considering the small number of subjects used here further testing should be carried out to confirm this. Finally, the number of different types of mapping algorithms tested is limited. Other types of mapping methods, such as methods based on diffeomorphic mapping, should also be compared in a future evaluation.

References

[1] L. Ahlfors. *Complex Analysis.* McGraw-Hill Science/Engineering/Math, 3rd edition, 1979.

[2] A. Almhdie, C. Léger, M. Deriche, and R. Lédée. 3d registration using a new implementation of the icp algorithm based on a comprehensive lookup matrix: Application to medical imaging. *Pattern Recognition Letters*, 28(12):1523–1533, 2007.

[3] D. R. Anderson, D. J. Sweeney, and T. A. Williams. *Statistics for business and economics.* South-Western College Publ., 8th edition, 2002.

[4] M. A. Audette, F. P. Ferrie, and T. M. Peters. An algorithmic overview of surface registration techniques for medical imaging. *Medical Image Analysis*, 4(3):201–217, 2000.

[5] P. J. Besl and N. D. McKay. A method for registration of 3-d shapes. *IEEE Transactions on Pattern Analysis and Machine Intelligence*, 14(2):239–256, 1992.

[6] G. Chetelat and J. . Baron. Early diagnosis of alzheimer's disease: Contribution of structural neuroimaging. *NeuroImage*, 18(2):525–541, 2003.

[7] A. M. Dale, B. Fischl, and M. I. Sereno. Cortical surface-based analysis: I. segmentation and surface reconstruction. *NeuroImage*, 9(2):179–194, 1999.

[8] E. W. Dijkstra. A note on two problems in connexion with graphs. *Numerische Mathematik*, 1:269–271, 1959.

[9] S. F. Eskildsen and L. R. Østergaard. Active surface approach for extraction of the human cerebral cortex from mri. *Lecture notes in Computer Science*, 4191 LNCS - II:823–830, 2006.

[10] J. Feldmar and N. Ayache. Rigid, affine and locally affine registration of free-form surfaces. *International Journal of Computer Vision*, 18(2):99–119, 1996.

[11] B. Fischl and A. M. Dale. Measuring the thickness of the human cerebral cortex from magnetic resonance images. *Proceedings of the National Academy of Sciences of the United States of America*, 97(20):11050–11055, 2000.

[12] B. Fischl, M. I. Sereno, and A. M. Dale. Cortical surface-based analysis: II. Inflation, flattening, and a surface-based coordinate system. *NeuroImage*, 9(2):195–207, 1999.

[13] B. Fischl, M. I. Sereno, R. B. H. Tootell, and A. M. Dale. High-resolution intersubject averaging and a coordinate system for the cortical surface. *Human Brain Mapping*, 8(4):272–284, 1999.

[14] R. Goldenberg, R. Kimmel, E. Rivlin, and M. Rudzky. Cortex segmentation: A fast variational geometric approach. *IEEE Transactions on Medical Imaging*, 21(12):1544–1551, 2002.

[15] G. L. Goualher, E. Procyk, D. Louis Collins, R. Venugopal, C. Barillot, and A. C. Evans. Automated extraction and variability analysis of sulcal neuroanatomy. *IEEE Transactions on Medical Imaging*, 18(3):206–217, 1999.

[16] X. Gu, Y. Wang, T. F. Chan, P. M. Thompson, and S. . Yau. Genus zero surface conformal mapping and its application to brain surface mapping. *IEEE Transactions on Medical Imaging*, 23(8):949–958, 2004.

[17] X. Han, D. L. Pham, D. Tosun, M. E. Rettmann, C. Xu, and J. L. Prince. Cruise: Cortical reconstruction using implicit surface evolution. *NeuroImage*, 23(3):997–1012, 2004.

[18] P. J. Harrison. The neuropathology of schizophrenia. a critical review of the data and their interpretation. *Brain*, 122(4):593–624, 1999.

[19] M. K. Hurdal and K. Stephenson. Cortical cartography using the discrete conformal approach of circle packings. *NeuroImage*, 23(SUPPL. 1), 2004.

[20] L. Ju, M. K. Hurdal, J. Stern, K. Rehm, K. Schaper, and D. Rottenberg. Quantitative evaluation of three cortical surface flattening methods. *NeuroImage*, 28(4):869–880, 2005.

[21] S. K. June, V. Singh, K. L. Jun, J. Lerch, Y. Ad-Dab'bagh, D. MacDonald, M. L. Jong, S. I. Kim, and A. C. Evans. Automated 3-d extraction and evaluation of the inner and outer cortical surfaces using a laplacian map and partial volume effect classification. *NeuroImage*, 27(1):210–221, 2005.

[22] C. . Kao, M. Hofer, G. Sapiro, J. Stern, K. Rehm, and D. A. Rottenberg. A geometric method for automatic extraction of sulcal fundi. *IEEE Transactions on Medical Imaging*, 26(4):530–540, 2007.

[23] F. Kruggel. Robust parametrization of brain surface meshes. *Medical Image Analysis*, 12(3):291–299, 2008.

[24] J. P. Lerch and A. C. Evans. Cortical thickness analysis examined through power analysis and a population simulation. *NeuroImage*, 24(1):163–173, 2005.

[25] L. M. Lui, Y. Wang, T. F. Chan, and P. Thompson. Landmark constrained genus zero surface conformal mapping and its application to brain mapping research. *Applied Numerical Mathematics*, 57(5-7 SPEC. ISS.):847–858, 2007.

[26] J. Nie, T. Liu, G. Li, G. Young, A. Tarokh, L. Guo, and S. T. C. Wong. Least-square conformal brain mapping with spring energy. *Computerized Medical Imaging and Graphics*, 31(8):656–664, 2007.

[27] A. Rangarajan, H. Chui, E. Mjolsness, S. Pappu, L. Davachi, P. Goldman-Rakic, and J. Duncan. A robust point-matching algorithm for autoradiograph alignment. *Medical Image Analysis*, 1(4):379–398, 1997. Cited By (since 1996): 45.

[28] M. E. Rettmann, X. Han, C. Xu, and J. L. Prince. Automated sulcal segmentation using watersheds on the cortical surface. *NeuroImage*, 15(2):329–344, 2002.

[29] Y. Shi, P. M. Thompson, I. Dinov, S. Osher, and A. W. Toga. Direct cortical mapping via solving partial differential equations on implicit surfaces. *Medical Image Analysis*, 11(3):207–223, 2007.

[30] M. Spjuth, F. Gravesen, S. F. Eskildsen, and L. R. Østergaard. Early detection of ad using cortical thickness measurements. *Progress in Biomedical Optics and Imaging - Proceedings of SPIE*, 6512, 2007.

[31] D. Tosun, M. E. Rettmann, and J. L. Prince. Mapping techniques for aligning sulci across multiple brains. *Medical Image Analysis*, 8(3):295–309, 2004.

[32] M. Vaillant, A. Qiu, J. Glaunès, and M. I. Miller. Diffeomorphic metric surface mapping in subregion of the superior temporal gyrus. *NeuroImage*, 34(3):1149–1159, 2007.

[33] D. C. Van Essen, H. A. Drury, S. Joshi, and M. I. Miller. Functional and structural mapping of human cerebral cortex: Solutions are in the surfaces. *Proceedings of the National Academy of Sciences of the United States of America*, 95(3):788–795, 1998.

[34] H. Xue, L. Srinivasan, S. Jiang, M. Rutherford, A. D. Edwards, D. Rueckert, and J. V. Hajnal. Automatic segmentation and reconstruction of the cortex from neonatal mri. *NeuroImage*, 38(3):461–477, 2007.

[35] G. Zou, J. Hua, and O. Muzik. *Non-rigid surface registration using spherical thin-plate splines*, volume 4791 LNCS. 2007.

Chapter 6

Cortical Volumes and Atrophy Rates in FTD-3 *CHMP2B* Mutation Carriers and Related Non-carriers

Adapted from: Simon F. Eskildsen, Lasse R. Østergaard, Anders B. Rodell, Leif Østergaard, Jørgen E. Nielsen, Adrian M. Isaacs, and Peter Johannsen: Cortical Volumes and Atrophy Rates in FTD-3 CHMP2B Mutation Carriers and Related Non-carriers, NeuroImage, In press

6.1 Introduction

Frontotemporal dementia (FTD) is a syndromic clinical variant of frontotemporal lobar degeneration (FTLD) which constitutes the third most prevalent group of neurodegenerative diseases with cognitive impairment [28,43]. Within recent years the clinical, molecular genetic and pathological classifications of FTD have evolved [8, 16]. Up to 40% of FTD cases are considered autosomal dominantly inherited. One of the rarer causes of familial FTD is *CHMP2B*-mutation related FTD with a pathogenic G-to-C transition in the acceptor splice site of *CHMP2B* exon 6 (c.532-1G>C) on chromosome 3 (FTD-3) [47]. The *CHMP2B* protein is a part of the Escort-3 complex involved in trafficking proteins destined for degradation in the Golgi apparatus. The molecular disease mechanism is not yet fully known. The disease was primarily described in a large Danish family [26, 36], but a novel nonsense mutation in the *CHMP2B* gene was recently identified in a Belgian familial FTD patient further supporting the gene to be involved in FTD [53].

The Danish FTD-3 family is very large with 33 identified patients and another 250 at risk for developing the disease within the next 60 years. The average FTD-3 clinical onset is 57 years with a broad range from 43 to 65. As the symptom onset is insidious the exact time of onset can be difficult to determine. Patients present with primarily a clinical syndrome of frontotemporal dementia with behavioural changes, apathy, sometimes aggression and/or changed eating behaviour. During the early course they rarely have language disturbances, but when neuropsychologically tested they often have impairment of more posteriorly cortically located functions such as memory and visuospatial problems. Urinary incontinence and gait disturbances are normally late features although they sometimes can be seen during the early years of the disease. Disease duration from diagnosis to death ranges from 2 to over 20 years.

In FTD cortical structural changes are *per se* primarily found in the frontal and tem-

poral lobes [7]. However, studies have also reported changes in the parietal lobes [4,25,55]. The aim of the present study is to assess cortical structural changes in preclinical FTD-3 *CHMP2B* mutation positive cases compared to mutation negative family members, and furthermore to assess a possible progression of cortical changes. A secondary aim has been to try to identify possible preclinical focal cortical abnormalities.

In vivo investigation of brain cortical structural changes using magnetic resonance imaging (MRI) has primarily employed manual or semi-automatic tracing of tissue boundaries to quantify anatomical structures [29, 42]. Such approaches are time consuming and subject to inter-rater variability. Therefore, automatic unbiased computational approaches have gained popularity when studying cohorts of subjects.

A variety of studies [54] have used voxel-based morphometry (VBM) to detect brain changes in diseases with FTLD and differences between disease FTLD sub-types and healthy controls since the introduction of the method [2, 60]. VBM performs voxel-wise comparisons between spatially aligned MRI scans of subject groups enabling identification of tissue growth and tissue loss throughout the entire brain. A related method is tensor-based morphometry (TBM) [3], analyzing the deformation field involved in non-linear mapping of images, such as mapping of intra-subject serial scans and mapping of subject to group average. This way, local expansions and contractions can be identified, and the tensor maps can be used to quantify longitudinal effects and differences between subjects and groups. TBM has been used in different areas, such as studying the developing human brain [12] and measuring degeneration in Alzheimer's disease [23]. TBM has been used less extensively than VBM within the field of FTLD, but recently more studies using TBM have been reported [4, 9, 52].

A third type of method for measuring cortical changes is the explicit segmentation of the cerebral cortex for measurements of cortical thickness using parametric or geometric deformable models [15, 21, 27, 31–33, 62, 64]. The cortex is explicitly or implicitly represented as surfaces of the white matter/gray matter boundary and the gray matter/cerebrospinal fluid boundary fitted to the images with subvoxel precision. This enables measurements of cortical thickness throughout the entire cortex with the advantage of standardized thickness measures, which is unavailable through VBM or TBM. In addition, VBM does not consider the cortical geometry, and cannot differentiate the cortical thickness of opposing walls in sulci. The drawback of surface based methods is the lack of quantification of subcortical regions, such as the thalamus, and basal ganglia. However, in studies where cortical structures are the objective and subcortical structures are less relevant, surface based methods are preferable. Surface based methods have been used to quantify changes in a variety of diseases, such as schizophrenia [34, 40, 63], obsessive-compulsive disorder [46], and Alzheimer's disease [35]. In diseases with FTLD surface based methods are apt, as degeneration is expected in the cortical lobes.

In this study we applied a surface based cortical segmentation method to serial MRI scans of preclinical individuals with *CHMP2B*-mutation related FTD and individuals without the mutation from the same family. Global volume measurements and local cortical thicknesses were determined from the cortical surfaces. Longitudinal and cross-sectional differences in cortical thickness were evaluated by lobe averages and by construction of statistical parametric maps.

6.2 Materials and Methods

The study adhered to the Helsinki II declaration, and was approved by The County Ethics Committees in the Counties of Aarhus, Viborg-Nordjylland and Copenhagen, Denmark. Subjects were recruited via a family contact group that distributes information within the Danish FTD-3 family. All participants signed the ethics approved informed consent form. All subjects had previously participated in genetic studies where they had been genetically tested for the *CHMP2B* mutation. The participating individuals and clinicians involved in scanning or with any direct contact to the participants have been and still are blinded

	Mutation carriers	Non-carriers
N	9	7
Male:female ratio	7:2	4:3
Age at baseline (years, mean±SD)	55.8±5.6	54.3±6.0
Inter-scan interval (years, mean±SD)	1.3±0.2	1.3±0.1

Table 6.1: Subject demographic information.

to the genetic status of the subjects.

6.2.1 Subjects

Nine individuals carrying the *CHMP2B* mutation and seven age-matched 1.-degree relatives without the mutation (non-carriers) from the third and fourth generation of the large Danish FTD-3 family were included in the study. All individuals were pre-symptomatic at the follow-up scan without any subjective complaints and working full time or recently retired due to age. Subjects and close relatives (usually the spouse) were interviewed in a semi-structured manner by an experienced clinician, used to assess FTD patients in general and the FTD-3 patients specifically. For all participants, neither the subject nor the informant described any changes in behaviour or personality. Some of the participants had previously agreed to neuropsychological screening where no abnormalities were found. There were no comorbidities affecting cerebral structure. Screening with standard instruments, such as the MMSE, is not valid for the present disease, as MMSE is known to be normal even though the patients have gross behavioural and personality changes. None of the participants showed any sign of insidious symptoms on neither the clinical interview nor the behavioural observation. Table 6.1 lists the demographic information of the subjects. The age range at baseline scan was from 45 to 65 years of age.

6.2.2 Image Acquisition

T1 MRI data were obtained on a 3T GE Signa Excite using a 3D inversion recovery fast spoiled gradient recalled sequence with TR/TE/TI = 6.3/2.9/750 ms, 14° flip angle, 0.94×0.94 mm^2 in-plane resolution (256×256 pixels), and a slice thickness of 1.2 mm. Full head images were acquired with 126 - 148 axial slices using a standard head coil. Standard non-volumetric T2 weighted (22 axial slices, TR/TE=4000/102 ms) images were also acquired. All images were checked for obvious acquisition artefacts such as motion and susceptibility artefacts which can affect the image processing and subsequent quantification.

6.2.3 Image Processing

The MRI data were linearly and nonlinearly registered to a common model using the ICBM152 [38]ăasătarget space. This was done using an automatic iterativeămultiresolution approach similar toăCollins et al. [14] and Janke et al. [30]. The common model was based on 85 subjects non-linearly registered, which resulted in an average with more well-defined image gradients than averages based on affine registrations, thus enabling more accurate registration of the target MRI data. Intensity non-uniformities originating from inhomogeneities in the magnetic field were corrected by the N3 algorithm [48]. A brain mask was created by iteratively fitting a deformable surface to the brain meninges using an algorithm similar to the brain extraction tool (BET) by Smith [50] (figure 6.1.a). The voxels inside the brain mask were classified into white matter (WM), gray matter (GM), and cerebrospinal fluid (CSF) using a fuzzy clustering algorithm (figure 6.1.b). Stereotaxic masks of the brain stem and cerebellum were applied to isolate the cerebral WM with an axial cut of separation approximately at lamina tecti. The ventricles and subcortical

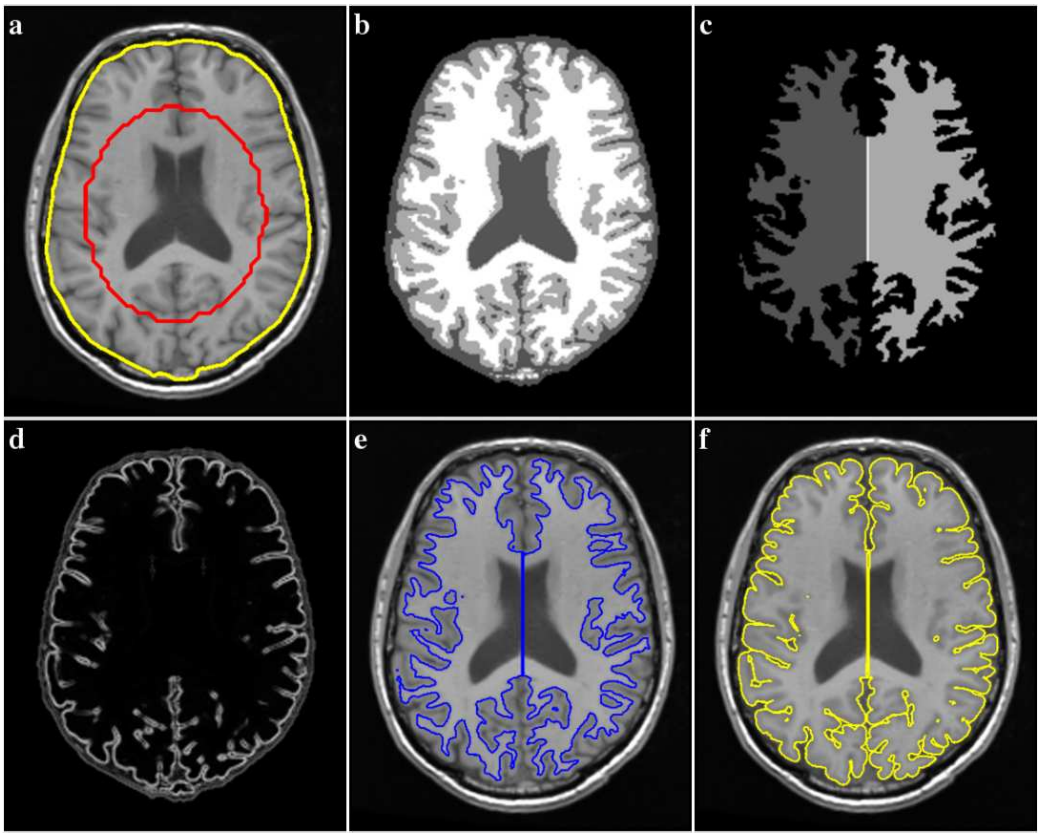

Figure 6.1: Extraction of the cortical boundaries. a) Spatially aligned MRI data with initial (red contour) and final (yellow contour) brain extraction contour superimposed. b) Brain tissue classified as WM, GM, and CSF. c) Ventricles and subcortical regions labelled as WM, and WM separated into hemispheres by a sagittal cut through corpus callosum. d) Edge map calculated from the fuzzy classifications. e) WM surface superimposed on the MRI data. f) GM surface superimposed on the MRI data.

regions were labelled WM to obtain a solid WM component for the following surface generation and cortical segmentation. The cerebrum WM was separated into two hemispheres by a mid-sagittal cut, and spherical topology of each hemisphere was obtained using a topology correction algorithm [11] (figure 6.1.c). An edge map of the GM/CSF interface was created using the membership volumes obtained by the previous fuzzy classification (figure 6.1.d). The edge map was used in the cortical boundary extraction as explained below. All processing steps were fully automatic.

6.2.4 Cortical Boundary Extraction

Cortical boundaries were identified using deformable surfaces and a force balancing scheme [39]. Each hemisphere was processed separately. An initial surface was obtained by applying an iso-surface algorithm on the topological correct WM component creating a closed triangulated surface [37]. The initial surface was deformed iteratively to the WM/GM boundary under influence of forces derived from the fuzzy classifications and the gradient image (6.1.e) [17]. The GM/CSF boundary was found by expanding the initial surface under influence of deformation forces derived from the surface normals, a gradient vector field [61], and the GM/CSF edge map shown in figure 6.1.d [18, 19]. The resulting surfaces accurately delineated the cerebral cortex reaching into the deep narrow sulci (figure 6.1.f). The cortex extraction method has been validated on healthy subjects and phantom

data [17–19], but has not yet been validated on neuropathological data. Therefore, cortical surfaces were visually inspected for segmentation errors, both using a 3D visualization tool and by superimposing the surfaces onto the original MR images.

6.2.5 Cortical Measurements

The surfaces generated for each hemisphere were triangular meshes each consisting of approximately 9×10^4 vertices uniformly distributed over the cortex. The cortical thickness was measured at each vertex as the distance between the WM and GM surface orthogonal to the GM surface using a combination of the surface normals and the nearest point (Euclidian) on the opposite surface. The nearest point distances between the surfaces were used to restrain how far along the surface normals to search for intersections of the opposite surface, thus preventing gross overestimation of the thickness where the lines defined by the GM surface normals do not intersect the WM surface within the same local topography. To increase the signal-to-noise ratio (SNR), cortical thickness measurements were blurred with a surface-based diffusion smoothing approximating a Gaussian kernel smoothing with 10 mm full-width half maximum (FWHM) [13]. Each hemisphere was divided into the main lobes based on an atlas in stereotaxic space that accompany the MRIcro software package [44], thus enabling regional based analysis. The atlas is defined as a labelled 3D image in stereotaxic space, and the subdivision of the surfaces was done by assigning a label to each vertex with the closest image label measured by Euclidian distance.

Tissue compartment volumes were estimated by utilizing the volumes enclosed by the GM and WM surfaces. The surfaces enclose the ventricles and subcortical regions from the lamina tecti and rostrally. Therefore, cerebrum volume was estimated by the volume enclosed by the GM surface minus the volume of the ventricles and subcortical regions, which were calculated from non-linearly aligned masks. WM volume was calculated similarly using the WM surface. Cortical volume was calculated as the difference between the cerebrum and WM volume. Compartment volumes were normalized by estimated total intracranial volume (eTIV) obtained from an intracranial mask non-linearly fitted to the images.

The acquired T2 images were visually checked for changes in WM lesions in order to ensure that WM lesions could not be an explanation for the results. We did not find any changes in the number of WM lesions over the course of the study. Only one subject had minor age-consistent WM-lesions. Thus there was not a clinically relevant difference in the number of WM-lesions between the two groups.

6.2.6 Surface Mapping

Surface mapping was applied to obtain vertex to vertex correspondence between intra-subject surfaces at baseline and follow-up, thus enabling point-wise differences in cortical thickness. After an initial rigid alignment of the surfaces using the ICP algorithm [5], vertex correspondence was calculated by minimizing a cost function expressing differences in mean curvature, orientation, and spatial position of the surface vertices [20, 51]. To facilitate the construction of statistical parametric maps of cortical differences between the groups, baseline surfaces were mapped to a reference surface chosen among the subjects. Surfaces at baseline were geometrically smoothed using a Laplace operator and mapped to the reference surface using the mapping method [20,51]. The smoothing was performed to reduce geometrical distortion and obtain more well-defined sulcal patterns.

6.2.7 Statistical Analysis

Distributions of cortical thickness across subjects were assumed to follow normal distributions, both with regard to regional averages and single point measurements. Differences

across groups were evaluated using t-tests with assumptions of unequal variance. Longitudinal differences within each group were evaluated using paired t-tests.

Statistical parametric maps were constructed to identify point-wise differences over time and between the groups. The maps were constructed by performing hypothesis testing at each vertex (approximately 10^5 vertices) of the reference surface testing change in cortical thickness or differences in cortical thickness between the groups. Problems with false positives related to multiple comparisons were addressed by calculating False Discovery Rate (FDR) corrected significance thresholds [24]. The statistical maps were blurred in the same way as the cortical thickness measurements to increase SNR and enhance focal effects. The blurring, which approximated a Gaussian kernel smoothing with 10 mm FWHM, had the effect of removing areas with scattered significance (diffuse effects) leaving only focal effects (clusters of significance). Focal effects were determined where significant different contiguous areas (clusters) exceeded an area of 20 mm^2 calculated as the surface area spanned by clusters of connected vertices with p-values below the significance threshold. Anatomical labels were assigned to the focal differences in the statistical parametric map by mapping labels from the stereotaxic atlas onto the reference surface as described above [44]. The area of the significant contiguous areas was summed within each region to report regional involvement.

To limit the intra-subject variability and increase statistical power to the group comparison, differences in cortical thickness and volume between groups were determined by comparing pooled data from mutation carriers (baseline and follow-up) with pooled data from non-carriers. This was done as subjects at a given time (baseline or follow-up) not necessarily are homogeneous, e.g. the disease stage in a mutation carrier at baseline may correspond to the disease stage in another mutation carrier at follow-up.

Annualized cortical atrophy rates in each lobe were calculated as percent decline of baseline lobe average thickness. To avoid magnifying noise in cortical thickness the atrophy rate per vertex was calculated as a ratio (r) as

$$r_i = \frac{m_{2,i} - m_{1,i}}{\Delta t(m_{2,i} + m_{1,i})} \tag{6.1}$$

where $m_{1,i}$ and $m_{2,i}$ are measurements at vertex i at respectively baseline and follow-up, and Δt is the subject scan interval. By normalizing with the summed thickness for baseline and follow-up unrealistically high atrophy rates, caused by baseline measurements close to zero, were avoided.

Asymmetry was evaluated by the left to right ratio between thickness measurements and atrophy rates averaged within the hemispheres and within the main lobes.

6.3 Results

6.3.1 Cortical Boundary Extraction and Compartment Segmentations

All generated cortical surfaces were found to be free of obvious segmentation errors by visually checking 3D rendered images as well as images of the original MR data with the surface contours superimposed. The masks fitted to the intra-cranial cavity, the ventricles, and subcortical regions were visually examined by superimposing them onto the original MR data. Intracranial and subcortical masks were found to accurately fit the images. However, examining the ventricular masks revealed problems of fitting to the posterior part of the lateral ventricles in two subjects of both groups. In these subjects the ventricular volume is underestimated. The inaccurate ventricular segmentations lead to overestimations of the WM and cerebrum volume while the cortical volume is unaffected by the ventricular segmentation. The segmentation accuracy was visually estimated to be similar for baseline and follow-up why it was assumed that longitudinal differences in WM and cerebrum volumes are unaffected by the segmentation errors.

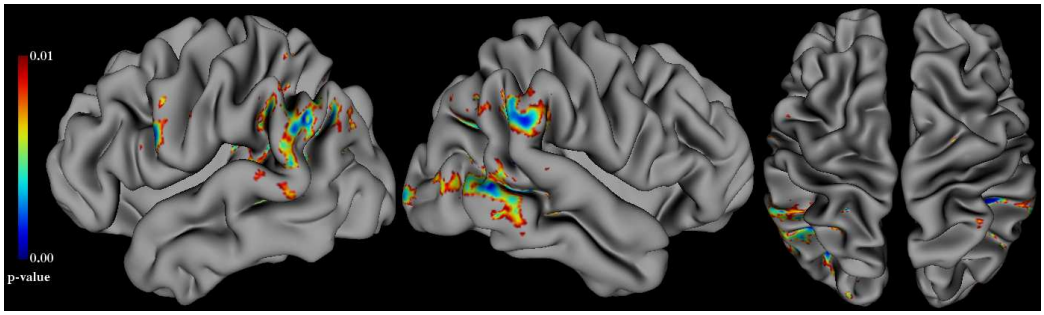

Figure 6.2: Statistical parametric map of differences in cortical thickness showing areas with $p < 0.01$ for one-sided t-test testing significant thinner cortex in mutation carriers compared to non-carriers. Map generated from pooled (baseline and follow-up) measurements and blurred with a diffusion smoothing approximating a Gaussian kernel smoothing with 10 mm FWHM.

6.3.2 Cross-sectional Differences

All lobes were significantly thinner in mutation carriers compared to non-carriers (table 6.2). For an FDR of 5% the statistical parametric maps implied an appropriate threshold of significance at $\alpha_{FDR} = 0.011$ for the left and $\alpha_{FDR} = 0.010$ for the right hemisphere. We chose a threshold of $\alpha_{FDR} = 0.01$ for both hemispheres. Figure 6.2 shows the blurred statistical parametric map of group differences in cortical thickness. Blurring the statistical map removed 85% of the significant points leaving highly significant clusters. Table 6.3 lists the anatomical regions that include the largest areas of significant difference. Significantly different regions were primarily found in the parietal lobes (24.8 cm^2) and the right temporal lobe (10.9 cm^2). Occipital lobes displayed less difference (6.2 cm^2), while only small significant differences were found in the left frontal lobe (2.4 cm^2). No part of the cortex was significantly thinner in non-carriers compared to the mutation group.

6.3.3 Longitudinal Effects

Analysis of group lobe averages revealed that in mutation carriers all lobes except the parietal lobes and the right temporal lobe were significantly thinner at follow-up compared to baseline (table 6.2). In non-carriers only the left occipital lobe was significantly thinner at follow-up.

None of the p-values in the statistical parametric maps of the longitudinal differences of cortical thickness was below α/N ($\alpha = 0.05, N = 10^5$), which resulted in no valid FDR adjusted significance threshold. Setting the threshold to $\alpha = 0.01$ showed no focal differences for either mutation carriers or non-carriers. Analyses of the unblurred statistical maps revealed scattered areas of significance in both frontal and temporal lobes in mutation carriers with more significance in the left lobes. Also, scattered areas of significance were found in the left occipital and left medial frontal lobes. In non-carriers scattered areas of significance were observed in the left occipital lobe. Lowering the significance threshold to $\alpha = 0.05$ revealed significant contiguous areas (1.4 cm^2) in the left temporal lobe of mutation carriers (see figure 6.3).

6.3.4 Atrophy Rates

Table 6.4 lists the annualized cortical atrophy rates within the main lobes for both groups. The cortical atrophy rate was significantly higher in the left frontal and left temporal lobe in mutation carriers compared to non-carriers. FDR analysis of the statistical parametric map of group differences in annualized cortical atrophy ratios (calculated by Eq. 6.1) provided no valid significance threshold for the same reason as described above. Setting

		Frontal lobe		**Temporal lobe**		**Parietal lobe**		**Occipital lobe**	
		Left	Right	Left	Right	Left	Right	Left	Right
MC	Baseline (mean±SD)	2.24±0.26	2.20±0.23	2.62±0.24	2.52±0.21	1.57±0.25	1.56±0.25	1.90±0.17	1.88±0.17
	Follow-up (mean±SD)	2.13±0.31	2.11±0.28	2.50±0.28	2.48±0.27	1.54±0.26	1.50±0.25	1.75±0.14	1.79±0.17
	Longitudinal difference (p-value)	0.005	0.015	0.007	0.335	0.440	0.193	0.002	0.003
NC	Baseline (mean±SD)	2.48±0.17	2.44±0.18	2.84±0.08	2.80±0.13	1.94±0.12	1.88±0.16	2.15±0.20	2.10±0.21
	Follow-up (mean±SD)	2.46±0.12	2.40±0.16	2.78±0.05	2.81±0.06	1.92±0.06	1.84±0.09	2.00±0.13	2.07±0.18
	Longitudinal difference (p-value)	0.629	0.312	0.112	0.736	0.614	0.348	0.030	0.496
Pooled group difference (p-value)		0.011	0.012	0.010	0.002	0.001	0.002	0.003	0.008

Table 6.2: Cortical thickness measurements (mm) averaged within main lobes at baseline and follow-up for mutation carriers (MC) and non-carriers (NC). Longitudinal differences evaluated by two-tailed paired t-test. Group differences evaluated by one-sided t-test with assumption of unequal variance on pooled measurements.

Anatomical region	Involved area, LH	Involved area, RH
Angular gyrus	655 mm^2	456 mm^2
Supramarginal gyrus	479 mm^2	463 mm^2
Middle temporal gyrus	221 mm^2	987 mm^2
Middle occipital gyrus	251 mm^2	221 mm^2
Superior temporal gyrus	158 mm^2	76 mm^2
Inferior parietal gyrus	226 mm^2	22 mm^2
Superior parietal gyrus	106 mm^2	No effect

Table 6.3: Anatomical regions with significantly ($p < 0.01$) thinner cortex in mutation carriers compared to non-carriers after smoothing. Only regions with an involved area of more than 1 cm^2 of either the left (LH) or right (RH) hemisphere are reported. The significant areas are visualized in figure 6.2.

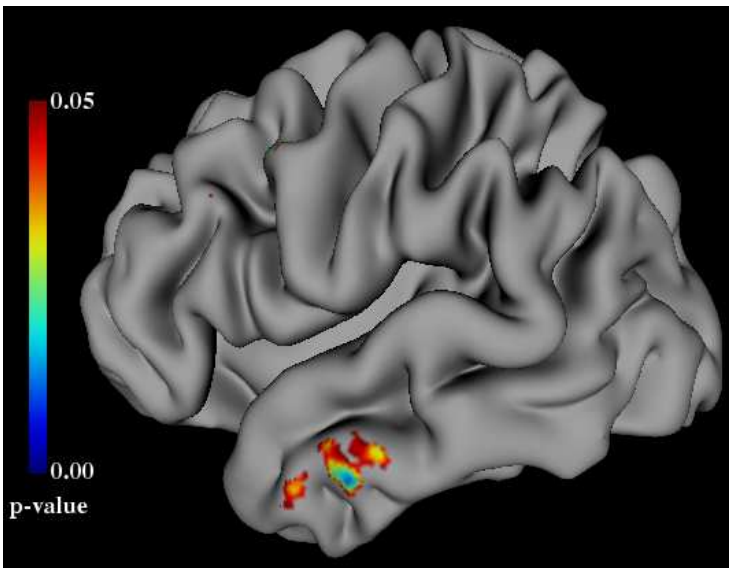

Figure 6.3: Statistical parametric map of longitudinal differences in cortical thickness in mutation carriers showing areas with $p < 0.05$ for paired t-test testing significant thinner cortex. Map blurred with a diffusion smoothing approximating a Gaussian kernel smoothing with 10 mm FWHM.

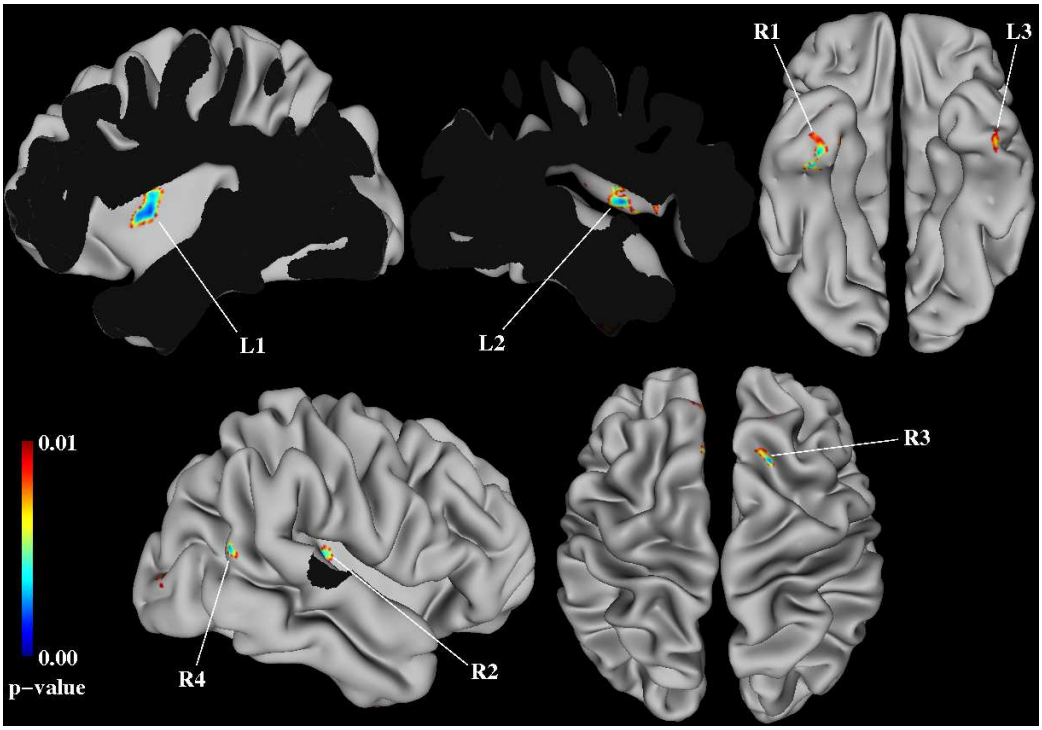

Figure 6.4: Statistical parametric map of significantly ($p<0.01$) higher atrophy ratios in mutation carriers. Map blurred with a diffusion smoothing approximating a Gaussian kernel smoothing with 10 mm FWHM. Surface parts have been removed for better visualization of regions buried by the lateral fissures. Labels correspond to the clusters listed in table 6.5. Cluster sizes may appear smaller than they are due to visualization on a partially flattened surface.

the significance threshold to $\alpha = 0.01$ on the blurred map revealed several focal effects (figure 6.4). Blurring the statistical map removed 78% of the statistically significant points leaving only highly focal effects. Clusters of significantly higher atrophy ratios with an area >20 mm^2 are listed in table 6.3 along with the involved anatomical regions. Higher atrophy ratios were found in both left and right frontal and temporal lobes. Especially the left insular cortex had a higher atrophy ratio in the mutation group (1.61 cm^2), but also the right inferio-temporal region (0.58 cm^2) and the right superior frontal gyrus (0.42 cm^2) showed focal differences.

6.3.5 Volume Measurements

Table 6.6 lists the measured cerebrum, WM, and cortical volumes, p-values for longitudinal differences within each group, and p-values for differences between the groups. Mutation carriers had significantly smaller cortical volume at follow-up compared to baseline (p=0.007). The cortical volume of non-carriers decreased, but the volume loss was not significant (p=0.142). Cerebrum and WM volumes were not significantly different at follow-up in either group. All cerebral volumes were significantly smaller in mutation carriers compared to non-carriers. The annualized percentage volume loss corrected for eTIV was 0.3 ± 1.4% cerebrum, -1.4 ± 2.2% WM, and 2.6 ± 2.2% cortex for mutation carriers. Annualized volume loss for non-carriers was 0.1 ± 1.4% cerebrum, -0.9 ± 2.0% WM, and 1.1 ± 1.8% cortex. Rates of volume loss were not significantly different between groups, however there was a trend for higher cortical volume loss in mutation carriers (p=0.17).

	Frontal lobe		**Temporal lobe**		**Parietal lobe**		**Occipital lobe**	
	Left	Right	Left	Right	Left	Right	Left	Right
MC (mean±SD)	4.18±3.73	3.42±3.51	3.74±3.16	1.37±3.75	1.52±5.30	3.14±6.87	6.15±4.03	3.91±2.97
NC (mean±SD)	0.50±3.51	1.15±2.86	1.44±1.96	0.48±2.86	0.81±4.57	1.59±4.89	4.77±5.53	0.84±3.78
Difference (*p*-value)	0.032	0.088	0.048	0.141	0.388	0.303	0.295	0.052

Table 6.4: Annualized atrophy rates as percent decline of baseline thickness for mutation carriers (MC) and non-carriers (NC). Difference between groups evaluated as one-sided t-test with assumption of unequal variance.

Cluster	**Area (mm^2)**	**Lobe**	**Main involved anatomical regions**
L1	120.4	Left frontal	Insula (109.5 mm^2)
L2	119.2	Left frontal	Rolandic operculum (74.8 mm^2) Insula (41.8 mm^2)
L3	22.4	Left temporal	Inferior temporal gyrus (22.4 mm^2)
R1	53.4	Right temporal	Fusiform gyrus (29.7 mm^2) Inferior temporal gyrus (23.7 mm^2)
R2	46.5	Right temporal	Transverse temporal gyrus (44.3 mm^2)
R3	35.3	Right frontal	Superior frontal gyrus (31.8 mm^2)
R4	22.6	Right temporal	Middle temporal gyrus (21.0 mm^2)

Table 6.5: Clusters of statistically significant higher atrophy ratios in mutation carriers compared with non-carriers. Clusters with significant contiguous areas >20 mm^2 are reported. Clusters are visualized in figure 6.4.

		Cerebrum	**White matter**	**Cortex**
MC	Baseline (mean±SD)	980±52	570±31	409±42
	Follow-up (mean±SD)	969±48	575±30	394±49
	Longitudinal diff (p-value)	0.161	0.348	0.005
NC	Baseline (mean±SD)	1048±42	585±32	463±35
	Follow-up (mean±SD)	1041±26	589±27	453±30
	Longitudinal diff (p-value)	0.420	0.501	0.086
Group differences (p-value)		0.002	0.175	0.005

Table 6.6: Compartment volumes (ml) corrected by eTIV for mutation carriers (MC) and non-carriers (NC) at baseline and follow-up. Longitudinal differences were adjusted for inter-scan interval and evaluated by two-tailed paired t-test. Group differences were evaluated by two-tailed t-test with assumption of unequal variance on pooled group measurements.

6.3.6 Asymmetry

Asymmetry ratios between hemispheres revealed a trend towards a thinner cortex in the right hemisphere in both mutation carriers (p=0.121) and non-carriers (p=0.061). By evaluating the averaged cortical thicknesses within lobes significant asymmetry was found in the frontal lobes (MC: p=0.046, NC: p=0.013) and parietal lobes (MC: p=0.033, NC: p=0.007) with right lobes being thinner in both groups. No asymmetry was found in the occipital lobes in either group, while mutation carriers had significantly thinner right temporal lobes (p=0.002). Evaluating the cortical atrophy rates, no asymmetry between hemispheres was found in either group.

6.4 Discussion

6.4.1 Cortical Thickness

After a 16 month follow-up, presymptomatic *CHMP2B* mutation carriers showed a significantly thinner cortex in the occipital and frontal lobes and the left temporal lobe. This is consistent with findings of other longitudinal studies of other types of symptomatic FTD patients [4, 10]; however, to our knowledge this is the first study describing cortical thinning in premanifest FTD disease.

Even though the statistical parametric maps with FDR adjusted significance threshold did not show significant focal atrophy in either group, the unblurred maps revealed scattered areas of atrophy in the same lobes, which were significantly thinner when averaging within the lobar measurements. Lowering the significance threshold to $\alpha = 0.05$ showed focal effects in the left middle temporal gyrus (figure 6.3)

When comparing the two groups (with and without the *CHMP2B* mutation) the overall lobe averages were significantly thinner in mutation carriers, whereas the statistical parametric maps revealed more focal differences (figure 6.2). Focal differences were mainly found in the parietal and temporal gyri, while almost no differences were found in the frontal lobes. However, due to the small number of subjects in both groups and preclinical stage of mutation carriers these differences may simply reflect normal variations in cortical thickness; and not necessarily a pathological effect. This is supported by the focal differences in atrophy ratio, which displayed a different pattern (figure 6.4). We consider change in cortical thickness a statistically stronger metric than the absolute cortical thickness when dealing with such small number of subjects. When examining the statistical parametric map of focal differences of the atrophy ratio, the right frontal lobe was also involved, while the occipital lobes had no focal effects. The atrophy ratio map reported more symmetrically distributed focal differences than the direct cortical thickness cross-sectional comparison. Specifically, the insular cortex (primarily left), the inferio-temporal regions, and the superior frontal gyri were those with the most pronounced focal effects (figure 6.4).

The anterior insula have been reported to be involved in several types of FTLD, mostly bilateral [6, 45, 58], but also in some cases in the left anterior insula [25, 59] and associated with progressive non-fluent aphasia [41]. Earlier examinations of patients with the *CHMP2B* mutation have shown varying degree of aphasia [26], though it is not a primary symptom of the disease. Hyperorality and changed eating behaviour has been observed in FTD-3 patients [26], and the atrophy patterns involving the insula areas found here share overlapping patterns with those found in FTLD types with abnormal eating behaviour [58]. Thus several of the symptoms observed in patients can be related to the preclinical structural changes found in this study. The two distinct patterns expressed by the group thickness differences and the group atrophy differences indicate that patterns of cortical thickness may not alone reveal the affected anatomical regions. Thus using only one MRI scan to establish a "clinical" FTD-3 diagnosis in a single *CHMP2B* mutation positive subject seems impossible at the preclinical stage studied here. A follow-up scan

is necessary to assess the atrophy pattern.

Results of cortical thickness based on the present method may not be directly comparable with results obtained by VBM analyses. VBM reports statistically significant clusters of GM change without considering the sulcal geometry. Small clusters in opposing parts of a sulcus may be insignificant when measuring cortical thickness because of the relatively large geodesic distance between the clusters, while in VBM they could converge into one large significant cluster because of the relatively small Euclidian distance between the clusters. Thus it is important to consider sulcal geometry when measuring focal effects [22]. Therefore, we included volumetric measurements to better compare our findings with results from previous studies, which used volumetric or VBM measurements, and to evaluate the sensitivity of volumetric measurements compared to cortical thickness.

6.4.2 Cerebral Volumes

The mutation carriers showed on average an annualized change in volume of approximately twice the magnitude of the non-carriers. Studies have reported annualized GM volume loss in healthy middle-aged and elderly persons of approximately 0.2% without WM loss [1,49]. Our measurements of average cortical volume loss (1.1%), though not significant (p=0.14), are in the high end compared to previous findings in healthy subjects. The small number of subjects (n=7) and significant normal variation may explain the difference. Unlike mutation carriers, both increase and decrease of cortical volume was measured in non-carriers, but rates of cortical volume loss were not significantly (p=0.17) higher in mutation carriers.

The averaged annualized cerebrum volume loss of 0.3% in mutation carriers was insignificant and suggested no change in whole-brain volume. Recent findings in ubiquitin positive FTLD reported whole-brain volume loss of 1.7%/year [56, 57]. These studies involved clinically diagnosed FTD patients above age 55 (average ages of 72/73 years) in contrast to the asymptomatic subjects in the present study. The whole-brain volume loss found by Whitwell et al. indicates an accelerated atrophy rate compared to the younger asymptomatic mutation carriers studied here, where the loss of tissue seems too subtle to be detected by whole-brain measures. However, cortical volume decreased significantly with 2.6% per year on average while a trend (p=0.08) for increased WM volume was observed (1.4%).

The increase of WM volume in both mutation carriers (1.4%) and non-carriers (0.9%), though not significant (p=0.08, p=0.26), was unexpected. Other studies have shown no WM volume change in aged healthy subjects [49] and only a slight increase in WM volume in non-aged healthy subjects [1]. The WM volume was calculated as the volume enclosed by the WM surface minus an estimated volume of the ventricles and subcortical regions. Ventricular and subcortical volumes were estimated using atlas masks non-linearly aligned to the images. Examining the accuracy of these masks revealed problems of fitting to the posterior part of the lateral ventricles in some subjects, why the ventricular volumes may be regarded as crude estimates affecting the accuracy of the calculated WM volume. Similarly, inaccurate ventricular volumes also affect the cerebrum volume estimates. To improve the WM and cerebrum volume estimates the ventricles could be explicitly segmented, e.g. by the use of deformable surfaces, which would also provide measures of ventricular enlargement.

The study did not show significant differences between mutation carriers and non-carriers when testing for global volumetric longitudinal effects. Nevertheless, using cortical thickness measurements we were able to determine higher atrophy rates in lobes, and even identified focal differences between the groups. This indicates that regional and focal cortical thickness measurements are more sensitive than global brain volume or tissue compartment measurements when quantifying cortical structural changes.

6.4.3 Limitations of the Study

The main limitation of the study is the low number of subjects examined. This affects the statistical power of the measured differences and complicates the assessment of how measurements are distributed. The assumption of normally distributed measurements, which was made on the grounds of biological variations tend to be normally distributed, may therefore be incorrect. It was not possible to recruit more subjects, as they had to be 1.-degree relatives of the same family.

The results may be affected by the within subject variability between the two scans. A third serial scan would provide more confident longitudinal measurements. An additional source of error could arise from the surface mapping used across subjects. Specific anatomical locations may be inaccurate, as a point on a cortical surface may be assigned a different anatomical label before mapping to the reference surface, if it was to be labelled by an expert anatomist. However, the mapping method used ensures that gyral points are mapped to a reference gyrus and sulcal points are mapped to a reference sulcus, thus cortical thickness comparisons are kept within the same cortical topography. Additionally, surface based registration has been shown to be more accurate across subjects than traditional image registrations [22].

Controlling the rate of falsely rejecting the null hypothesis in multiple comparison as used to construct the statistical parametric maps was attempted with the FDR method [24]. However, only the map calculated for the differences in absolute cortical thickness of pooled group data provided FDR corrected significance thresholds. Other statistical maps had no p-values less than α/N ($\alpha = 0.05, N = 10^5$) thus the FDR method removed all significance. This is an effect of the low number of subjects used in the study. Still, to enable interpretations of the results, it was decided to report the statistical maps without the FDR corrected thresholds. The blurring of the statistical maps removed between 78% and 100% of the statistically significant points ($p<0.01$), leaving clusters of significance in the map. Thus it can be argued that such blurring removes most of the false positives in the statistical parametric maps. Furthermore, most of the found focal effects are bilateral, which seems unlikely if they were caused by spurious results.

The atlas used for assigning anatomical labels to the surfaces is defined as a 3D image, and the procedure of assigning labels by Euclidian distance may lead to uncertainties in the exact anatomical designation of the significant pathological effects. However, as the anatomical regions used in the study are relatively large, uncertainties are limited to effects in the border regions and are considered not to affect the interpretation.

Finally, the crude estimates of ventricular volume affect the measures of WM and cerebrum volume. Therefore, the reported volumetric changes and differences of these compartments should be taken lightly. However, the volume measurements of the cortex are considered accurate, as these measurements are not influenced by the ventricular volume estimations.

6.4.4 Conclusion

We have shown that global and focal cortical changes can be measured in asymptomatic FTD-3 *CHMP2B* mutation positive subjects by using automatic cortical delineation. Global cortical volumetric changes were statistically significant, but whole-brain changes were of a lower rate than rates previously reported in other types of clinically manifest FTD patients. Focal cortical changes were identified by cortical thickness measurements, and the results indicated that such local measures have higher sensitivity for detecting small changes than global volumetric measures. Because of normal variations in cortical thickness and the low number of subjects studied annualized atrophy rates were considered the most reliant features describing differences between mutation carriers and non-carriers. Symptoms previously reported from patients with the *CHMP2B* mutation could be associated with the affected anatomical regions and our results further support the pathogenicity of the *CHMP2B* c.532-1G>C mutation. Comparing presymptomatic FTD-

3 *CHMP2B* mutation positive individuals with individuals from the same family without the *CHMP2B* mutation revealed bilaterally increased atrophy rates in the inferio-temporal cortex, the superior frontal cortex, and the insular cortex.

Acknowledgments

The study was supported by the Danish MRC: grant 22-04-0458 and the Danish National Research Foundation (L.Ø). MR technician Dora Ziedler, CFIN Aarhus University Hospital, Denmark is thanked for her help with the scans.

References

[1] J. S. Allen, J. Bruss, C. K. Brown, and H. Damasio. Normal neuroanatomical variation due to age: The major lobes and a parcellation of the temporal region. *Neurobiology of Aging*, 26(9):1245–1260, 2005.

[2] J. Ashburner and K. J. Friston. Voxel-based morphometry - the methods. *NeuroImage*, 11(6 I):805–821, 2000.

[3] J. Ashburner, C. Hutton, R. Frackowiak, I. Johnsrude, C. Price, and K. Friston. Identifying global anatomical differences: Deformation-based morphometry. *Human Brain Mapping*, 6(5-6):348–357, 1998.

[4] B. Avants, M. Grossman, and J. C. Gee. The correlation of cognitive decline with frontotemporal dementia induced annualized gray matter loss using diffeomorphic morphometry. *Alzheimer Disease and Associated Disorders*, 19(SUPPL. 1):S25–S28, 2005.

[5] P. J. Besl and N. D. McKay. A method for registration of 3-d shapes. *IEEE Transactions on Pattern Analysis and Machine Intelligence*, 14(2):239–256, 1992.

[6] M. Boccardi, F. Sabattoli, M. P. Laakso, C. Testa, R. Rossi, A. Beltramello, H. Soininen, and G. B. Frisoni. Frontotemporal dementia as a neural system disease. *Neurobiology of Aging*, 26(1):37–44, 2005.

[7] M. Broe, J. R. Hodges, E. Schofield, C. E. Shepherd, J. J. Kril, and G. M. Halliday. Staging disease severity in pathologically confirmed cases of frontotemporal dementia. *Neurology*, 60(6):1005–1011, 2003.

[8] N. J. Cairns, E. H. Bigio, I. R. A. Mackenzie, M. Neumann, V. M. . Lee, K. J. Hatanpaa, C. L. White III, J. A. Schneider, L. T. Grinberg, G. Halliday, C. Duyckaerts, J. S. Lowe, I. E. Holm, M. Tolnay, K. Okamoto, H. Yokoo, S. Murayama, J. Woulfe, D. G. Munoz, D. W. Dickson, P. G. Ince, J. Q. Trojanowski, and D. M. A. Mann. Neuropathologic diagnostic and nosologic criteria for frontotemporal lobar degeneration: Consensus of the consortium for frontotemporal lobar degeneration. *Acta Neuropathologica*, 114(1):5–22, 2007.

[9] V. A. Cardenas, A. L. Boxer, L. L. Chao, M. L. Gorno-Tempini, B. L. Miller, M. W. Weiner, and C. Studholme. Deformation-based morphometry reveals brain atrophy in frontotemporal dementia. *Archives of Neurology*, 64(6):873–877, 2007.

[10] D. Chan, N. C. Fox, R. Jenkins, R. I. Scahill, W. R. Crum, and M. N. Rossor. Rates of global and regional cerebral atrophy in ad and frontotemporal dementia. *Neurology*, 57(10):1756–1763, 2001.

[11] L. Chen and G. Wagenknecht. Automated topology correction for human brain segmentation. volume 4191 LNCS - II, pages 316–323, 2006.

[12] M. K. Chung, K. J. Worsley, T. Paus, C. Cherif, D. L. Collins, J. N. Giedd, J. L. Rapoport, and A. C. Evans. A unified statistical approach to deformation-based morphometry. *NeuroImage*, 14(3):595–606, 2001.

[13] M. K. Chung, K. J. Worsley, S. Robbins, T. Paus, J. Taylor, J. N. Giedd, J. L. Rapoport, and A. C. Evans. Deformation-based surface morphometry applied to gray matter deformation. *NeuroImage*, 18(2):198–213, 2003.

[14] D. L. Collins, P. Neelin, T. M. Peters, and A. C. Evans. Automatic 3d intersubject registration of mr volumetric data in standardized talairach space. *Journal of Computer Assisted Tomography*, 18(2):192–205, 1994.

[15] A. M. Dale, B. Fischl, and M. I. Sereno. Cortical surface-based analysis: I. segmentation and surface reconstruction. *NeuroImage*, 9(2):179–194, 1999.

[16] S. Davion, N. Johnson, S. Weintraub, M. . Mesulam, A. Engberg, M. Mishra, M. Baker, J. Adamson, M. Hutton, R. Rademakers, and E. H. Bigio. Clinicopathologic correlation in pgrn mutations. *Neurology*, 69(11):1113–1121, 2007.

[17] S. F. Eskildsen, M. Uldahl, and L. R. Østergaard. Extraction of the cerebral cortical boundaries from mri for measurement of cortical thickness. *Progress in Biomedical Optics and Imaging - Proceedings of SPIE*, 5747(II):1400–1410, 2005.

[18] S. F. Eskildsen and L. R. Østergaard. Active surface approach for extraction of the human cerebral cortex from mri. *Lecture Notes in Computer Science (including subseries Lecture Notes in Artificial Intelligence and Lecture Notes in Bioinformatics)*, 4191 LNCS - II:823–830, 2006.

[19] S. F. Eskildsen and L. R. Østergaard. Quantitative comparison of two cortical surface extraction methods using mri phantoms. 4791 LNCS(PART 1):409–416, 2007.

[20] S. F. Eskildsen and L. R. Østergaard. Evaluation of five algorithms for mapping brain cortical surfaces. In C. R. Jung and M. Walter, editors, *Proceedings*. IEEE Computer Society, Oct. 12–15 2008.

[21] B. Fischl and A. M. Dale. Measuring the thickness of the human cerebral cortex from magnetic resonance images. *Proceedings of the National Academy of Sciences of the United States of America*, 97(20):11050–11055, 2000.

[22] B. Fischl, M. I. Sereno, R. B. H. Tootell, and A. M. Dale. High-resolution intersubject averaging and a coordinate system for the cortical surface. *Human Brain Mapping*, 8(4):272–284, 1999.

[23] N. C. Fox, W. R. Crum, R. I. Scahill, J. M. Stevens, J. C. Janssen, and M. N. Rossor. Imaging of onset and progression of alzheimer's disease with voxel-compression mapping of serial magnetic resonance images. *Lancet*, 358(9277):201–205, 2001.

[24] C. R. Genovese, N. A. Lazar, and T. Nichols. Thresholding of statistical maps in functional neuroimaging using the false discovery rate. *NeuroImage*, 15(4):870–878, 2002.

[25] M. Grossman, C. McMillan, P. Moore, L. Ding, G. Glosser, M. Work, and J. Gee. What's in a name: Voxel-based morphometric analyses of mri and naming difficulty in alzheimer's disease, frontotemporal dementia and corticobasal degeneration. *Brain*, 127(3):628–649, 2004.

[26] S. Gydesen, J. M. Brown, A. Brun, L. Chakrabarti, A. Gade, P. Johannsen, M. Rossor, T. Thusgaard, A. Grove, D. Yancopoulou, M. G. Spillantini, E. M. C. Fisher, J. Collinge, and S. A. Sorensen. Chromosome 3 linked frontotemporal dementia (ftd-3). *Neurology*, 59(10):1585–1594, 2002.

[27] X. Han, D. L. Pham, D. Tosun, M. E. Rettmann, C. Xu, and J. L. Prince. Cruise: Cortical reconstruction using implicit surface evolution. *NeuroImage*, 23(3):997–1012, 2004.

[28] R. J. Harvey, M. Skelton-Robinson, and M. N. Rossor. The prevalence and causes of dementia in people under the age of 65 years. *Journal of Neurology, Neurosurgery and Psychiatry*, 74(9):1206–1209, 2003.

[29] C. R. Jack Jr., R. C. Petersen, Y. C. Xu, P. C. O'Brien, G. E. Smith, R. J. Ivnik, B. F. Boeve, S. C. Waring, E. G. Tangalos, and E. Kokmen. Prediction of ad with mri-based hippocampal volume in mild cognitive impairment. *Neurology*, 52(7):1397–1403, 1999.

[30] A. L. Janke, R. Renwick, M. Budge, J. Pruessner, and D. L. Collins. Nonlinear multiresolution symmetric registration in automated segmentation of sub- and allocortical structures in mri. *Proceedings of ISMRM, 10th annual meeting, Toronto*, 2003.

[31] S. E. Jones, B. R. Buchbinder, and I. Aharon. Three-dimensional mapping of cortical thickness using Laplace's equation. *Human Brain Mapping*, 11(1):12–32, 2000.

[32] S. K. June, V. Singh, K. L. Jun, J. Lerch, Y. Ad-Dab'bagh, D. MacDonald, M. L. Jong, S. I. Kim, and A. C. Evans. Automated 3-d extraction and evaluation of the inner and outer cortical surfaces using a laplacian map and partial volume effect classification. *NeuroImage*, 27(1):210–221, 2005.

[33] N. Kriegeskorte and R. Goebel. An efficient algorithm for topologically correct segmentation of the cortical sheet in anatomical mr volumes. *NeuroImage*, 14(2):329–346, 2001.

[34] G. R. Kuperberg, M. R. Broome, P. K. McGuire, A. S. David, M. Eddy, F. Ozawa, D. Goff, W. C. West, S. C. R. Williams, A. J. W. Van der Kouwe, D. H. Salat, A. M. Dale, and B. Fischl. Regionally localized thinning of the cerebral cortex in schizophrenia. *Archives of General Psychiatry*, 60(9):878–888, 2003.

[35] J. P. Lerch, J. Pruessner, A. P. Zijdenbos, D. L. Collins, S. J. Teipel, H. Hampel, and A. C. Evans. Automated cortical thickness measurements from mri can accurately separate alzheimer's patients from normal elderly controls. *Neurobiology of Aging*, 29(1):23–30, 2008.

[36] S. G. Lindquist, H. Brændgaard, K. Svenstrup, A. M. Isaacs, and J. E. Nielsen. Frontotemporal dementia linked to chromosome 3 (ftd-3) - current concepts and the detection of a previously unknown branch of the danish ftd-3 family. *European Journal of Neurology*, 15(7):667–670, 2008.

[37] W. E. Lorensen and H. E. Cline. Marching cubes: A high resolution 3d surface construction algorithm. *Computer Graphics (ACM)*, 21(4):163–169, 1987.

[38] J. Mazziotta, A. Toga, A. Evans, P. Fox, J. Lancaster, K. Zilles, R. Woods, T. Paus, G. Simpson, B. Pike, C. Holmes, L. Collins, P. Thompson, D. MacDonald, M. Iacoboni, T. Schormann, K. Amunts, N. Palomero-Gallagher, S. Geyer, L. Parsons, K. Narr, N. Kabani, G. Le Goualher, D. Boomsma, T. Cannon, R. Kawashima, and B. Mazoyer. A probabilistic atlas and reference system for the human brain: International consortium for brain mapping (icbm). *Philosophical Transactions of the Royal Society B: Biological Sciences*, 356(1412):1293–1322, 2001.

[39] T. Mclnerney and D. Terzopoulos. Topology adaptive deformable surfaces for medical image volume segmentation. *IEEE Transactions on Medical Imaging*, 18(10):840–850, 1999.

[40] K. L. Narr, R. M. Bilder, A. W. Toga, R. P. Woods, D. E. Rex, P. R. Szeszko, D. Robinson, S. Sevy, H. Gunduz-Bruce, Y. . Wang, H. DeLuca, and P. M. Thompson. Mapping cortical thickness and gray matter concentration in first episode schizophrenia. *Cerebral Cortex*, 15(6):708–719, 2005.

[41] P. J. Nestor, N. L. Graham, T. D. Fryer, G. B. Williams, K. Patterson, and J. R. Hodges. Progressive non-fluent aphasia is associated with hypometabolism centred on the left anterior insula. *Brain*, 126(11):2406–2418, 2003.

[42] K. P. Rankin, H. J. Rosen, J. H. Kramer, G. F. Schauer, M. Weiner, N. Schuff, and B. L. Miller. Right and left medial orbitofrontal volumes show an opposite relationship to agreeableness in ftd. *Dementia and Geriatric Cognitive Disorders*, 17(4):328–332, 2004.

[43] E. Ratnavalli, C. Brayne, K. Dawson, and J. R. Hodges. The prevalence of frontotemporal dementia. *Neurology*, 58(11):1615–1621, 2002.

[44] C. Rorden and M. Brett. Stereotaxic display of brain lesions. *Behavioural Neurology*, 12(4):191–200, 2000.

[45] H. J. Rosen, M. L. Gorno-Tempini, W. P. Goldman, R. J. Perry, N. Schuff, M. Weiner, R. Feiwell, J. H. Kramer, and B. L. Miller. Patterns of brain atrophy in frontotemporal dementia and semantic dementia. *Neurology*, 58(2):198–208, 2002.

[46] Y. Shin, Y. Y. So, K. L. Jun, H. H. Tae, J. L. Kyung, M. L. Jong, Y. K. In, S. I. Kim, and S. K. Jun. Cortical thinning in obsessive compulsive disorder. *Human Brain Mapping*, 28(11):1128–1135, 2007.

[47] G. Skibinski, N. J. Parkinson, J. M. Brown, L. Chakrabarti, S. L. Lloyd, H. Hummerich, J. E. Nielsen, J. R. Hodges, M. G. Spillantini, T. Thusgaard, S. Brandner, A. Brun, M. N. Rossor, A. Gade, P. Johannsen, S. A. Sørensen, S. Gydesen, E. M. C. Fisher, and J. Collinge. Mutations in the endosomal escrtiii-complex subunit chmp2b in frontotemporal dementia. *Nature Genetics*, 37(8):806–808, 2005.

[48] J. G. Sled, A. P. Zijdenbos, and A. C. Evans. A nonparametric method for automatic correction of intensity nonuniformity in mri data. *IEEE Transactions on Medical Imaging*, 17(1):87–97, 1998.

[49] C. D. Smith, H. Chebrolu, D. R. Wekstein, F. A. Schmitt, and W. R. Markesbery. Age and gender effects on human brain anatomy: A voxel-based morphometric study in healthy elderly. *Neurobiology of Aging*, 28(7):1075–1087, 2007.

[50] S. M. Smith. Fast robust automated brain extraction. *Human Brain Mapping*, 17(3):143–155, 2002.

[51] M. Spjuth, F. Gravesen, S. F. Eskildsen, and L. R. Østergaard. Early detection of ad using cortical thickness measurements. *Progress in Biomedical Optics and Imaging - Proceedings of SPIE*, 6512(I):0L1–0L9, 2007.

[52] C. Studholme, V. Cardenas, R. Blumenfeld, N. Schuff, H. J. Rosen, B. Miller, and M. Weiner. Deformation tensor morphometry of semantic dementia with quantitative validation. *NeuroImage*, 21(4):1387–1398, 2004.

[53] J. van der Zee, H. Urwin, S. Engelborghs, M. Bruyland, R. Vandenberghe, B. Dermaut, T. De Pooter, K. Peeters, P. Santens, P. P. De Deyn, E. M. Fisher, J. Collinge, A. M. Isaacs, and C. Van Broeckhoven. Chmp2b c-truncating mutations in frontotemporal lobar degeneration are associated with an aberrant endosomal phenotype in vitro. *Human Molecular Genetics*, 17(2):313–322, 2008.

[54] J. L. Whitwell and C. R. Jack Jr. Comparisons between alzheimer disease, frontotemporal lobar degeneration, and normal aging with brain mapping. *Topics in Magnetic Resonance Imaging*, 16(6):409–425, 2005.

[55] J. L. Whitwell, C. R. Jack Jr., M. Baker, R. Rademakers, J. Adamson, B. F. Boeve, D. S. Knopman, J. F. Parisi, R. C. Petersen, D. W. Dickson, M. L. Hutton, and K. A. Josephs. Voxel-based morphometry in frontotemporal lobar degeneration with ubiquitin-positive inclusions with and without progranulin mutations. *Archives of Neurology*, 64(3):371–376, 2007.

[56] J. L. Whitwell, C. R. Jack Jr., V. S. Pankratz, J. E. Parisi, D. S. Knopman, B. F. Boeve, R. C. Petersen, D. W. Dickson, and K. A. Josephs. Rates of brain atrophy over time in autopsy-proven frontotemporal dementia and alzheimer disease. *NeuroImage*, 39(3):1034–1040, 2008.

[57] J. L. Whitwell, C. R. Jack Jr., J. E. Parisi, D. S. Knopman, B. F. Boeve, R. C. Petersen, T. J. Ferman, D. W. Dickson, and K. A. Josephs. Rates of cerebral atrophy differ in different degenerative pathologies. *Brain*, 130(4):1148–1158, 2007.

[58] J. L. Whitwell, E. L. Sampson, C. T. Loy, J. E. Warren, M. N. Rossor, N. C. Fox, and J. D. Warren. Vbm signatures of abnormal eating behaviours in frontotemporal lobar degeneration. *NeuroImage*, 35(1):207–213, 2007.

[59] G. B. Williams, P. J. Nestor, and J. R. Hodges. Neural correlates of semantic and behavioural deficits in frontotemporal dementia. *NeuroImage*, 24(4):1042–1051, 2005.

[60] I. C. Wright, P. K. Mcguire, J. . Poline, J. M. Travere, R. M. Murray, C. D. Frith, R. S. J. Frackowiak, and K. J. Friston. A voxel-based method for the statistical analysis of gray and white matter density applied to schizophrenia. *NeuroImage*, 2(4):244–252, 1995.

[61] C. Xu and J. L. Prince. Generalized gradient vector flow external forces for active contours. *Signal Processing*, 71(2):131–139, 1998.

[62] H. Xue, L. Srinivasan, S. Jiang, M. Rutherford, A. D. Edwards, D. Rueckert, and J. V. Hajnal. Automatic segmentation and reconstruction of the cortex from neonatal mri. *NeuroImage*, 38(3):461–477, 2007.

[63] U. Yoon, J. . Lee, K. Im, Y. . Shin, B. H. Cho, I. Y. Kim, J. S. Kwon, and S. I. Kim. Pattern classification using principal components of cortical thickness and its discriminative pattern in schizophrenia. *NeuroImage*, 34(4):1405–1415, 2007.

[64] X. Zeng, L. H. Staib, R. T. Schultz, and J. S. Duncan. Segmentation and measurement of the cortex from 3-d mr images using coupled-surfaces propagation. *IEEE Transactions on Medical Imaging*, 18(10):927–937, 1999.

Chapter 7

Discussion and Conclusion

This thesis contributes to the field of morphometry of the human cerebral cortex from MRI. The objective is to develop methods for quantifying cortical structural changes as found in neurodegenerative diseases and to investigate the ability of such methods to measure changes in preclinical individuals. A main goal is to differentiate between different neurodegenerative diseases by cortical atrophy patterns and identify clinical markers to aid in early diagnosis. The first step to this goal is to accurately measure the size and shape of the cerebral cortex. In this thesis, it is proposed to reconstruct the cortical structure by manifold surfaces. The next step towards the goal is to measure atrophy and identify similar patterns of atrophy in population groups. For this purpose, cortical mapping is proposed and mapping techniques are investigated. The last steps toward the goal of differentiating between neurodegenerative diseases by atrophy patterns involve applying the quantification methods in clinical studies. A first step is taken in that direction by applying the developed methods to individuals from a family with an inherited variant of frontotemporal dementia. The following discusses the cortical reconstruction, cortical mapping and application of quantification methods presented in this thesis.

7.1 Cortical Reconstruction

Successful cortical reconstructions use a combination of voxel based methods and deformable models. Voxel based methods are typically applied as preprocessing steps prior to a deformable model for the purpose of enhancing information of tissue boundaries and reducing manual interaction. The main focus of the thesis is on deformable models while preprocessing steps necessary for automatic cortex reconstruction has been implemented by use of existing methodologies. The following discusses the deformable surface algorithm as proposed during the thesis, followed by a discussion of the steps necessary for automatic and robust cortical reconstruction and finally reflections on computational expense is presented.

7.1.1 Deformable Surface Algorithm

As stated in the introduction, two criteria are important for surface reconstructions of the cerebral cortex. First, the surfaces must accurately model the underlying true anatomical boundaries. Second, the topology of the cortex must be preserved. To meet these criteria, a solution based on parametric deformable surfaces is suggested. By using parametric models, the topology criterion can be met if the initial surface has the correct topology and self-intersections are avoided during deformation. Methods for correcting surface topology [5,25] and methods to avoid self-intersections of parametric surfaces [21,39] have been proposed. By selecting proper algorithms to solve these problems, the focus of the study is to obtain as accurate cortical reconstructions as possible using deformable models.

In Paper I [12], it is demonstrated that a parametric deformable surface based on the classic balloon model [7] combined with a gradient vector flow force [53] is able to delineate even the tight sulcal folds. The deformation is based on a greedy algorithm [49] which is fast but prone to be trapped in local minima. However, by initializing the deformable surface close to the target boundaries, the probability of local minima is reduced and fast convergence is enabled. It is demonstrated that the proposed method is robust to image noise; increasing the noise level in the image to 9% only results in average errors less than half a voxel size compared to surfaces extracted from noiseless data. Finally, the paper reports that thickness measurements obtained from the reconstructed cortical surfaces are realistic compared to measurements found in post mortem studies.

The algorithm proposed in Paper I [12] has a few drawbacks. The surface position with lowest energy is searched for in a discrete search space, thus limiting the accuracy of the solution even if multiscale techniques are used. Furthermore, the method for enforcing spherical topology on the initial surface may produce anatomical inconsistencies in the surface. The initial surface is a tessellation of the WM of both cerebral hemispheres connected by corpus callosum. A tessellation of an unmodified WM voxel component usually results in a surface with several handles, where larger handles can be caused by additional inter-hemispheric connections such as the commissures. In addition, classification of subcortical regions often results in a mixture of WM and GM voxels which give rise to numerous topological errors. Therefore, the applied topology correction algorithm based on graph cutting [25] has difficulties producing surfaces with anatomically consistent appearance. In fact, in figure 2.6 on page 30 such anatomical inconsistencies can be observed as bridges across the ventricles.

In Paper II [13], the granularity problem is addressed by altering the deformation approach to calculate displacement vectors directly by the sum of force vectors. Furthermore, a local weighting strategy of the deformation forces is implemented to improve the accuracy and convergence of surfaces. Exploiting the close initial surface, normalized surface curvature is used to relax regularizing forces in curved regions and balance the use of the two external image forces for optimal modeling of tight sulci. The paper demonstrates that such a combination and weighting of forces is superior to approaches using only a pressure force [10] or only a gradient vector flow force [52].

In Paper III [14], the topology correction method is changed to a more robust and consistent approach [5]. The hemispheres are separated and ventricles and subcortical regions filled and thereby further optimizing the possibility for topologically correct and consistent surfaces of the neocortex. The paper demonstrates that the proposed algorithm is geometrically more accurate and faster than the widely used and freely available reconstruction algorithm FreeSurfer [10].

A Note on Novelty

The field of cortical morphometry is rapidly expanding and the progression is fast. At the time of publication of Paper I, several of the surface reconstruction methods referenced in the introduction of this thesis were not published. Several researchers around the world work on cortical surface reconstruction from MRI and this is reflected in the amount of literature on the subject. As noted in the introduction, recent methods seem to conform to the same strategy of reconstructing the outer cortical boundary by inflating a surface of the inner cortical boundary. This is indeed the same strategy adopted in this thesis. The main difference is how this deformation is performed. The combination of external image forces and weighting strategy presented in the papers of this thesis is considered unique. However, recent studies have pointed in similar directions as proposed here.

In a recent comparative study of eight deformable contour methods, it is concluded that new methods could combine features from existing methods to handle specific segmentation problems [30]. Specifically, a combination of a balloon model with a gradient vector flow (GVF) is given as an example. This combination is similar to what is presented in this thesis for the reconstruction of the outer cortical boundary. Another recent paper

propose a method for reconstructing the central layer of the cortex by combining a pressure force with a GVF force in the deformation process [37]. Again, this is similar to the approach described in this thesis with the difference that the target here is the outer cortical boundary. These studies confirm the novelty and performance of the cortical reconstruction approach suggested in this thesis.

7.1.2 Automation and Robustness

Large scale cohort studies call for automatic procedures to limit tedious and laborious manual interaction and to optimize consistency. A goal for the cortical reconstruction algorithm developed during the Ph.D. study is full automation. However, when dealing with biological images and complex target structures, this is not an easy task when robustness to image and object variation is also prioritized. Apart from the deformable surface algorithm, several other processing steps are involved in an automatic reconstruction procedure. These steps are performed to fulfill the preconditions and improve the accuracy of the deformable surface algorithm. The main precondition of the used deformable surface approach is initialization close to the target boundary. This is achieved by a good classification of the cerebral WM.

The steps taken to perform classification of the cerebrum WM include intensity non-uniformity correction, image registration to a stereotaxic space, brain extraction, intensity based classification into WM, GM and CSF and finally removal of brain stem and cerebellum as outlined in Paper I [12]. Such preprocessing steps are common for several cortical reconstruction algorithms [10, 24, 33, 35]. The performance, robustness and automation of cortical reconstructions depend on choices of algorithms to perform each step. For the cortical reconstruction presented in this thesis, these choices have remained more or less the same throughout the course of the Ph.D. study and are in the following briefly discussed in connection with automation and robustness.

Correction of intensity non-uniformities caused by inhomogeneities in the radio frequency field is usually needed for improving intensity based classifications. The inhomogeneity increases with field strength and is very pronounced at 3 Tesla. Various algorithms to correct the intensity non-uniformities in the images have been proposed and a number of these are publicly available [31]. In this thesis, the freely available N3 algorithm is used [43]. This algorithm is automatic and performs well on images generated by both 1.5 and 3 Tesla scanners [3].

Automatic image registration to a stereotaxic space is a crucial step involved in almost all structural studies as well as many functional studies. For this reason, enormous effort has been put into developing robust registration and freely available, well-performing methods exists [9, 11, 18, 34, 51] [1]. In this thesis, registration is done using an automatic procedure [8, 9] which is found to perform well for the purposes of the cortical reconstruction. The registration procedure need not be highly accurate, as the purpose for the cortical reconstruction is gross localization of the major anatomical parts. Thus, the registration is used for the removal of brain stem and cerebellum. A registration working for the wide variability of brain anatomy is usually not sufficiently accurate to be used for brain extraction as well.

Brain extraction is necessary as several tissues in the human head have overlapping T1 intensities which impairs the tissue classification. Such an algorithm must be able to robustly extract the brain tissues without removing parts of the brain and optimally without including proximate tissues such as dura mater, exterior veins and cartilage. Several brain extraction methods have been proposed [40]. None of the freely available methods [10, 41, 44, 47] are found suitable for purposes of robust and automatic cortical reconstruction. Therefore, in this Ph.D. study, a brain extraction algorithm has been developed similar in spirit to the brain extraction tool by Smith [44]. Even though this algorithm works well for most data, brain extraction of elderly subjects has proved difficult to perform

[1] For a list of available software tools see http://www.cma.mgh.harvard.edu/iatr/

robustly and accurately. The main problem is the inclusion of dura mater and superior sagittal sinus which may have intensities similar to WM, thus complicating the cerebrum WM classification. The problem is probably related to change in MRI signal intensity which is an effect of age [32].

Classification of the cerebral tissues into WM, GM and CSF can be performed using several of the classification approaches described in the introduction. Particularly, in this thesis a fuzzy clustering approach is used [23]. This classification algorithm generally performs well; however, no formal comparisons with other algorithms were carried out during the Ph.D. study. The algorithm influences the surface convergence and reconstruction accuracy as the fuzzy membership images produced are used in the deformation process. In Papers I and III the accuracy of the reconstructed surfaces is shown to be around half a voxel size, which is why the accuracy of the tissue classification is deemed acceptable.

Generally, the cortical reconstruction procedure runs fully automatic on most MRI scans. However, a small fraction of scans of elderly individuals need manual interaction to remove parts of the dura mater prior to tissue classification. This is caused by insufficient brain extraction. It is my experience that brain extraction remains the main obstacle to a fully automatic and robust cortical surface reconstruction method.

7.1.3 Computational Expense

The time it takes to generate accurate cortical reconstructions may be relevant in some scenarios. If cortical reconstructions are to be used in diagnostics or preoperative planning, the computational delay may be a nuisance at best and critical at worst. However, in most cases the reconstruction time is not important though a fast reconstruction significantly reduces the time needed to obtain results in large scale studies. Especially when repeated trials are necessary to tune parameters, high throughput is desirable. In any case, optimization of computational expense should be prioritized after accuracy, robustness and automation.

Traditionally, optimization of parametric deformable surfaces is very slow if convergence to a global minimum must be guaranteed. Global minimum solutions can be obtained by various minimization algorithms [2, 45]. The deformation methods applied to propagate the deformable surfaces in this thesis do not guarantee convergence to a global minimum. This enables faster convergence and because of the close initialization, the models are less vulnerable to problems of local minima. Applying a global minimization algorithm does not necessarily improve the accuracy as the global minimum may not be the most accurate delineation of the cortical boundaries due to noise and artefactual irregularities found in MRI. Global minimum algorithms are suited for problems where the initial guess is far from the solution. However, in cortical reconstructions, the initial guess can be determined close to the solution as robust classification of the cerebrum WM can be achieved. Therefore, the need for convergence of surfaces initialized far from the target boundary seems artificial and computational expensive optimization algorithms guaranteeing a global minimum appear superfluous for the purpose of cortical reconstruction.

Geometric deformable models have become popular solutions to the cortical reconstruction problem since the introduction of topology preservation to the level set method by the use of digital topology [26]. An argument for these models are the low computational expense compared to parametric models. Authors claim that self-intersection prevention is very computational intensive in parametric deformable surface models [24, 27]. The solution to cortical reconstructions with self-intersection avoidance presented in this thesis is reasonably fast. Deformation of the GM/CSF surface is done in approximately 5 min. per hemisphere on a 2.8 GHz Opteron CPU. But compared to new level set methods, where the deformation process is measured in seconds [42], the parametric high resolution models are outperformed. However, seen in the perspective of the entire process needed for cortical reconstruction, the deformation process is only a fraction of the computational time used. Intensity correction and classification algorithms often demand similar compu-

tational resources and if high-dimensional non-linear registration methods are used, the preprocessing steps may be a factor ten more time consuming than the parametric deformable models. Thus, in practical cortex reconstruction, the deformation algorithm is not the computational bottle neck if a suitable minimization method is chosen.

7.2 Cortical Surface Mapping

The cortical reconstructions enable detailed morphological quantifications of the entire neocortex. To fully utilize these high resolution measurements and identify differences over time and between subjects, point correspondence between cortical surfaces is necessary. In this thesis the subject of cortical surface mapping for the purpose of point correspondence is briefly investigated in paper IV [15].

The main problem when comparing different cortical surfaces is the great variation in folding patterns. Usually comparison is enabled by mapping the manifold surfaces to each other or to a template. If the manifold properties of the surfaces are maintained by a mapping, it is hard, if not impossible, to match the cortical folding patterns and thereby matching gyri to sulci is unavoidable without loosing information. As the cortex generally is thicker at the top of gyri than at the bottom of sulci, such matching may lead to unreliable measurements of difference in cortical thickness. By relaxing the manifold properties in the mapping, it is possible to only match areas of the surfaces with similar topography. A mapping method with this purpose is proposed in paper IV and evaluated along with methods that maintain the manifold properties when mapping. The evaluation confirmed that if the manifold properties are maintained, high topographical errors occur. The methods achieving low topographical errors due to manifold relaxation result in neighboring vertices jumping between gyri and sulci leading to large geodesic distances. This is also undesirable as neighboring measurements are not independent and such large geodesic distances imposed by a mapping may render the measurements unreliable. Though the proposed algorithm maintains the most information (high coverage) of the five evaluated methods, large geodesic errors are not acceptable.

A solution to maintain manifold properties and limit the topographic errors could be to develop different brain templates each reflecting a "type of brain" categorized on the basis of the cortical folding patterns. This way a subject cortex could be matched to the best template representing the type of cortical folding of the subject. How many different templates would be needed and to what detail the categorization can be performed remains to be investigated. Such an approach would be feasible only if the number of different classes is limited.

Another observation supporting the categorization of brains according to the cortical folding pattern is the large errors and large standard deviations in the landmark test performed in the paper. All mapping methods resulted in large average geodesic distances to the manually placed landmarks. However, it was observed that in some cases the mapping was very close to the landmarks while in others the geodesic errors were large as the high standard deviations also suggest. This indicates that some cortices are generally better matches which further support the categorization of the brains for the purpose of brain mapping. By specializing the brain templates for specific cortical patterns, the geodesic landmark errors could be reduced.

7.3 Application on Neurodegenerative Diseases

Demonstrating the use of the cortex reconstruction method on data from individuals with a neurodegenerative disease is crucial, as methods behaving well on simulated data and data from non-pathological brains may fail on pathological brains. In this thesis, the cortical reconstruction is applied to individuals from a family with an inherited variant of frontotemporal dementia where a pathogenic mutation has been identified on chromosome

3 (FTD-3). Nine individuals with the mutation and seven without the mutation are included in the study.

The study which is documented in Paper V [16] revealed that comparison of groups using absolute cortical thickness need more subjects than the 16 used in order to compensate for the significant normal variation in cortical thickness. However, when including the temporal dimension, atrophy rates can be estimated which are statistically stronger when comparing pathological effects. This is reflected in the different statistical maps generated by respectively absolute cortical thickness and annualized atrophy ratios. The atrophy ratio statistical map seems more plausible as it shows bilateral effects contrary to the statistical map of differences in absolute cortical thickness. In the specific variant of frontotemporal dementia, bilateral effects are expected although the degenerative manifestations of the disease remain to be fully mapped.

The cortical reconstruction provides means for measuring the cerebral volumes. This is done by calculating the interior volume of the closed surfaces of the WM and GM. Cortical volume is determined by the difference in volume between the surfaces. In the FTD-3 study, only the cortical volume in mutation carriers decreased significantly while trend for increased WM volume was observed. By only modeling the neocortex, estimations of WM volume cannot be directly obtained why volumes were adjusted by masks of ventricles and subcortical structures. Ventricular enlargements are expected over time and the increased WM volume may be due to inability of the masks to fit to the altered ventricles. Ventricular volume can be measured more elegantly by modeling the ventricles explicitly by use of deformable or shape models.

Cerebral volumes should generally be normalized as great inter-subject variability exists and the volume of the healthy mature brain is presumed to be correlated with the volume of the cranium cavity [29, 50]. In the study, the measurements were normalized with estimated total intra-cranial volume obtained by a fitted stereotaxic mask. The accuracy of such an approach is highly dependent on the registration method and intra-cranial volume estimations calculated without registration could improve the accuracy and remove registration bias.

The rate of change in cerebral volumes was not significantly higher in mutation carriers compared to non-carriers while atrophy rates based on cortical thickness both averaged within the lobes and focally by the statistical maps showed significant difference between the groups. This indicates that cortical thickness is more sensitive than volume measures. A formal study evaluating the sensitivity of the measures should be carried out to determine the difference between the measures.

The statistical maps used in the study were created by hypothesis testing at each vertex of a reference surface. In hypothesis testing, there is a probability for incorrectly rejecting the null hypothesis; the false positive rate. When performing thousands of tests as in the generation of the statistical maps, there is bound to be incorrect test outcomes, thus leading to false positives. In the study, this problem is addressed by calculating corrected significance thresholds based on controlling the false discovery rate (FDR) [20]. However, the FDR method eliminated all significant focal effects in some of the statistical maps. Controversy exists whether to apply methods for controlling the false positive rate at the risk of not reporting important findings [19, 38]. In the FTD-3 study, large smoothing kernels were applied to the maps so only clusters of vertices where the null hypothesis are rejected remain. The probability that a single test is wrong is at the level of determination; however, the probability that several vertices in the same neighborhood all have wrong outcomes is significantly reduced. Therefore, it is argued that problems with multiple comparisons are insignificant after smoothing the maps. Even though these arguments seem to hold, the arguments should be supported by studies investigating the impact of the different parameters involved in creating cortical statistical maps, e.g. the effect of spatial inter-dependency of the measurements on the statistical model. Such investigations may lead to a theoretical foundation of the statistical maps generated for cortical features.

7.4 Future Directions

The subjects covered in this thesis lead to a range of questions and recognition of problems still unresolved in quantification of cerebral cortical structures by use of surface models. These questions and problems should be addressed in future studies.

Firstly, the accuracy of the proposed parametric deformable model must be further investigated and comparisons with geometric deformable models should be carried out as these models have become popular during recent years. The accuracy of the reconstructed surfaces have been evaluated on the basis of young healthy subjects and phantom MRI scans. Studies of the performance on old and pathological brains should be conducted. Recent initiatives of collecting data from neurodegenerative diseases, such as the Alzheimer's Disease Neuroimaging Initiative[2], provide means for evaluations on old and pathological brains. Validation by comparison to manual delineations, histological measures and animal studies are also possible directions for determining the accuracy and reliability of the cortical reconstruction.

Secondly, for the purpose of high throughput in large scale studies, automation and robustness is essential. For the cortical reconstruction method presented here, the brain extraction step is identified as the weakest link. Future effort should be put into improving this step with the purpose of developing methods robust to the altered MRI signal intensity due to age. Robust brain extraction is continuously being researched by other groups [1, 4, 17, 28] and progress in the field may advantageously be incorporated into the cortical reconstruction pipeline.

Thirdly, the investigation of different cortical mapping algorithms revealed a need for improvements within the field which was mainly caused by the high variations of cortical folding patterns between individuals. Future studies should look into the possibility of categorizing cortices on the basis of folding patterns and the construction of specialized cortical templates.

Fourthly, evaluations of the measures calculated from the cortical surfaces have not been the subject of this thesis and work within this field could improve the reliability of the results obtained. Others have evaluated different measures of cortical thickness [36] and it should be investigated whether the conclusions drawn by this study apply to the surfaces generated by the cortical reconstruction method presented in the present thesis. Apart from cortical thickness, volume estimates are also derived from the surfaces. When using the cortical surfaces to calculate volume measurements of the cerebral tissues two problems arise: 1) absolute volumes must be normalized by an invariant factor correlated to the maximum matured brain size and 2) WM volume estimates are corrupted by enlargements of the ventricles as the WM surface encompasses these cavities. As done in the FTD-3 study, normalization can be performed by estimation of the intra-cranial volume as this measure is presumed to reflect the maximum matured brain volume and to remain constant over time [50]. Often the intra-cranial volume is estimated by a brain mask generated to remove the scalp [22, 48, 54]; however, such masks may not reflect the true intra-cranial volume. Therefore, work specifically directed toward estimating the intra-cranial volume should be carried out. The problem of enlarged ventricles in the WM volume estimations can be addressed by explicitly modeling the ventricles. Several methods for ventricles modeling exist [6] and future improvement of the cortical reconstruction pipeline could incorporate a suitable method for modeling the ventricles. Incorporation of measures of ventricle size and shape may provide additional information of atrophy progression [46].

Fifthly, the sensitivity of the cortical thickness compared to traditional volume measures should be investigated. The FTD-3 study [16] indicated that the cortical thickness measurements are superior to volume estimates when detecting subtle cortical changes. Further work should confirm this observation and evaluate the sensitivity of the measures. This could be done using the realistic brain phantoms generated from cortical surfaces as described in Paper III [14].

[2]For more information see http://www.loni.ucla.edu/ADNI/

Finally, further work on statistical parametric maps of morphological features, such as the cortical thickness, should be carried out. Studies examining the reliability of the evidence produced by statistical maps are important for the general acceptance of results found by cortical surface reconstructions and subsequent mapping. In addition, the statistical method for generating the maps should be evaluated and it should be investigated if inclusion of the spatial inter-dependency of the measurements could improve the statistical model.

7.5 Conclusion

This thesis has demonstrated that the human cerebral cortex can be reconstructed from brain MRI by means of parametric deformable surfaces. The resulting high resolution surfaces provide means for detailed measurements of the cortical morphology. The accuracy of the developed method has been shown to be at subvoxel level and the method is geometrically more accurate than a widely used competing reconstruction method. The topologically correct cortical surfaces are generated automatically and robustly by incorporating a series of preprocessing steps based on existing voxel based methods. Compared to other parametric reconstruction methods, the developed algorithm is fast; complete reconstructions are generated in less than one hour from native scanner images.

The problem of cortical mapping has been addressed and strengths and weaknesses of different methods for solving the mapping problem have been uncovered in a comparative study. The study indicates that more work needs to be done in this field to address the wide morphological variability of human cortices.

Finally, the developed methods have been applied in a study of preclinical subjects with an inherited neurodegenerative disease. It was demonstrated that atrophy is detectable at this preclinical stage of the disease and that cortical thickness based measurements are more sensitive than volume measures.

The work presented in this thesis is part of ongoing efforts toward the goal of diagnosing and differentiating between neurodegenerative diseases by means of cortical atrophy patterns. Future directions of technological improvements rendering this goal probable have been pointed out. If these issues are addressed, the quantification methods are ready to be deployed in large scale studies toward the goal of diagnosing and differentiating between neurodegenerative diseases.

References

[1] J. Acosta-Cabronero, G. B. Williams, J. M. S. Pereira, G. Pengas, and P. J. Nestor. The impact of skull-stripping and radio-frequency bias correction on grey-matter segmentation for voxel-based morphometry. *NeuroImage*, 39(4):1654–1665, 2008.

[2] A. A. Amini, T. E. Weymouth, and R. C. Jain. Using dynamic programming for solving variational problems in vision. *IEEE Transactions on Pattern Analysis and Machine Intelligence*, 12(9):855–867, 1990.

[3] J. B. Arnold, J. . Liow, K. A. Schaper, J. J. Stern, J. G. Sled, D. W. Shattuck, A. J. Worth, M. S. Cohen, R. M. Leahy, J. C. Mazziotta, and D. A. Rottenberg. Qualitative and quantitative evaluation of six algorithms for correcting intensity nonuniformity effects. *NeuroImage*, 13(5):931–943, 2001.

[4] M. Battaglini, S. M. Smith, S. Brogi, and N. De Stefano. Enhanced brain extraction improves the accuracy of brain atrophy estimation. *NeuroImage*, 40(2), 2008.

[5] L. Chen and G. Wagenknecht. Automated topology correction for human brain segmentation. *Lecture Notes in Computer Science*, 4191(LNCS):316–323, 2006.

[6] Y. Y. Chou, N. Leporé, G. I. de Zubicaray, O. T. Carmichael, J. T. Becker, A. W. Toga, and P. M. Thompson. Automated ventricular mapping with multi-atlas fluid image

alignment reveals genetic effects in Alzheimer's disease. *NeuroImage*, 40(2):615–630, 2008.

[7] L. D. Cohen and I. Cohen. Finite-element methods for active contour models and balloons for 2-D and 3-D images. *IEEE Transactions on Pattern Analysis and Machine Intelligence*, 15(11):1131–1147, 1993.

[8] D. L. Collins and A. C. Evans. Animal: Validation and application of nonlinear registration-based segmentation. *International Journal of Pattern Recognition and Artificial Intelligence*, 11(8):1271–1294, 1997.

[9] D. L. Collins, P. Neelin, T. M. Peters, and A. C. Evans. Automatic 3D intersubject registration of MR volumetric data in standardized talairach space. *Journal of Computer Assisted Tomography*, 18(2):192–205, 1994.

[10] A. M. Dale, B. Fischl, and M. I. Sereno. Cortical surface-based analysis: I. Segmentation and surface reconstruction. *NeuroImage*, 9(2):179–194, 1999.

[11] C. Davatzikos. Spatial normalization of 3D brain images using deformable models. *Journal of Computer Assisted Tomography*, 20(4):656–665, 1996.

[12] S. F. Eskildsen, M. Uldahl, and L. R. Østergaard. Extraction of the cerebral cortical boundaries from MRI for measurement of cortical thickness. *Progress in Biomedical Optics and Imaging - Proceedings of SPIE*, 5747(II):1400–1410, 2005.

[13] S. F. Eskildsen and L. R. Østergaard. Active surface approach for extraction of the human cerebral cortex from MRI. *Lecture Notes in Computer Science*, 4191(II):823–830, 2006.

[14] S. F. Eskildsen and L. R. Østergaard. Quantitative comparison of two cortical surface extraction methods using MRI phantoms. *Lecture Notes in Computer Science*, 4791(I):409–416, 2007.

[15] S. F. Eskildsen and L. R. Østergaard. Evaluation of five algorithms for mapping brain cortical surfaces. In *Proceedings of the 21st Brazilian Symposium on Computer Graphics and Image Processing (SIBGRAPI)*. IEEE Computer Society, Oct. 12–15 2008.

[16] S. F. Eskildsen, L. R. Østergaard, A. B. Rodell, L. Østergaard, J. E. Nielsen, A. Isaacs, and P. Johannsen. Cortical volumes and atrophy rates in FTD-3 CHMP2B mutation carriers and related non-carriers. Submitted to NeuroImage, 2008.

[17] C. Fennema-Notestine, I. B. Ozyurt, C. P. Clark, S. Morris, A. Bischoff-Grethe, M. W. Bondi, T. L. Jernigan, B. Fischl, F. Segonne, D. W. Shattuck, R. M. Leahy, D. E. Rex, A. W. Toga, K. H. Zou, and G. G. Brown. Quantitative evaluation of automated skull-stripping methods applied to contemporary and legacy images: Effects of diagnosis, bias correction, and slice location. *Human Brain Mapping*, 27(2):99–113, 2006.

[18] K. J. Friston, J. Ashburner, C. D. Frith, J. . Poline, J. D. Heather, and R. S. J. Frackowiak. Spatial registration and normalization of images. *Human Brain Mapping*, 3(3):165–189, 1995.

[19] L. V. García. Escaping the bonferroni iron claw in ecological studies. *Oikos*, 105(3):657–663, 2004.

[20] C. R. Genovese, N. A. Lazar, and T. Nichols. Thresholding of statistical maps in functional neuroimaging using the false discovery rate. *NeuroImage*, 15(4):870–878, 2002.

[21] S. Gottschalk, M. C. Lin, and D. Manocha. Obbtree: A hierarchical structure for rapid interference detection. *Proceedings of the ACM SIGGRAPH Conference on Computer Graphics*, pages 171–180, 1996.

[22] R. C. Gur, B. I. Turetsky, M. Matsui, M. Yan, W. Bilker, P. Hughett, and R. E. Gur. Sex differences in brain gray and white matter in healthy young adults: Correlations with cognitive performance. *Journal of Neuroscience*, 19(10):4065–4072, 1999.

[23] L. O. Hall, A. M. Bensaid, L. P. Clarke, R. P. Velthuizen, M. S. Silbiger, and J. C. Bezdek. A comparison of neural network and fuzzy clustering techniques in segmenting magnetic resonance images of the brain. *IEEE Transactions on Neural Networks*, 3(5):672–682, 1992.

[24] X. Han, D. L. Pham, D. Tosun, M. E. Rettmann, C. Xu, and J. L. Prince. CRUISE: Cortical reconstruction using implicit surface evolution. *NeuroImage*, 23(3):997–1012, 2004.

[25] X. Han, C. Xu, U. Braga-Neto, and J. L. Prince. Topology correction in brain cortex segmentation using a multiscale, graph-based algorithm. *IEEE Transactions on Medical Imaging*, 21(2):109–121, 2002.

[26] X. Han, C. Xu, and J. L. Prince. A topology preserving level set method for geometric deformable models. *IEEE Transactions on Pattern Analysis and Machine Intelligence*, 25(6):755–768, 2003.

[27] X. Han, C. Xu, D. Tosun, and J. L. Prince. Cortical surface reconstruction using a topology preserving geometric deformable model. *Proceedings of the Workshop on Mathematical Methods in Biomedical Image Analysis*, pages 213–220, 2001.

[28] S. W. Hartley, A. I. Scher, E. S. C. Korf, L. R. White, and L. J. Launer. Analysis and validation of automated skull stripping tools: A validation study based on 296 MR images from the Honolulu Asia aging study. *NeuroImage*, 30(4):1179–1186, 2006.

[29] P. Hartmann, A. Ramseier, F. Gudat, M. J. Mihatsch, W. Polasek, and C. Geisenhoff. Normal weight of the brain in adults, referred to age, sex, height and body weight. *Pathologe*, 15(3):165–170, 1994.

[30] L. He, Z. Peng, B. Everding, X. Wang, C. Y. Han, K. L. Weiss, and W. G. Wee. A comparative study of deformable contour methods on medical image segmentation. *Image and Vision Computing*, 26(2):141–163, 2008.

[31] Z. Hou. A review on MR image intensity inhomogeneity correction. *International Journal of Biomedical Imaging*, 2006, 2006.

[32] D. M. Kim, S. A. Xanthakos, L. A. Tupler, D. P. Barboriak, H. C. Charles, J. R. MacFall, and K. R. R. Krishnan. Mr signal intensity of gray matter/white matter contrast and intracranial fat: Effects of age and sex. *Psychiatry Research - Neuroimaging*, 114(3):149–161, 2002.

[33] J. S. Kim, V. Singh, J. K. Lee, J. Lerch, Y. Ad-Dab'bagh, D. MacDonald, J. M. Lee, S. I. Kim, and A. C. Evans. Automated 3-D extraction and evaluation of the inner and outer cortical surfaces using a Laplacian map and partial volume effect classification. *NeuroImage*, 27(1):210–221, 2005.

[34] U. Kjems, S. C. Strother, J. Anderson, L. Law, and L. K. Hansen. Enhancing the multivariate signal of [15O] water PET studies with a new nonlinear neuroanatomical registration algorithm. *IEEE Transactions on Medical Imaging*, 18(4):306–319, 1999.

[35] N. Kriegeskorte and R. Goebel. An efficient algorithm for topologically correct segmentation of the cortical sheet in anatomical MR volumes. *NeuroImage*, 14(2):329–346, 2001.

[36] J. P. Lerch and A. C. Evans. Cortical thickness analysis examined through power analysis and a population simulation. *NeuroImage*, 24(1):163–173, 2005.

[37] T. Liu, J. Nie, A. Tarokh, L. Guo, and S. T. C. Wong. Reconstruction of central cortical surface from brain MRI images: Method and application. *NeuroImage*, 40(3):991–1002, 2008.

[38] M. D. Moran. Arguments for rejecting the sequential bonferroni in ecological studies. *Oikos*, 100(2):403–405, 2003.

[39] T. Möller. A fast triangle-triangle intersection test. *Journal of Graphics Tools*, 2:25–30, 1997.

[40] D. E. Rex, D. W. Shattuck, R. P. Woods, K. L. Narr, E. Luders, K. Rehm, S. E. Stolzner, D. A. Rottenberg, and A. W. Toga. A meta-algorithm for brain extraction in MRI. *NeuroImage*, 23(2):625–637, 2004.

[41] D. W. Shattuck, S. R. Sandor-Leahy, K. A. Schaper, D. A. Rottenberg, and R. M. Leahy. Magnetic resonance image tissue classification using a partial volume model. *NeuroImage*, 13(5):856–876, 2001.

[42] Y. Shi and W. C. Karl. A real-time algorithm for the approximation of level-set-based curve evolution. *IEEE Transactions on Image Processing*, 17(5):645–656, 2008.

[43] J. G. Sled, A. P. Zijdenbos, and A. C. Evans. A nonparametric method for automatic correction of intensity nonuniformity in mri data. *IEEE Transactions on Medical Imaging*, 17(1):87–97, 1998.

[44] S. M. Smith. Fast robust automated brain extraction. *Human Brain Mapping*, 17(3):143–155, 2002.

[45] B. Suman and P. Kumar. A survey of simulated annealing as a tool for single and multiobjective optimization. *Journal of the Operational Research Society*, 57(10):1143–1160, 2006.

[46] L. J. Thal, K. Kantarci, E. M. Reiman, W. E. Klunk, M. W. Weiner, H. Zetterberg, D. Galasko, D. Praticò, S. Griffin, D. Schenk, and E. Siemers. The role of biomarkers in clinical trials for Alzheimer disease. *Alzheimer Disease and Associated Disorders*, 20(1):6–15, 2006.

[47] B. D. Ward. Intracranial segmentation. Technical report, Medical College of Wisconsin, 1999. http://afni.nimh.nih.gov/pub/dist/doc/manual/3dIntracranial.pdf.

[48] J. L. Whitwell, W. R. Crum, H. C. Watt, and N. C. Fox. Normalization of cerebral volumes by use of intracranial volume: Implications for longitudinal quantitative mr imaging. *American Journal of Neuroradiology*, 22(8):1483–1489, 2001.

[49] D. J. Williams and M. Shah. A fast algorithm for active contours. In *Third International Conference on Computer Vision*, 1990.

[50] H. Wolf, F. Kruggel, A. Hensel, L. O. Wahlund, T. Arendt, and H. J. Gertz. The relationship between head size and intracranial volume in elderly subjects. *Brain Research*, 973(1):74–80, 2003.

[51] R. P. Woods, S. T. Grafton, C. J. Holmes, S. R. Cherry, and J. C. Mazziotta. Automated image registration: I. General methods and intrasubject, intramodality validation. *Journal of Computer Assisted Tomography*, 22(1):139–152, 1998.

[52] C. Xu, D. L. Pham, M. E. Rettmann, D. N. Yu, and J. L. Prince. Reconstruction of the human cerebral cortex from magnetic resonance images. *IEEE Transactions on Medical Imaging*, 18(6):467–480, 1999.

[53] C. Xu and J. L. Prince. Snakes, shapes and gradient vector flow. *IEEE Transactions on Image Processing*, 7(3):359–369, March 1998.

[54] R. Zivadinov, L. Locatelli, B. Stival, A. Bratina, A. Grop, D. Nasuelli, O. Brnabic-Razmilic, and M. Zorzon. Normalized regional brain atrophy measurements in multiple sclerosis. *Neuroradiology*, 45(11):793–798, 2003.